X-ray Microscopy of Hydrocarbon-Clay Interactions

A Thesis Submitted to the College of
Graduate Studies and Research
In Partial Fulfillment of the Requirements
For the Degree of Masters of Science
In the Department of Chemistry
University of Saskatchewan
Saskatoon

By

Danielle Covelli

Permission to Use

In presenting this thesis in partial fulfillment of the requirements for a postgraduate degree from the University of Saskatchewan, I agree that the Libraries of this University may make it freely available for inspection. I further agree that permission for copying of this thesis in any manner, in whole or in part, for scholarly purposes may be granted by Professor S.G. Urquhart who supervised my thesis work or, in his absence, by the Head of the Department of Chemistry or the Dean of the College of Graduate Studies and Research. It is understood that any copying or publication or use of this thesis or parts thereof for financial gain shall not be allowed without my written permission. It is also understood that due recognition shall be given to me and to the University of Saskatchewan in any scholarly use that may be made of any material in my thesis.

Request for permission to copy or to make other use of material in this thesis in whole or in part should be addressed to:

The Head
Department of Chemistry
University of Saskatchewan
Saskatoon, Saskatchewan
Canada S7N 5C9

Abstract

One of the critical challenges in the Canadian oil sand industry is improving processes used to separate bitumen from oil sands and to remove clay particulates from produced oil. The fine clay particles are believed to play a significant role in the oil sands industry, from stabilizing process emulsions to fouling problems in water treatment. Addressing the problems caused by these fine clay particulates is limited by the ability to characterize the hydrocarbon-clay interactions.

Scanning Transmission X-ray Microscopy (STXM) is used to study hydrocarbon-clay interactions in controlled model systems, where all components are known, and in process samples extracted from oil sands. To use STXM to study our desired systems, many experimental developments were required. Well developed sample preparation was needed to provide samples free from contaminants and experiments free of artifacts. Clean clays, free of extraneous carbon were required for model studies. A device to reduce photodeposition in the STXM chamber was also required to examine interactions of hydrocarbons on clay surfaces.

Using these developments, Near Edge X-ray Absorption Fine Structure (NEXAFS) spectra of model clays and model hydrocarbon mixtures were recorded using the STXM microscope on beamline 5.3.2 at the Advanced Light Source, in Berkeley CA. Using NEXAFS spectroscopy in conjunction with the STXM microscope, allowed us to explore preferential interactions between specific hydrocarbon and fine clay particles (smaller than 1 μm) in our model studies. We were also able to assess the chemistry of the hydrocarbons before association with the clay particles.

Process samples, consisting of a set of four bitumen froths extracted from the oil sands were investigated. The carbon chemistry of the froths was assessed and quantitatively analyzed. The findings were correlated with previous confocal microscopy results from our collaborators at CANMET Energy Technology Centre in Devon, Alberta.

Acknowledgements

First and foremost, I would like to graciously thank my research supervisor, Dr. Stephen Urquhart, for his invaluable support and guidance throughout the two years of this Masters work. Also, for providing me with the opportunity to be involved in this fascinating research project. The experience and knowledge gained under his supervision are both valuable and essential for my future growth in research, and as a scientist. I greatly appreciate all of the time and hard work he invested in me.

I would also like to thank my advisory committee member, Dr. Reid, for his valuable comments and advice during committee meetings.

I am very grateful to various members of Professor Urquhart's lab, including Edwige Otero, Dr. Juxia Fu, Dr. Brian Haines, Stephen Christensen, Rèmy Coulomb and Éric Christensen for their support. I would like to especially thank Edwige Otero for her valuable advice, patience and generosity throughout the entirety of my project.

Also, I am very appreciative of our collaborators at NRCan in Devon, AB; Randy Mikula, Oladipo Omotoso and Vincente Munoz who were instrumental in providing samples and advice throughout the project.

I wish to thank both Dr. David Kilcoyne and Dr. Tolek Tylisczack for their excellent advice and support while running experiments at the Advanced Light Source (ALS).

Finally, I would like to thank the Department of Chemistry, University of Saskatchewan, NSERC, and NEXEN for financial support of the project. Also I would like to acknowledge the ALS where all experiments were performed. The Advanced Light Source is supported by the Director, Office of Science, Office of Basic Energy Science, of the U.S. Department of Energy under contract No. DE-AC02-05CH11231.

Table of Contents

List of Tables

List of Figures

List of Abbreviations

AFM	Atomic Force Microscopy
ALS	Advanced Light Source
AEY	Auger Electron Yield
CBD	Citrate-bicarbonate-dithionate
EELS	Electron Energy Loss Spectroscopy
EPU	Elliptical Polarized Undulator
EXAFS	Extended X-ray Absorption Fine Structure
HPAM	Hydrolyzed Polyacrylamide
IR	Infrared
MOS	Model Oil Sands
NEXAFS	Near Edge X-ray Absorption Fine Structure
NMR	Nuclear Magnetic Resonance
NRCan	Natural Resources Canada
NSLS	National Synchrotron Light Source
OD	Optical Density
OSA	Order Sorting Aperture
PEY	Partial Electron Yield
PMT	Photo Multiplier Tube
SGM	Spherical Grating Monochromator
STEM	Scanning Transmission Electron Microscopy
STXM	Scanning Transmission X-ray Microscopy

TDM	Transition Dipole Moment
TEM	Transmission Electron Microscopy
TEY	Total Electron Yield
VLM	Visual Light Microscope
XAS	X-Ray Absorption Spectrosocpy
XRD	X-Ray Powder Diffraction

CHAPTER 1
INTRODUCTION

The oil sands in northern Alberta contain large amounts of bitumen, which can be extracted and converted into synthetic crude oil through flotation and purification processes. Oil sands are a complex mixture of clays, sand, bitumen, water and mineral phases. A hot water flotation technique is commonly used to extract bitumen from the oil sands. However, it has been recognized that this processing is complicated by fine clay particles and divalent ions present in the oil sands, as these are believed to interfere with the flotation process and cause emulsion stabilizations.[1-3] These complications lead to decreased production and require more energy for separation. Therefore, it is of fundamental importance to understand the nature of the interactions between the hydrocarbons and the fine particle content, especially the clay particulates which are believed to be one of the largest contributors to these processing problems.[3] The ability to address processing issues is amplified by the complexity of characterizing the relevant hydrocarbon-clay interactions.

The overall goal for this research program is an improved understanding of the physical interactions between the surfaces of clay particles and organic phases present in the oil sands. The specific goal of this Masters project is to develop methods to study and characterize hydrocarbon-clay associations in both model systems and process samples. We have applied X-ray spectromicroscopy to study the nature of these interactions.

X-ray spectromicroscopy is the combination of chemically sensitive Near Edge X-ray Absorption Fine Structure (NEXAFS) spectroscopy with high spatial resolution X-ray microscopy.

X-ray spectromicroscopy is a rapidly evolving field which has been extensively used for the chemical characterization of organic species, such as polymers,[4-9] organic molecules,[10,11] biological[12,13] and environmental[14-16] samples. This technique is well suited to study hydrocarbon-clay associations in a variety of model clays, model organic-clay and process oil sand samples. The detailed research objectives for the portion of the project studied in this Masters thesis are outlined in §1.6.

An introduction to the oil sands and the processing problems associated with the interaction of hydrocarbons with clay particulates is briefly described in §1.1. An introduction to the theory of NEXAFS spectroscopy and its chemical and orientational sensitivity are described in detail in §1.2. The technique and capabilities of X-ray microscopy are briefly illustrated in §1.3. The model clay systems that will be studied in the project are discussed in §1.4. Section 1.5 introduces the types of samples that will be studied in the thesis. An outline of the thesis and research objectives are provided in §1.6.

1.1 Clay Particles in the Oil Sands

Oil sands are located throughout many parts of the world; however, the largest currently known field is in northern Alberta, Canada.[17] The reserves in northern Alberta are estimated to contain 1.7 trillion barrels of bitumen.[3] Oil extracted from these oil sands represents almost 50% of Canada's total crude oil output.[18]

Bitumen is commonly extracted from the oil sands using a water-based flotation technique. At the start of the process, the oil sands are mixed with water to release the bitumen from the sand and fine clay particles. This is followed by aeration, where air is added into the mixture, allowing the liberated bitumen to attach to the air bubbles. The last step involves flotation of the aerated bitumen.[19] The floatation is key for separation, as it separates the bitumen from water and solid particles.[19] Under the best circumstances, 95% of the bitumen can be recovered, however; problems can lower the recovery to less than 70%.[3] In some cases, the reduced recovery has been speculated to be partially related to the amount and types of fine particles present in the oil sands, and their interactions with bitumen and other organic phases.[1-3,20]

In the oil sands industry, "fines" are defined as mineral particulates smaller than 44 μm.[18] The fine particles associated with the oil sands vary throughout the deposit; however, fine clay particles are believed to have the largest effect on the efficiency of bitumen recovery. There has been extensive research invested in clay mineralogy of the oil sands, which indicated the fine clay particles are principally illite and kaolinite, with very small amounts of chlorite, montmorillonite, and mixed-layer clays.[21]

There is also a large variety of organic components present in the oil sands. For instance, bitumen is a complex mixture of many different organic species. Some of which include non-polar aliphatic and naphthenic hydrocarbons (such as naphtha and naphthenic acids) while others are highly polar aromatic molecules combined with heteroatoms (O, N and S), such as asphaltenes and resins.[22,23] The bitumen can also have transition metal ions complexed to porphyrins and other polar molecules.[22] Using fractional chromatography and separation methods, it has been shown that bitumen in oil

sands is primarily composed of 67 w% aromatic compounds, 29 w% resins and 4 w% saturates.[24]

Past research has also focused on the study of features affecting the coagulation and coalescence of clays, as well as factors affecting the bitumen recovery. Some studies have also taken interest in examining clay-clay interactions, and clay-bitumen interactions within the oil sands.[1,3,18,20,25] These are described in the following section.

Long et al. (2006) studied different methods of coagulation of clays to improve oil sands processing. In this study, they examined illite-illite interactions under several different conditions and found that addition of calcium and magnesium ions to solution, as well as relatively low pH (2.9), tended to favor the coalescence of illite particles.[18] Adding a flocculate, partially hydrolyzed polyacrylamide, also increased the agglomeration of clays. They believed clay flocculation/coagulation would be desirable in both bitumen extracting and tailings treatment because it could lead to fast settling of solids in the tailings.[18] Despite finding successful ways to make illite particles coalesce in solution, some of the methods are not feasible for oil sands processing.

A study by *Fong et al.* (2004), used a series of model oil sands (MOS) to perform screening studies of bitumen recovery. The MOS were comprised of 10-wt% bitumen, 5-wt% water and 85-wt% solids (75-wt% coarse silica and 25-wt% silica fines).[25] A warm water extraction process was performed to assess the effective bitumen recovery. To evaluate the different variables, they determined bitumen content gravimetrically, and used particle size distribution tests and a 3-factor Box-Behnken analysis for quantification.[26] Processability curves were created for the different variables to find the maximum bitumen recovery under the varying conditions. The variable MOS were

compared with a standard MOS to find optimal conditions for bitumen recovery. They concluded that coarse solids (106-212 μm) and sodium ions in process water did not affect bitumen recovery; whereas, magnesium and calcium ions in process water and the presence of montmorillonite (0.05 – 1 wt%) caused permanent loss of bitumen recovery. Their study produced valuable insight into factors effecting bitumen recovery in ideal model systems: however, they cannot apply their findings to associations causing recovery loss in "real" systems where unusual situations might occur.

Czarnecka et al. (1980) combined X-ray powder diffraction (XRD) and infrared spectroscopy (IR) to study the adsorption of bitumen on clays.[20] All bitumen components (asphaltenes, resins, etc) exhibited IR bands at identical positions; however, the relative intensities of C-H and C=C stretching bands for aromatic rings were different. The highest ratio of aromatic components was found in asphaltenes, suggesting asphaltenes have either more aromatic groups or a larger molecular size.[25] From IR data, organics appeared to be absorbing to clay surfaces and not within clay interlayers. IR also showed bitumen extracted from the oil sands was adsorbed by different clays, and some of the adsorbed organic matter could be removed using organic solvents (toluene and a 70:30 mixture of chloroform-acetone).[20] From XRD data, the ability of organic molecules to enter the interlayer space was assessed by testing a series of samples under varying conditions. The XRD results were independent of the different conditions applied, demonstrating organic substances from the oil sands were adsorbing on clay surfaces rather than within clay interlayers, thereby verifying what was slightly evident in their IR data.[20]

Liu et al. (2004), examined the interaction of bitumen with montmorillonite and kaolinite using Atomic Force Microscopy (AFM). Without the addition of calcium ions, they found the montmorillonite-bitumen interactive force profiles were highly repulsive setting a barrier for montmorillonite to approach bitumen. The addition of Ca^{2+} caused a significant decrease in the repulsion force and enhanced adhesion forces.[1] The decrease in long-range repulsive forces allows the clay to approach bitumen more easily. The kaolinite-bitumen force profiles were also found to be highly repulsive. Adding Ca^{2+} depressed the repulsion forces; however the adhesion forces remained weak, signifying that kaolinite would only weakly attach to bitumen. These differences were attributed to Ca^{2+} adsorbing well to the surface of bitumen and montorillonite but not to the surface of kaolinite. This indicated that bitumen-montmonorillonite interactions were stronger than bitumen-kaolinite interactions, especially when Ca^{2+} ions were present in solution, which was attributed to increased adhesion forces.[1] Zeta potential distribution measurements supported these results.

To advance their previous findings involving the bitumen interactions between two model clays, Liu and coworkers (2004) examined interactions between bitumen and fine particles extracted directly from the oil sands.[2] They were interested in characterizing the bitumen-fine particle interactions in good and poor processing ores. Interactive force profiles from AFM studies showed repulsive force profiles with weak adhesive forces for good processing ores, and attractive force profiles with strong adhesive forces for poor processing ores. This indicates that interactions between bitumen and fine particles in poor processing ores are more favorable than in good processing ores. The measurements were corroborated with the use of zeta potential distribution measurements.

Bantignies et al. (1998) studied the absorption of asphaltenes on clay surfaces using IR, NEXAFS spectroscopy and Extended X-Ray Absorption Fine Structure (EXAFS). The IR data showed only the OH surface of kaolinite was sensitive to contact with asphaltenes and no changes were seen in the illite spectrum after contact with asphaltenes.[27] The Al K-edge NEXAFS and EXAFS showed the surface OH groups were linked to the Al in the kaolinite, confirming the IR results, and the Si environment was not sensitive to contact with the asphaltenes. Both the Al and Si environments in the illite remained the same before and after contact with asphaltenes, indicating no major interaction.

Identifying and characterizing the hydrocarbon-clay interactions is important for understanding the separation and processing problems encountered in the oil sands industry. Therefore, the underlying goal of this project is to characterize the association of organic species with clay surfaces. We propose to use NEXAFS spectroscopy to study associations of various hydrocarbon-clay systems. NEXAFS spectroscopy is a direct probe of the local environment surrounding the absorbing atom, and will allow us to identify the chemical species adsorbed to clay particles. Our C 1s NEXAFS spectra will be obtained using the Scanning Transmission X-ray Microscope (STXM) to achieve micro-imaging and high chemical sensitivity simultaneously. The technique and instrumentation will be discussed thoroughly in chapters 1 and 2 of this thesis.

1.2 Near Edge X-ray Absorption Fine Structure Spectroscopy

This section will provide a brief introduction to Near Edge X-ray Absorption Fine Structure (NEXAFS) spectroscopy. A more detailed introduction to these experiments will be provided in § 2.1. NEXAFS, or X-ray Absorption Spectroscopy (XAS) is an

elementally specific core level spectroscopy. X-rays can have sufficient energy to excite or ionize core electrons within an atom or molecule. An electronic transition occurs when the X-ray energy matches the energy required to make a core excited state. In NEXAFS spectroscopy, the K edge refers to the excitation of core electrons from the 1s shell; whereas, L edge spectroscopy refers to excitation from the 2s (L_1), $2p_{1/2}$ (L_2) and $2p_{3/2}$ electron shells. The edge jump corresponds to an absorption cross-section increase at the core electron ionization potential. An example of these different edges is illustrated below in Figure 1-1 .

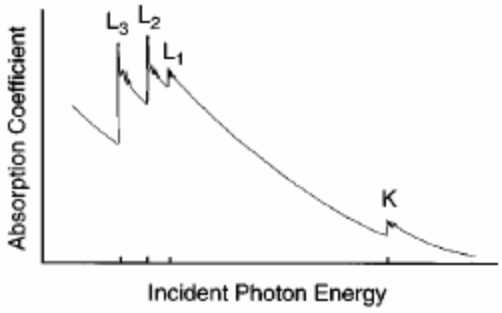

Figure 1-1. X-ray absorption coefficient as a function of photon energy demonstrating different X-ray absorption edges (L_3, L_2,L_1).[28]

1.2.1 X-Ray Absorption Spectrum

The X-Ray Absorption Spectrum (XAS) is divided into two regions; the NEXAFS region and the EXAFS region. This division is shown in Figure 1-2. The NEXAFS region ranges from slightly below the edge jump to approximately 50 eV above the edge; whereas, the EXAFS region ranges from 50 eV above the edge to well beyond the ionization edge.[29] NEXAFS features are commonly attributed as electronic transitions to specific unoccupied molecular orbitals, for example C 1s (C=O) $\rightarrow$ $\pi^*_{(C=O)}$ transition

characteristic of a carbonyl species. This is in contrast to EXAFS features, which are due to electron scattering from neighboring atoms close to the core excited atom.

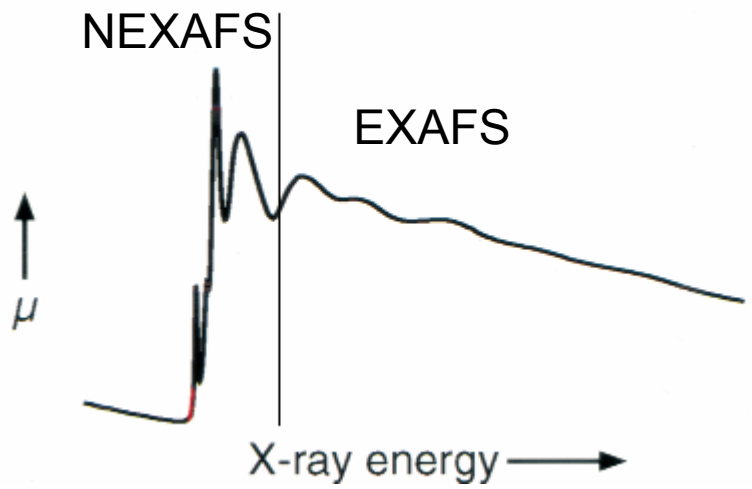

Figure 1-2. Major regions in a typical XAS spectrum.[30]

In addition to elemental information, NEXAFS spectroscopy can provide chemical bonding and functional group information. For example carbon-carbon double bonds, and aromatic groups appear as pre-edge peaks at ~285 eV; whereas carbonyl functionalities (C=O) exhibit peaks at ~ 288 eV, but vary slightly depending on their chemistry (ketone, carbonate, etc). NEXAFS can also provide information on the orientation of functional groups on surfaces or within molecules, as well as magnetic structure.[31] EXAFS spectra can provide information on the local atomic structure around the core excited atom, such as bond lengths, identity of neighboring atoms and coordination number.[28]

1.2.2 X-Ray Absorption Cross Section

The edge jump in NEXAFS spectra appears as an abrupt step-function type absorption.[28] The X-ray absorption cross section (σ_x) of an atom or molecule is

commonly defined as the number of photons excited per unit time divided by the flux (number of incident photons per unit time) per unit area.[31] This atomic cross section can be calculated using Fermi's "Golden Rule", in conjunction with applying the dipole approximation, to provide the final result for the X-ray absorption cross section as follows;

$$\sigma_x = \frac{4\pi^2\hbar^2}{m^2}\frac{e^2}{\hbar c}\frac{1}{\hbar\omega}\left|\langle f|e_F \bullet p|i\rangle\right|^2 Q_f(E) \qquad (1)$$

where σ_x is the X-ray absorption cross section in cm^2, ħ is Planck's constant divided by 2π, *e* is an electron charge, *m* is the mass of the electron, ħω is the photon energy, *c* is the speed of light, e_E is the electric field vector, *p* is the dipole operator, *f* is the wavefunction in the final state, *i* is the wavefunction in the initial state and Q_f (E) is the energy density of final states.[31]

The optical oscillator strength (*f*), is a dimensionless quantity related to the X-ray absorption cross section according to the equation,

$$\sigma_x = C\frac{df}{dE} \qquad (2)$$

where $C = 2\pi^2e^2\hbar/mc$.[31] Thus, the oscillator strength is a measure of the intensity of a resonance and the intensities to bound state transitions are normally represented by

$$f = \frac{2}{m\hbar\omega}\left|\langle f|e \bullet p|i\rangle\right|^2 \qquad (3)$$

which is commonly reported as "*f* number".[31] The discrete and continuum oscillator strengths must fulfill specific sum rules, the most common being the Thomas-Reiche-Kuhn sum rule.[31] This rule states that the sum of the oscillator strengths of transitions to all states is unity for each electron in a particular atom or molecule.[31] Therefore, the total oscillator strength for the electronic excitation of an atom or molecule is equal to the

number of electrons in the atom or molecule, which can be represented mathematically by

$$\sum_n f_n + \int_{IP}^{\infty} \frac{df(E)}{dE} dE = N \qquad (4)$$

where N is the number of electrons.[31] Thus, the area under the curve of a plot of df(E)/dE as a function of energy must be proportional to the number of electrons in the system.[31] For instance, in normalized C 1s spectra, the integrated C 1s absorption area must be the same for multiple spectra of a sample. Thus, if the intensity of one peak in the spectrum increases, the intensity of another peak must decrease such that the area under the normalized and background subtracted carbon NEXAFS spectra remains constant. This can be utilized for quantizing NEXAFS data but is only valid for normalized spectra, and is used for part of our analysis in chapter 5.

1.2.3 Chemical Sensitivity of NEXAFS Spectroscopy

NEXAFS is a chemically sensitive spectroscopy. Every element has a characteristic core binding energy, therefore NEXAFS spectra are element specific. Features in the spectra can be attributed to various transitions from the ground state to core excited states.

Although NEXAFS photo-excitation is a multi-electron process, it is useful to describe the process for closed-shell molecules using an orbital approximation such that the excitation process is considered to be a one-electron transition.[8] For instance, in aromatic species, the transition at 285 eV is attributed to a transition from the C 1s electron to a π^* orbital of a phenyl ring. Such details can provide important information regarding the chemical bonding and electronic structure in molecules, specifically the

presence or absence of various functional groups. This exquisite functional group sensitivity can be seen in Figure 1-3. This figure shows the C 1s NEXAFS spectrum of poly(styrene-r-acrylonitrile). In the pre-edge region, the spectrum contains two intense peaks, labeled A and B. Peak A, at approximately 285 eV can be attributed to a C 1s → π* electronic transition of the phenyl functional group; whereas, peak B, at 287 eV arises due to a C 1s → π* electronic transition of the acrylonitrile functional group.[8] This figure nicely demonstrates the functional group sensitivity of NEXAFS; however, an even more powerful component of NEXAFS spectroscopy lies in its ability to decipher between chemical shifts in similar functional groups. This more advanced chemical sensitivity of NEXAFS spectroscopy has been utilized in a multitude of studies over the past few years and will be reviewed below.

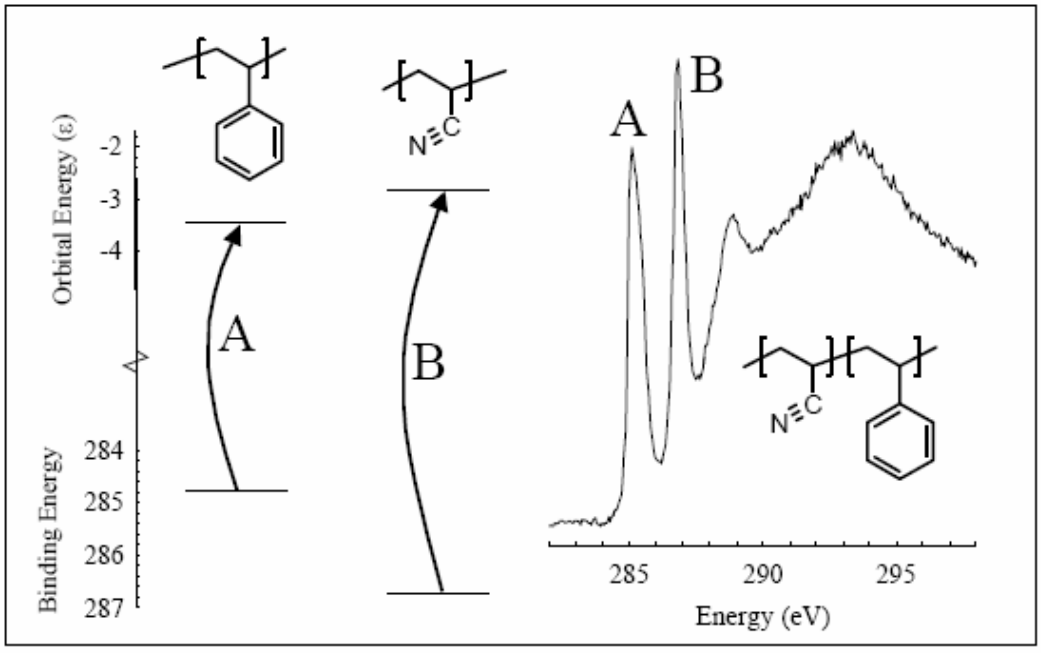

Figure 1-3. Schematic of electronic transitions in the C 1s NEXAFS spectrum of poly(styrene-r-acrylonitrile).[8]

Urquhart et al. (1999) studied the chemical differences between methylene di-p-phenylene isocyanate and toluene diisocyanate polymers, to distinguish between the two polymers but more importantly, to resolve differences in urea and carbonate linkages.[5] On the left side of Figure 1-4**,** four polymers examined and compared in this study are shown, and on the right, the C 1s NEXAFS spectra obtained from the polymers are displayed.

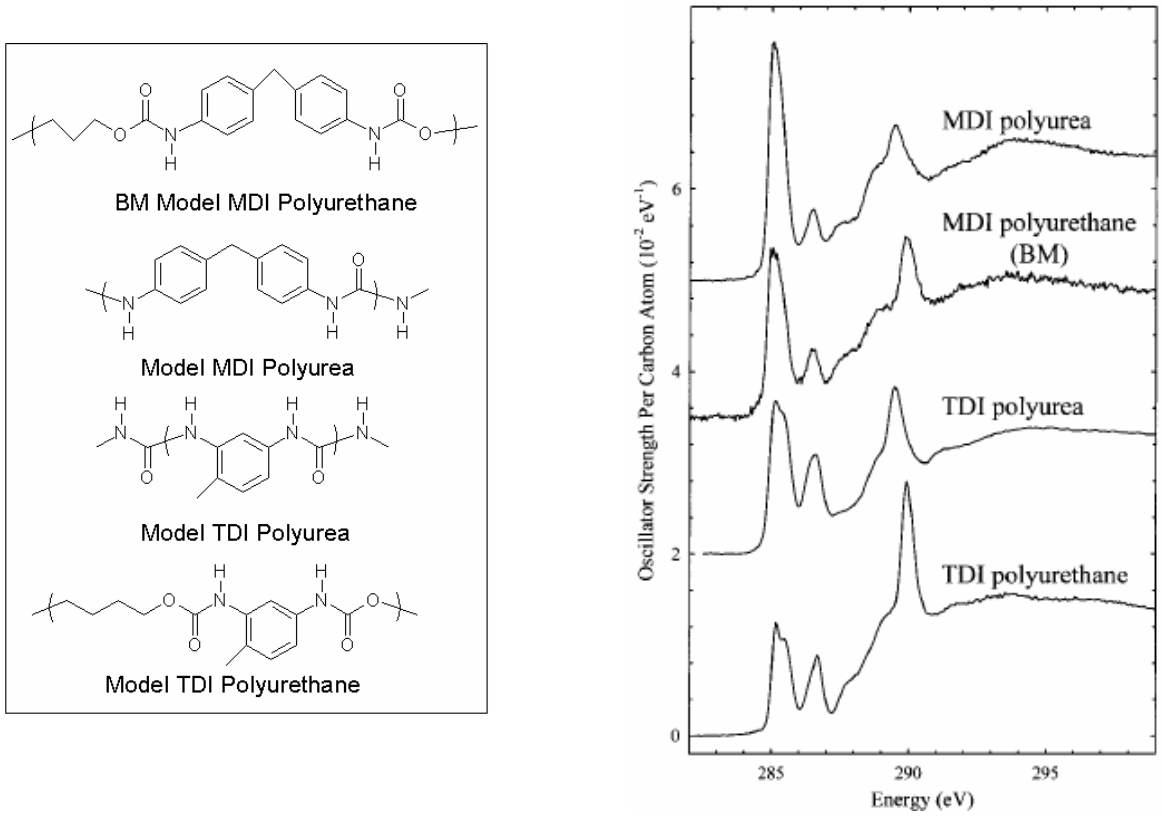

Figure 1-4. (Left) Structures of two polyurea and two polyurethane polymers examined by C 1s NEXAFS, (Right) C 1s NEXAFS spectra of the 4 polymers.[5]

The key to understanding the differences between the two types of polymers was found in the pattern of the C 1s (C-H) → $1\pi^*_{C=C}$ transition (located at approximately 285.2 eV) and C 1s (C-R) → $1\pi^*_{C=C}$ transitions (located at approximately 286.5 eV).[5] The energy splitting between these two transitions was very similar for both types of

polymers; however, the intensity ratio of the C-R/C-H transitions was vastly different, creating a distinguishing feature. They were also able to differentiate between the two types of linkages, urea and carbonate, from the energy of the C 1s (C-R)→ $1\pi^*_{C=C}$ transition. The transition was found to be at a slightly lower energy with a slightly different shape for the polyurea model than for the polyurethane model. It was also found that the C-H and C-R intensities were quite different, in particular the C-H peak was approximately 30% more for the polyurea model than the polyurethane polymer.

To further exhibit the chemical sensitivity of NEXAFS, a 2002 paper by Urquhart and Ade was able to exploit the functional group sensitivity of NEXAFS further by creating a series of correlation diagrams for carbonyl functional groups.[10] This study focused on the carbonyl chemistry occurring from the carbon and oxygen core (C 1s and O 1s) → $\pi^*_{(C=O)}$ transitions in a series of polymers containing carbonyl groups in a variety of different bonding arrangements. By focusing on the energy of the carbonyl transition, they created C 1s and O 1s correlation diagrams for the trends in energy position that various carbonyl functional groups would possess. These correlation diagrams are shown in Figure 1-5 below. Careful calibration and high quality *ab initio* calculations were used to insure the positions reported in the correlation diagrams were accurate, so they could be used in future work to aid in chemical identification of specific carbonyl functionalities.

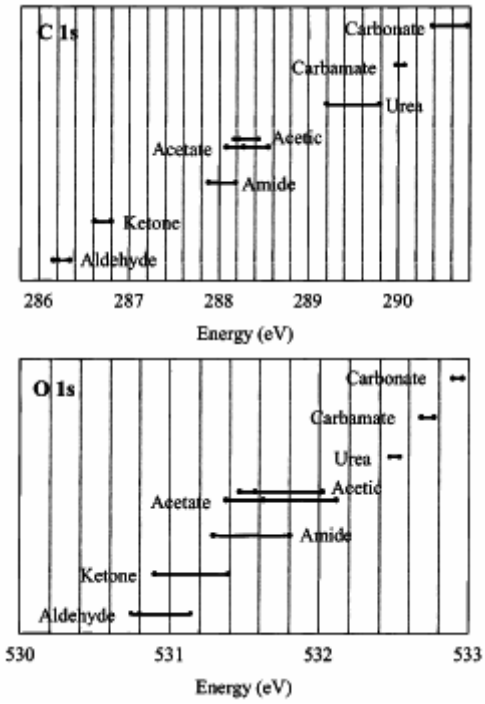

Figure 1-5. Correlation diagram indicating the expected energies for various C 1s and O 1s electronic transitions based on the type of carbonyl moeity present in the molecule.[10]

1.2.4 Orientational Sensitivity of NEXAFS Spectroscopy

NEXAFS spectroscopy is also sensitive to molecular orientation. Linear dichroism is defined as the anisotropic absorption of linear polarized electromagnetic radiation.[32] The intensity of NEXAFS features are dependent on the angle between the X-ray electric field vector e_E and the transition moment vector.[8] The transition intensity varies as

$$I \propto \left| e_E \bullet r \right|^2 \propto \cos^2 \theta \qquad (5)$$

where θ is the angle between the electric-dipole vector r and the electric-field vector e_E.[8]

Synchrotron radiation has well-defined polarization properties. Synchrotron light is 85-90% linear polarized in the horizontal plane on bend magnet beamlines, and to 100% on linear undulator beamlines.[31,33]

A recent example of NEXAFS spectroscopy used to examine molecular orientation of molecules involved investigation of linear dichroism in C 1s → $\sigma^*_{C\text{-}C}$ transitions or a

linear alkane, n-hexacontane.[32] Figure 1-6 shows the C 1s NEXAFS spectra of the hexacontane at 0°, and 90°, the angles at which the intensity of the C 1s $\rightarrow \sigma^*_{(C-H)}$ band reaches a minimum and maximum respectively.[32] From the angle dependence of the C 1s $\rightarrow \sigma^*_{(C-C)}$, they were able to determine that the transition dipole moment (TDM) for the C 1s $\rightarrow \sigma^*_{C-C}$ transition, apparent at 293.5 eV, was orientated along the macromolecular backbone of the linear alkane, as opposed to along individual C-C bonds.

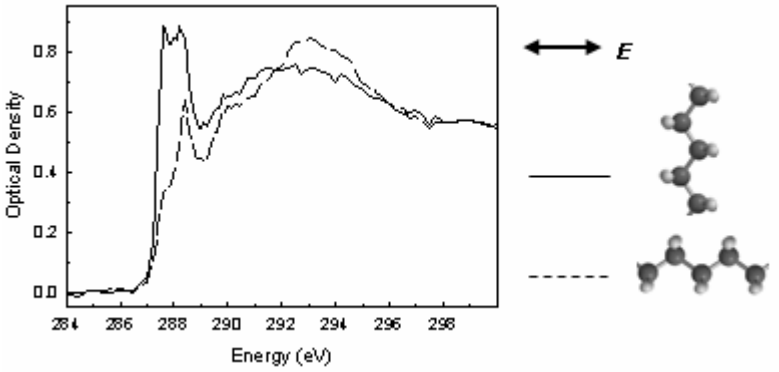

Figure 1-6. C 1s NEXAFS spectra of hexacontane ($C_{60}H_{122}$), at two extreme angles; 0° where the electric field vector was aligned along the macromolecular backbone, and 90°, where the electric field vector was aligned perpendicular to the macromolecular backbone.[32]

1.3 X-ray Microscopy

This section provides a brief introduction to X-ray microscopy and how it can be utilized in the study of complex chemical systems. Section 2.2 will discuss the experimental details on how X-ray microscopy experiments are performed and provide specific details on the X-ray microscope used for these experiments.

X-ray microscopy has undergone rapid development and advances as the availability, quality and brightness of third generation synchrotron facilities has improved. For all the experiments performed in our work, we used scanning transmission X-ray microscopy.

These microscopes use diffractive focusing optics to form an X-ray focus through which the sample can be raster scanned.[34] A schematic diagram of a typical scanning X-ray microscope is shown below in Figure 1-7. The STXM microscope consists of an X-ray source (in this example from an undulator), a monochromator to select the desired photon energy, zone plate optics to focus the beam onto the sample, a controlled stage to allow for sample scanning (peizo and stepper stages), and a detector to measure the X-ray transmission. These components will be discussed in greater detail in chapter 2.

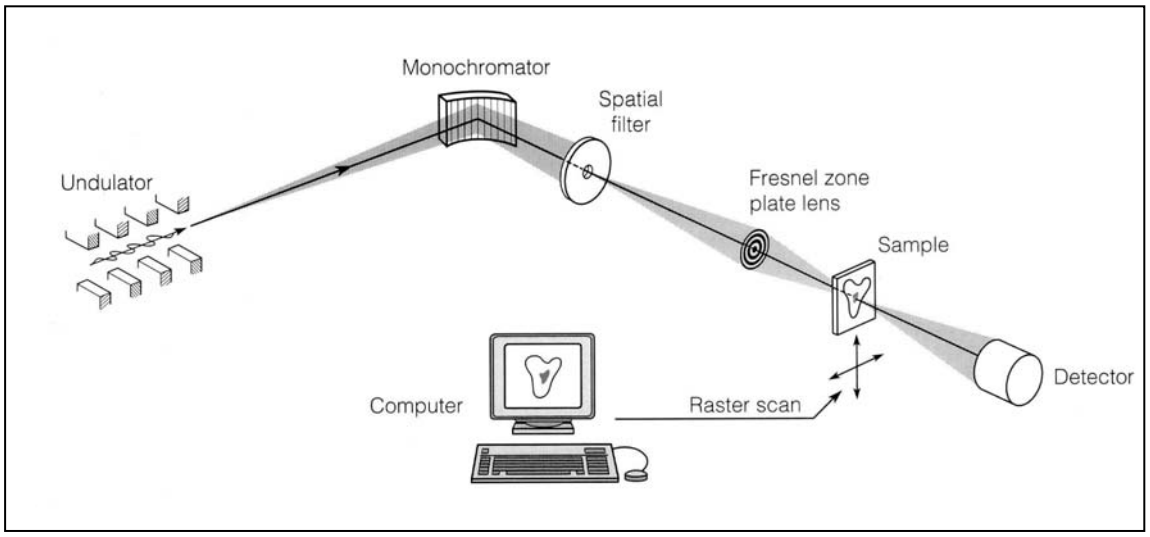

Figure 1-7. Schematic diagram of an scanning transmission X-ray microscope.[4]

The main advantage of using a soft X-ray scanning transmission microscope is that high resolution images can be obtained in combination with high resolution X-ray absorption spectroscopy. This combination of high spatial resolution images from X-ray microscopy and high resolution NEXAFS spectra has led to what is commonly called X-ray spectromicroscopy. This high sensitivity and chemical contrast capability of NEXAFS spectromicroscopy is demonstrated by the example of *Yoon et al.*[35] STXM microscopy was used to investigate a series of hydrated synthetic aluminum containing

mineral colloids. An evaluation of the capability of STXM microscopy to distinguish between similar aluminum samples when mixed in a solution was desired. The first step in the study was obtaining Al 1s NEXAFS spectra of the model compounds alone, shown below in Figure 1-8.

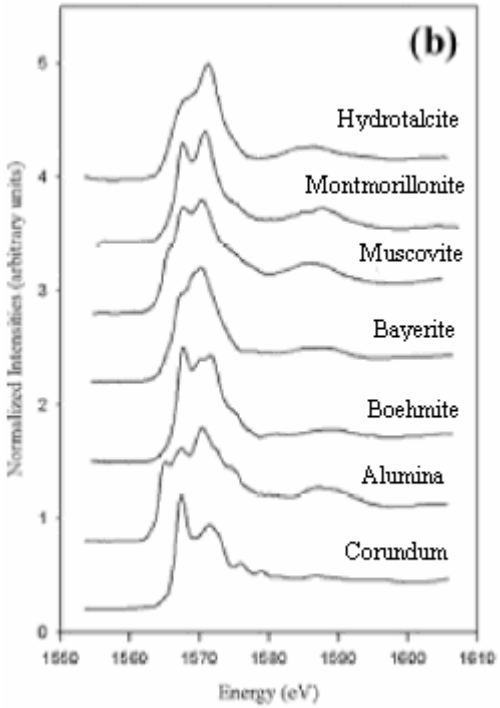

Figure 1-8. Aluminum K-edge NEXAFS spectra of seven reference minerals.[35]

Once individual spectra were obtained, four aluminum containing minerals were mixed in aqueous solution and STXM micrographs were obtained from the hydrated sample. Using the chemical contrast sensitivity of NEXAFS, maps of the different minerals in the mixed, hydrated samples were made by examining images acquired at different energies. Figure 1-9 shows various X-ray microscope images along with the Al-K edge NEXAFS spectra obtained from different regions in the sample. To identify these regions, slightly different photon energies were used to take X-ray microscope images of the sample, as shown in the bottom section of Figure 1-9. Based on the energy at which

different absorption features occur, the authors were able to identify different chemical regions in their mixture. From comparison of previous NEXAFS spectra of each mineral by itself, they could locate each individual mineral in the mixture. This example demonstrates the strengths and unique capabilities of NEXAFS spectromicroscopy.

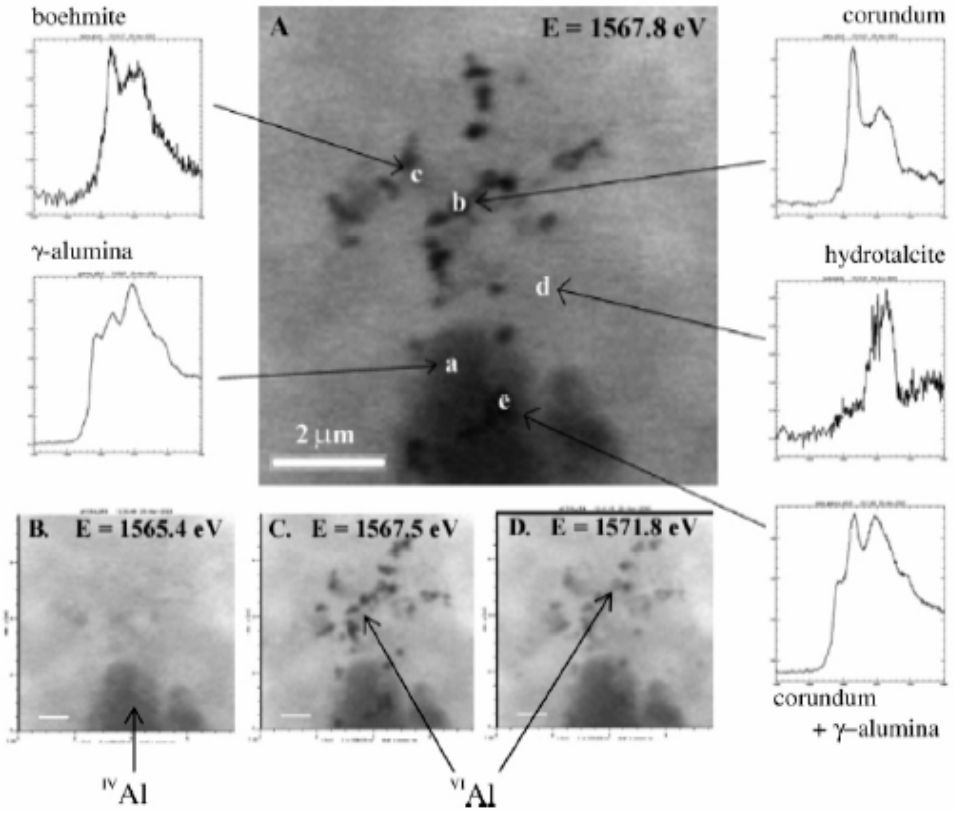

Figure 1-9. STXM micrographs and Al K-edge NEXAFS spectra of various aluminum containing minerals in a mixed aqueous sample.[35]

When examining other common techniques, we can see advantages for the use of NEXAFS spectromicroscopy which provides a balance between spatial resolution and chemical sensitivity.

Infrared Spectroscopy (IR) and Nuclear Magnetic Resonance (NMR) spectroscopy have excellent chemical sensitivity. However, these techniques lack high spatial resolution.[36] Synchrotron FTIR imaging is used to obtain chemical spectra in

combination with high resolution imaging.[37,38] Although synchrotron IR allows for energy resolution better than the STXM ($4cm^{-1}$ ~ 0.5 meV), the spatial resolution is usually diffraction limited to 3-10 μm, significantly poorer than the STXM.[37-39] Similarly, Raman microscopy can be used for obtaining chemical information and imaging with excellent spatial and energy resolution. Although the energy resolution and chemical sensitivity is better than the STXM, the spatial resolution is usually greater than 250 nm, which is significantly poorer than the STXM.[40]

Conversely, microscopy techniques such as Transmission Electron Microscopy (TEM) and Scanning Transmission Electron Microscopy (STEM) have very high spatial resolution (better than the STXM)[41], but they lack the same degree of chemical sensitivity. TEM in conjunction with Electron Energy Loss Spectroscopy (EELS) increases the chemical sensitivity.[42,43] Although some EELS instruments can achieve an energy resolution of 0.1 eV, under most circumstances the energy resolution in NEXAFS spectromicroscopy is much better than that available from EELS, and therefore provides better chemical sensitivity.[41,43] Also, a major drawback of electron beam microscopy is the electron beam causes severe radiation damage to organic samples (breaking bonds and mass loss) and is therefore not suitable for all samples.[36]

Since experiments can be performed under coarse vacuum or in a helium atmosphere, STXM microscopy allows for experiments to be performed using aqueous samples.[15,44-47] For instance, environmental samples can be examined while remaining in their natural hydrated state, as shown earlier in Figure 1-9. in the paper by *Yoon et al*. (2004).[35] This is useful because it allows samples to remain naturally hydrated, in their environmental form, avoiding the creation of artifacts associated with sample drying.

All measurements acquired for the data presented in this project were obtained using STXM 5.3.2 at the ALS in Berkeley California. The experimental details will be thoroughly described in chapter 2.

1.4 Model Hydrocarbon-Clay Systems

The overall goal of this project is to characterize the interaction of hydrocarbons with clay surfaces. To conduct such a study, it is important to start by examining well defined systems, rather than using poorly understood samples extracted directly from the oil sands. Hydrocarbon-clay systems contained in the oil sands are extremely complex, as they consist of a number of different hydrocarbons, such as bitumen, naphthenic acids, asphaltenes, and others. The fine clay particles ("fines") believed to be heavily responsible for oil sands processing problems are smaller than 44 μm.[1-3] Therefore, the use of a microscope is beneficial to investigate samples at relevant spatial scales. In particular, the use of the STXM microscope provides a method whereby the hydrocarbon-clay interactions can be assessed on an adequate spatial scale with a direct and correlative measurement of the carbon surface chemistry and clay mineralogy.

This thesis is focused on model hydrocarbon-clay samples. The obvious choices for clay substrates were illite and kaolinite as they have been found to be the most abundant form of fine clay particles in the oil sands.[21] Illite (general formula $(KH_3O)(Al,Mg,Fe)_2(Si, Al)_4O_{10}$ $[(OH)_2, H_2O]$)[18] has 2 tetrahedral layers with potassium as the main interlayer cation; whereas, kaolinite (general formula $Al_2Si_2O_5(OH)_4$) is a clay mineral that has 1 tetrahedral layer and no cations in its interlayer.[48] An image of these two clays is shown in Figure 1-10. Kaolinites are almost strictly aluminum-silicates (no other ions except Al, Si, O, and H), while illites contain interlayer cations which are

mainly potassium ions.[48] The presence of the potassium is useful for our studies because illite can be easily recognized in NEXAFS spectroscopy by the K 2p edges.

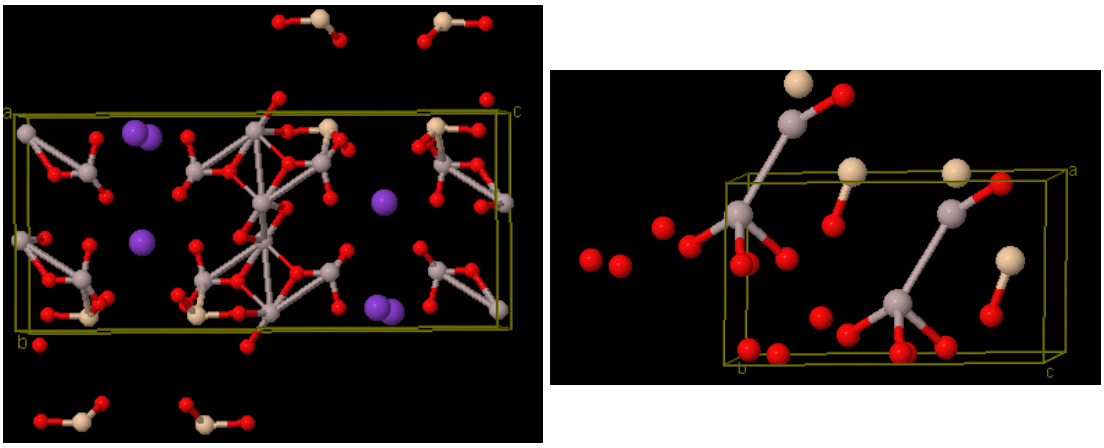

Figure 1-10. Ball and stick images showing the structure of illite (left) and kaolinite (right).[49] (Red= Oxygen, Blue= Potassium, Cream= Silicon, and Grey= Aluminum)

We examined two different model organic species; methylene blue and naphthenic acid. Methylene blue was chosen because it adheres well to the surfaces of clays, and we wanted a definitive model for testing this technique. Methylene blue or similar organic dyes have previously been used to determine the surface coverage of the clays,[50-52] but are not meant to be representative of oil sand hydrocarbons. Naphthenic acids are a complex mixture of saturated aliphatic and alicyclic carboxylic acids, and are known to be a heavy component in the tailings of the oil sands industry.[53] Naphthenic acid was chosen for our second model organic because it contains different functional groups than the ones present in methylene blue. As discussed in chapter 4, naphthenic acid is implicated in tailing contamination.

Methylene blue will emphasize ionic interactions occurring with the clay surfaces, while naphthenic acid will highlight polar interactions with the clay surfaces. The preparation of the model hydrocarbon-clay systems is described in chapter 2.

1.5 Process Samples

In addition to studying model hydrocarbon-clay systems, it is also desirable to study hydrocarbon samples extracted from the oil sands. For this project, our goals include gaining a better understanding of hydrocarbon-clay interactions, which can be obtained using model systems; however, we would like to expand that understanding to process samples. Therefore, we studied a group of process samples consisting of four different bitumen froths. The bitumen froths examined in this thesis have been previously studied by our collaborators at NRCan using light microscopy and confocal laser scanning microscopy.[3] They studied different morphologies in the various bitumen froths in order to relate them to factors affecting oil sands processability. We would like to correlate our chemical spectroscopy with their semi-quantitative morphological studies related to degradation and processability. These results will be discussed in chapter 5.

The process samples investigated arise from the separation procedure in oil sand processing. The separation of oil sands to extract bitumen most commonly uses a water-based flotation technique. The separation process occurs in distinct stages; (1) separation of the bitumen from the fine particles, (2) aeration and finally (3) flotation of the aerated bitumen.[2,17] A schematic diagram of the typical set up of vessels involved in the extraction process is shown in Figure 1-11. The mined oil sands are processed to separate the bitumen from the majority of the sand, clay and other small particulates. Once mixed and processed, the mixture is sent to the settling or separation vessels. In these vessels the major separation occurs into three distinct regions; an upper froth layer, a middle region referred to as the clay-middlings which contains suspended fines, and the lower layer that is normally a dense mass of larger solids.[19] Once this major separation is completed, the

bitumen froths are further purified in other stages shown in the diagram to remove as many of the fine clay particles as possible, while retaining as much of the bitumen as possible.

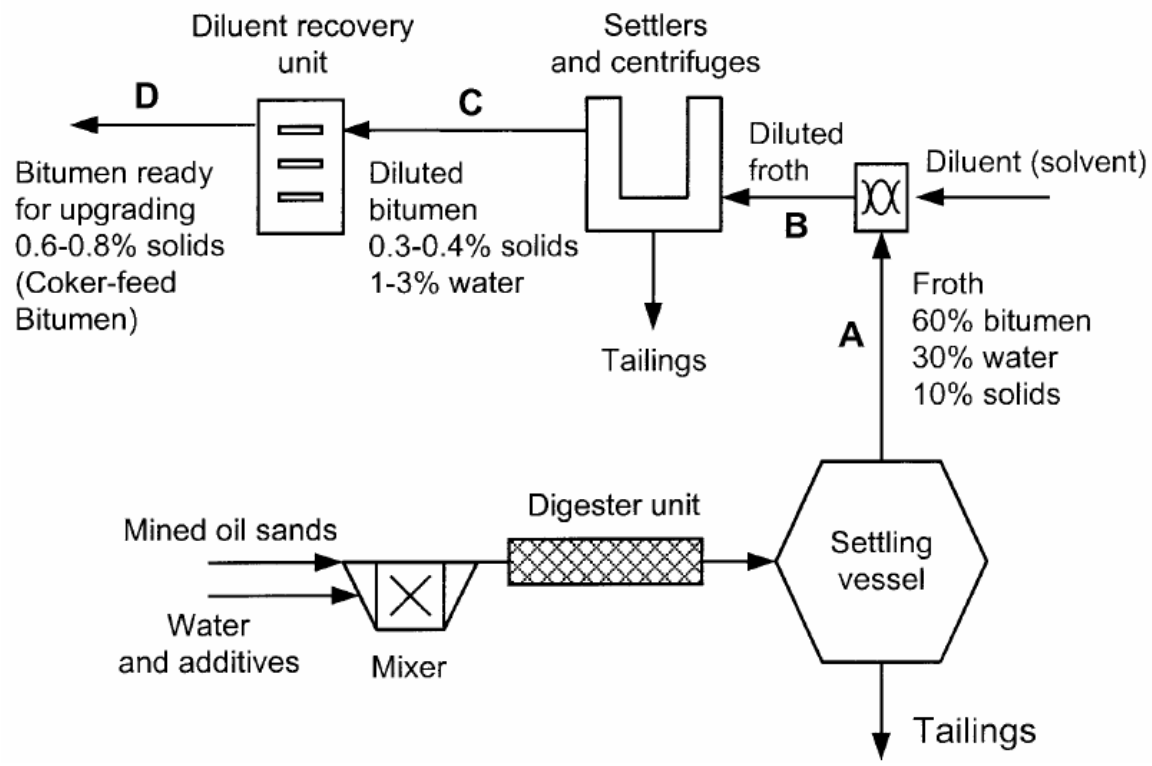

Figure 1-11. Schematic diagram of the bitumen extraction process.[54]

For our experiments, we examined the top layer containing the bitumen froth. All processing samples were obtained from our collaborators, Randy Mikula, Oladipo Omotoso and Vincente Munoz, at CANMET Energy Technology Centre in Devon, Alberta. The samples were prepared in a similar manner, which will be described in detail in the sample preparation section of chapter 2.

1.6 Outline and Goals

Chapter 2 will introduce the experimental techniques used to acquire the data presented for this thesis; STXM spectromicroscopy. The details of the microscope's components, data acquisition methods, and sample preparation considerations will be discussed explicitly. We designed an anticontaminator to reduce photodeposition on our samples in the X-ray microscope and tested our design under a variety of conditions to assess its effectiveness. Chapter 3 will discuss the design, tests and implementation of our anticontaminator for the scanning microscope at the ALS. In chapter 4, we present the experimental results, analysis and conclusions that were obtained from our studies of model clay and model hydrocarbon-clay systems. Chapter 5 describes the experimental findings from our study on the four bitumen froth process samples. Finally, chapter 6 will summarize all of the findings from the thesis, as well as provide suggestions for future experiments that can be performed to extend the findings from this work.

Our original goal for this Masters projected was studying hydrocarbon-clay surface interactions. We discovered that this is a very difficult task as thin layers of carbon present on the clay surfaces can be overpowered by carbon contamination in our clay samples and from the photodeposition on the clay surfaces. Therefore, two developments were required. First we prepared carbon free clays so that we could control the carbon present on the clay surfaces, and secondly, we needed to find a method to reduce carbon contamination from photodeposition. The second goal is addressed thoroughly in chapter 3, where the development and testing of an anticontaminator for STXM 5.3.2 is described. The preparation to achieve carbon free clays is discussed in the sample preparation section of chapter 2. Originally, we were interested in assessing whether clay

surfaces had any preferential binding for specific organic species. Our study of model hydrocarbon-clay systems allowed us to address this question and the results and discussion are provided in chapter 4. An additional goal for this Masters thesis included examination of process samples directly from the oil sands. We wanted to study differences in the organic content of several bitumen froths. These results are thoroughly discussed in chapter 5. Chapter 6 gives a summary of all of the findings from this research and provides some suggestions for future research on this project.

CHAPTER 2

INTRODUCTION TO EXPERIMENTAL METHODS

We propose to use X-ray spectromicroscopy to study hydrocarbon-clay interactions. The experimental details involved in obtaining NEXAFS spectra are outlined in § 2.1, including a description of common spectroscopic detection methods. The resolution of experimental artifacts associated with the operation of the STXM microscope and sample preparation were critical components of this thesis. Section 2.2 describes the STXM microscope instrumentation and experimental methods. The goals and methods of sample preparation are described in § 2.3. Section 2.4 discusses artifacts that arise in X-ray Spectromicroscopy.

2.1 Near Edge X-ray Absorption Fine Structure Spectroscopy

A tunable source of X-rays is required for NEXAFS spectroscopy experiments. Synchrotron radiation is electromagnetic radiation emitted by the acceleration of charged particles (electrons, positrons, etc) moving at relativistic velocities.[33] Synchrotron radiation produces tunable radiation that ranges from microwave to hard X-ray wavelengths. It is used extensively for X-ray spectroscopy and diffraction experiments.

NEXAFS spectroscopy is a core level spectroscopy, where the absorption of X-rays leads to the excitation or ionization of tightly bound core electrons. These excitation features appear as discrete features in the NEXAFS spectra. For instance, the excitation of an electron to an unoccupied molecular orbital produces a pre-edge peak in the absorption spectrum; whereas, the complete ionization of core electrons forms the edge jump in the absorption spectra, the position which corresponds to the binding energy of the electron. Core excited states subsequently relax, causing the ejection of electrons (Auger electrons) or the emission of fluorescence photons.[31] An outline of these processes is illustrated in Figure 2-1.

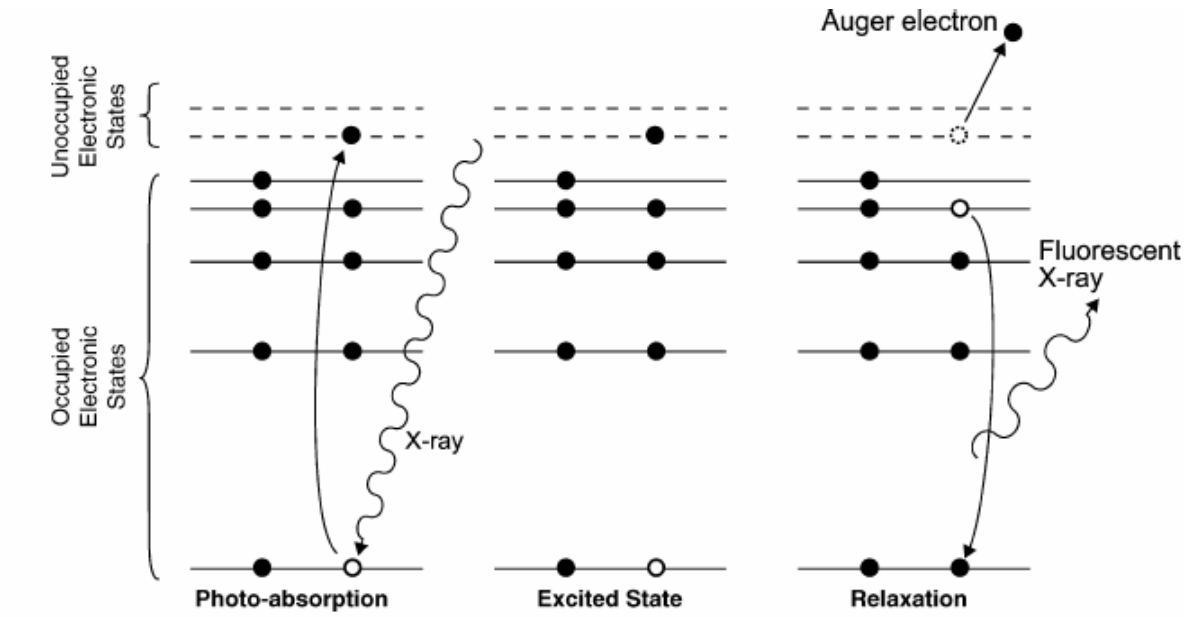

Figure 2-1. Schematic diagram showing the different processes that occur during the X-ray photo-absorption of core electrons during a NEXAFS experiment.[55]

NEXAFS spectroscopy can be detected using several different methods. The three detection techniques include fluorescence detection, electron emission detection, and transmission detection.[55] A schematic diagram illustrating these techniques is shown in

Figure 2-2, and the principles behind them will be discussed below. The main focus will be on transmission detection as this method was used for all experiments presented in this thesis.

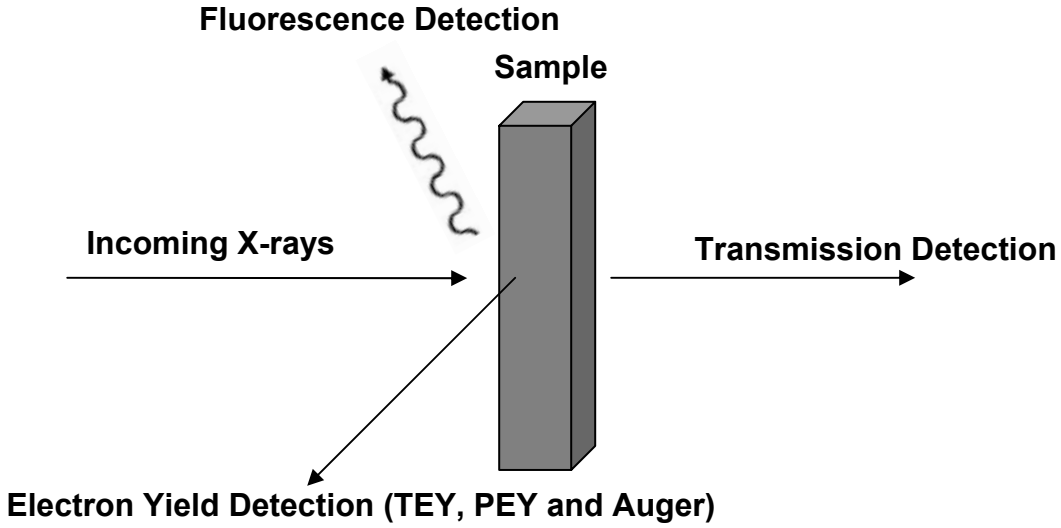

Figure 2-2. Schematic diagram demonstrating the 3 main types of detection used in NEXAFS spectroscopy, fluorescence, transmission and electron yield detection.

2.1.1 Detection Methods

Transmission detection requires measurement of the incident photon beam intensity (Io) and the transmitted photon beam intensity (I). NEXAFS spectroscopy measured in transmission obeys Beer's Law.[55] Therefore, optical density (OD) spectra can be obtained from the transmitted X-ray intensity using the formula,

$$OD = - \ln (I/I_0) \quad (6)$$

where I is the transmitted X-ray flux and I_0 is the incident X-ray flux. Collecting NEXAFS spectra in this manner has the benefit that it can easily be assessed quantitatively by examining the dependence of the absorbance according to

$$A = OD = \mu\rho t = - \ln (I/I_0) \quad (7)$$

where A is absorbance, μ is the energy dependent mass absorption coefficient, ρ is the density, and *t* is the sample thickness. Transmission is normally considered a bulk sensitive technique because the measured signal is averaged over a column through the sample.[55] However, when performing transmission measurements in the soft X-ray region (100-2000 eV), the samples must be very thin for transmission to occur, and thus the surface region contributes greatly to the overall transmission signal.[55]

The other two detection methods, fluorescence and electron emission, are based on detecting the decay of core excited states. Core excited states can decay by radiative mechanisms such as fluorescence and non-radiative mechanisms such as Auger decay.

Once a core vacancy is created in an atom or molecule, a rearrangement occurs to reduce the total energy by filling the hole with an electron from a higher-lying orbital. With fluorescence decay, the creation of the core hole is followed by the emission of a photon of characteristic energy, equal to the difference between the initial and final states.[56] Fluorescence yield detection measures the photons that are emitted via fluorescence decay. As fluorescence decay rapidly follows the creation of a core hole, the X-ray fluorescence signal is proportional to the creation of core excited states through X-ray absorption.[31] This type of detection is considered to be bulk sensitive because X-rays have a longer penetration depth, and can escape from deeper within the sample than electrons. Fluorescence yield detection is also only effective for dilute solids, not concentrated ones.

In competition with fluorescence decay, core excited states can also decay by a non-radiative mechanism, Auger decay. When a core electron is removed from an atom/molecule leaving a vacancy, a second electron from a higher state may fill the hole

causing the release of energy. When this energy is not released as a radiative photon, it can be transferred to an additional electron or electrons in the molecule. The energy causes the electron to be ionized, and for Auger electron yield (AEY), the energy of the ionized auger electron is monitored. Considering Auger electrons have fixed characteristic energies, they are mainly used for elemental characterization in surface and interface analysis.[56]

Subsequent electron scattering will occur in a solid which will create many secondary electrons that can be monitored using partial electron yield (PEY) and total electron yield (TEY). As the electrons approach the surface of the sample material they are scattered inelastically by electron-electron and electron-plasmon interactions, and quasi-eleastically by electron-phonon interactions.[31] Due to scattering within the materials, electrons generated deeper in the solid lose energy more than surface generated electrons. Sample current TEY detects electrons that have enough energy to overcome the work function and to be ejected out at the surface of the sample. Whereas, PEY detects electrons with energy above a chosen energy limit, normally set to exclude low kinetic energy electrons and thus increase surface sensitivity.[55]

2.2 X-ray Spectromicroscopy

This section will describe the STXM microscope used for our experiments, microscopy and spectroscopy measurements and spectral artifacts. The procedures used to acquire experimental data with minimal artifacts will also be described.

STXM microscopy has been extensively used in research involving polymers,[4-6] biological[12,13,57] and environmental[13,15,35,58] samples. STXM microscopy was first

developed by Kirz, Jacobsen, Ade and coworkers at the National Synchrotron Light Source (NSLS), in Brookhaven New York.[42] The STXM allows NEXAFS spectra to be obtained on extremely small sample regions; currently a spatial resolution of approximately 35 nm and an energy resolution of 100 meV can be achieved.[59,60] Images or micrographs can be acquired at energies specified such that they provide the best chemical contrast and sensitivity possible. All measurements for this thesis were acquired using the beamline 5.3.2 STXM microscope at the ALS, which will be discussed in detail in the following section.

2.2.1 STXM 5.3.2 at the ALS

STXM 5.3.2 at the ALS was constructed by a collaboration of scientists from Dow Chemical, the Advanced Light Source, North Carolina State University, McMaster University and several other institutions.[61] The STXM uses Fresnel zone plates to focus the X-ray beam. As diffractive focusing zone plates must be illuminated coherently, STXM microscopes are usually used on undulator beamlines.[6] However, due to the high brightness of the ALS, STXM 5.3.2 is the first of its kind which is capable of running on a bending magnet beamline.[61]

STXM 5.3.2 was specifically designed for polymer studies and thus was designed and optimized for use at the C 1s, N 1s and O 1s edges, covering an energy range from 250 eV to 600 eV. All of the STXM's components are contained within an aluminum vacuum chamber. This microscope chamber allows for samples to be examined in air, in a helium atmosphere or in vacuum (down to 10^{-6} Torr).[60]

The major components of the optics and focusing instrumentation involved with the microscope include Fresnel zone plates (fabricated with a central stop), a spherical-

grating monochromator, a toroidal mirror, and an order sorting aperture (OSA). A schematic diagram of beamline 5.3.2 combined with the optical components involved for the operation is shown in Figure 2-3.

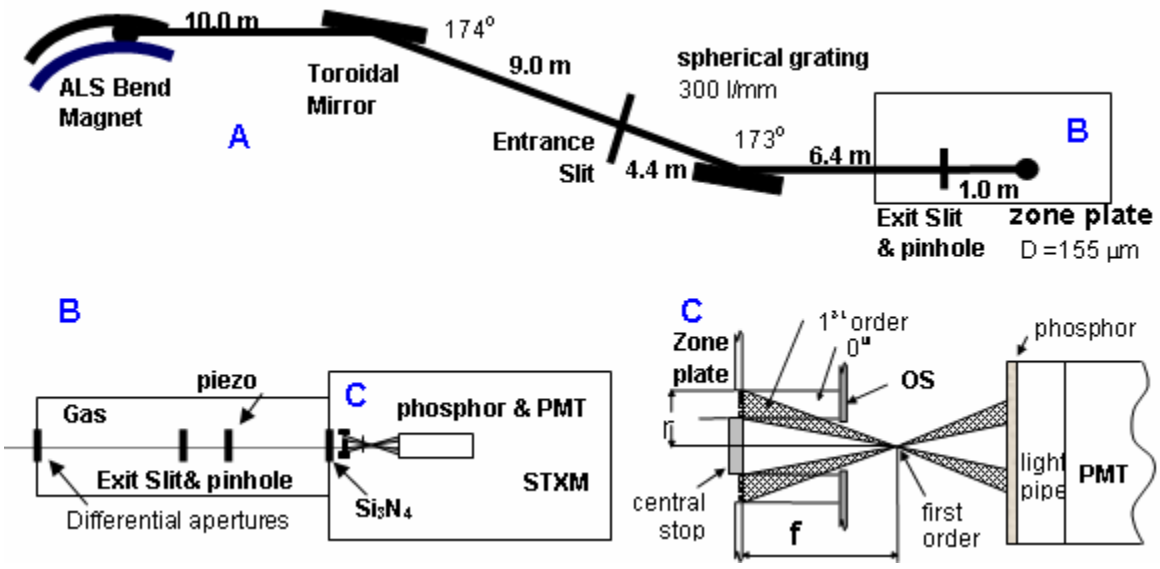

Figure 2-3. Schematic diagram showing the various components of STXM 5.3.2 at the ALS. (A) Beamline; (B) Inside-hutch components and (C) Optical and focusing components of the STXM.[7]

This beamline only uses two main optical surfaces; a toroidal mirror, which focuses light from the bending magnet onto the entrance slit, and a spherical grating mirror which disperses the light horizontally.[61] The spherical grating monochromator operates with energies ranging from 250 eV to 600 eV.

Coherent, monochromatic light illuminates a zone-plate which produces a small X-ray spot by diffractive focusing. The zone-plate contains a central stop, which helps suppress undiffracted light from transmitting through the zone plate and reaching the sample. This signal would contribute to spectral contamination due to non-first order light interacting with various substances present in the sample, outside of the focus. An

order sorting aperture (OSA) is located between the zone-plate and sample such that only first order diffraction reaches the sample.[61] However, it was found that this was not completely efficient, approximately 20% of second order light (e.g. photons with twice the energy, from second order diffraction from the SGM grating monochromator) also reaches the sample.[61] The second order radiation will distort the spectra of thick materials, and create a distortion in the C 1s spectra of oxygen rich materials. To remove the second order light contribution at the carbon edge (~285 eV), a N_2 gas filter was used. A low pressure of nitrogen in the beam path effectively absorbs photons with an energy above the N 1s core edge (~400 eV), reducing higher order contamination at the C 1s edge.

A silicon-nitride window separates the microscope from the beamline (which is kept under ultra high vacuum), from the STXM chamber. The transmitted X-ray flux is measured by converting the flux to visible light using a phosphor window and a photomultiplier (PMT) counts the visible photons with a count rate capacity in the tens of MHz.[60] An image of the phosphor detector used in STXM 5.3.2 is shown below in Figure 2-4.

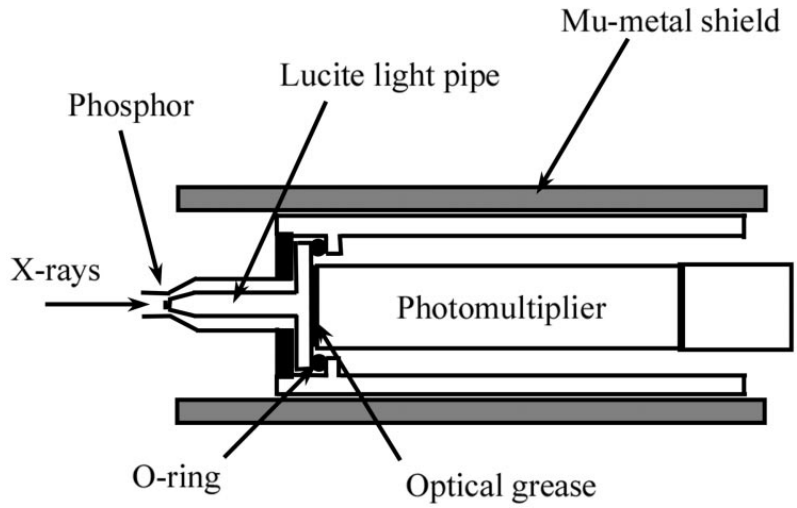

Figure 2-4. Schematic diagram of the detector used in the STXM 5.3.2.[60]

Fresnel zone plates consist of a series of concentric rings which get thinner as the radii get larger.[34] They work as achromatic lenses with the focal length being directly proportional to the photon energy.[60] Therefore, when changing the energy, the STXM microscope must be refocused in synch with the change in the photon energy.[60]

Since the sample should be scanned relative to a stable X-ray beam, STXM microscopes require extremely accurate control of the sample stages. Therefore, STXM 5.3.2 was designed with an interferometer system with two axes (x and y) piezoelectric stages to control fine motion.[60] Interferometer control is important for maintaining the focus positions as the energy is scanned. A schematic diagram showing the design of the components involved in controlling the fine movements of the microscope's operation is provided below in Figure 2-5.

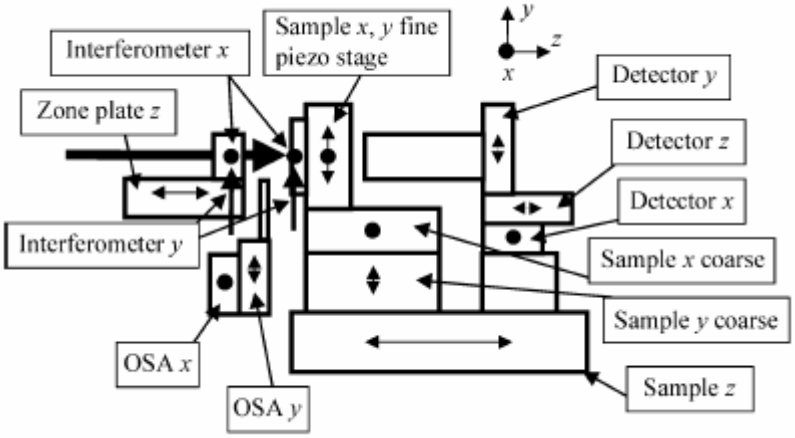

Figure 2-5. Schematic diagram showing the major components used for controlling stage positioning in the STXM.[60]

2.2.2 STXM Modes of Acquisition

The most common signal detected when using a STXM microscope is the photon flux that is transmitted through the sample. In principle, a small focused X-ray beam remains focused in one spot, while the sample is raster scanned through this micro-sized beam. There are four main methods used for data acquisition.

1.) Imaging: The first method involves raster scanning the sample across a small micro-focused beam to produce a micrograph image, at a specific X-ray energy. This first method only produces images, I (x,y). Therefore, this type of data collection is most commonly used for providing survey scans to find interesting regions within the sample, and also for energy specific imaging.

2.) Point Scan: The second method used is point scan mode. To obtain point scans, the beam is focused to a particular location on the sample, and the photon energy is varied to record a spectrum of this sample volume, I (E).

3.) Line Scan: The STXM is used to obtain line scans. Similar to the point scan mode, line scans involve focusing the beam to a specific region of the

sample to obtain NEXAFS spectra. However, unlike point scans, line scans involve raster scanning a straight line across the sample, while varying the photon energy between lines, I (x, E). Line scans can be used to obtain the transmission spectrum of the sample as well as an open area (Io). This is useful because the NEXAFS spectra extracted has a transmitted intensity through the sample (I) and the transmitted intensity through an open area (I_0 incident flux) obtained simultaneously. An image showing a line scan and demonstrating how the data is extracted from the line scan is provided in Figure 2-6**.**

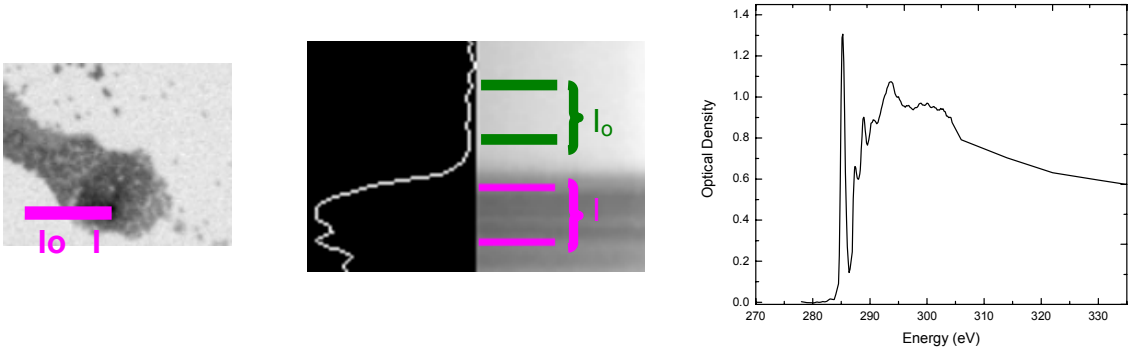

Figure 2-6. (Left) X-ray micrograph image of polystyrene (hυ = 390 eV) with line used for line scan displayed. (Middle) The line scan image based on the line shown in the image to the left. (Right) The C 1s NEXAFS spectrum obtained from the line scan of polystyrene.

4.) Image Sequences: The final and most informative way of obtaining information of samples in the STXM involves collecting small image sequences which are more commonly referred to as stacks. This method was created by *Jacobsen et al.* (2000) using STXM X-1A beamline at the National Synchrotron Light Source (NSLS) at Brookhaven National Laboratory, in Brookhaven, New York.[62] This method involves obtaining a

series of images or micrographs, in a small region of sample, using very small energy spacings, I (x, y, E). Each image must be taken at the proper focus position on the sample to ensure that there is no degradation in spatial resolution.[62] NEXAFS spectra can be extracted from the different regions within the sample by data processing after the experiment.

The best method of obtaining NEXAFS spectra using image sequences involves including a hole or a blank area within the small region used for the image sequence. This allows for simultaneous acquisition of both the incident flux spectrum (Io) and the transmitted flux spectrum (I, through sample) to normalize flux variations that may occur over time.[62] Figure 2-7 illustrates how this technique can be used, and it demonstrates how the NEXAFS spectrum can be extracted from the data set.

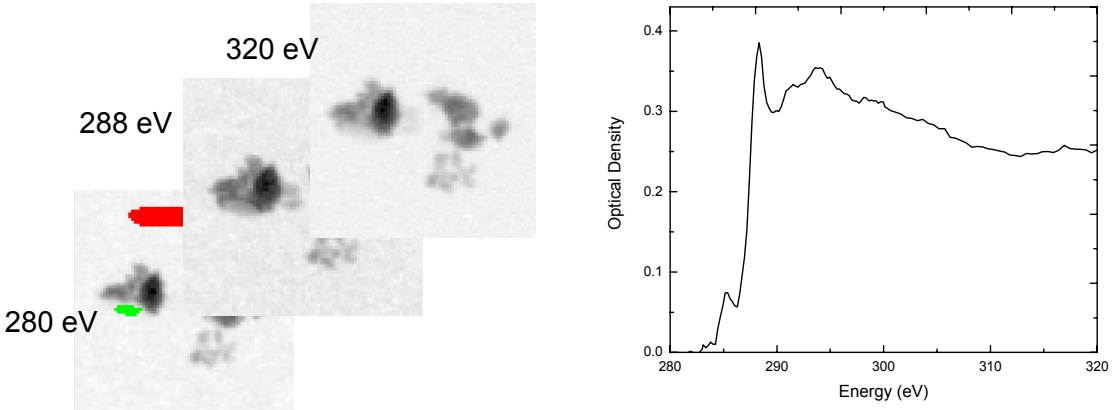

Figure 2-7. (Left) A selection of 3 images from the stack of clays. The green highlights the region used for the I (transmitted intensity, clay particle) and the red region represents the I_o (incident flux). The spectrum on the right is extracted from the stack.

2.3 General Sample Preparation

All NEXAFS data were collected using transmission mode detection in the STXM microscope. One of the major requirements for transmission is that the sample must be

thin enough to ensure that the X-ray beam can penetrate through the sample with a flux which is high enough to limit statistical noise. Sample preparation artifacts must also be avoided. To meet these requirements, samples were prepared by solution casting samples onto a substrate. All of the samples for this thesis were examined using a Si_3N_4 membrane/window (Silson Ltd. and Norcada Inc.) as the substrate. An example of one of these windows is shown in Figure 2-8 below. The membrane portion of the window is between 75 nm (Norcada Inc.) and 100 nm (Silson Ltd) thick. The detailed preparation procedures for all the samples examined are provided in chapters 4 and 5.

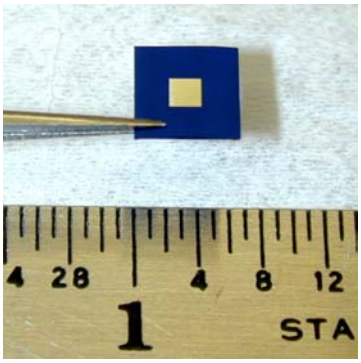

Figure 2-8. An image of a typical Si_3N_4 window used as the substrate for our STXM experiments.

Sources of Samples

The samples used for the experiments reported in this thesis were provided by our collaborators at CANMET Energy Technology Centre Natural Resources of Canada (NRCan, Devon, AB). The model clays (illites and kaolinites) provided came from two major clay banks, the Clay Science Society of Japan and the Source Clay Repository of the Clay Mineral Society, in Georgia. The bitumen froth samples, originated from Suncor Canada and PetroCan, but were provided by our collaborators at NRCan. Most of the samples were prepared in a similar fashion, and the major sample preparation details are

described in chapters 4 and 5. A comprehensive list of the samples examined is provided in Table 2-1.

Sample Name	Sample Number	Sample Source
JCSS 1101 Kaolinite	Model – 1	Clay Society of Japan
Bleached JCSS 1101 Kaolinite	Model – 2	Clay Society of Japan
K-Gβ Kaolin	Model – 3	Georgia Clay Bank
Bleached K-Gβ Kaolin	Model - 4	Georgia Clay Bank
Bleached Illite	Model - 5	US Geological Survey
Naphthenic Acid	Model - 6	NRCan
Methylene Blue	Model - 7	Alfa Aesar
Naphthenic acid and illite	Model - 8	NRCan
Methylene blue and illite	Model - 9	NRCan and Alfa Aesar
Primary froth	Environmental -1	Suncor
Secondary froth	Environmental -2	Suncor
Froth #1	Environmental -3	PetroCan
Froth #9	Environmental -4	PetroCan

Table 2-1. A summary of the sample examined for this thesis.

2.4 Artifacts in C 1s NEXAFS Spectromicroscopy

A major complication that commonly arises in STXM spectromicroscopy is the presence of higher order spectral contamination from the beamline. When the X-ray beam travels through the optics on the STXM beamline, it is diffracted by mirror gratings into different orders (first, second, third etc.). Due to the fact that STXM 5.3.2 was built on a bending magnet beamline, the STXM is much more sensitive to higher order (2^{nd}

and 3rd order) contamination because bend magnets provide a wide distribution of photon energies ("white light"), while undulators produce odd harmonics.[33,60] The third order light is blocked with the use of nickel coatings on the Si_3N_4 window.[61] However, second order light is of a much greater concern because it interferes with C 1s spectra.[61] This is especially important for samples that may contain oxygen because the O 1s absorption (at 543 eV) may appear as second order (at 271 eV) in the C 1s pre-edge region, and we will see oscillations from oxygen 2nd order absorption, distorting the C 1s NEXAFS spectrum. An example of this contamination is exhibited in Figure 2-9, where we can see dip in the spectrum at about 286 eV, and structure in the pre-edge region of the NEXAFS spectrum (270-280 eV).

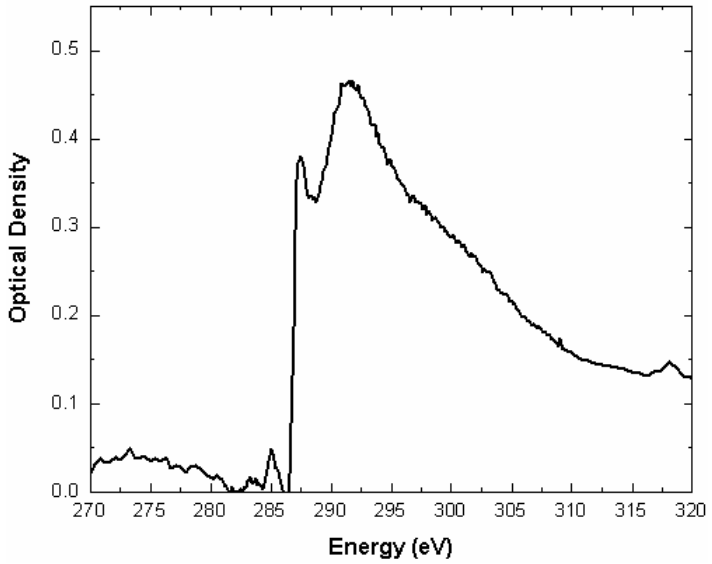

Figure 2-9. A C 1s NEXAFS spectrum that shows distortion below 285 eV due to higher order contamination.

There are a few mechanisms in place to aid in the suppression of this second order light. Proper alignment of both the zone plate and the OSA are important, but the most effective means of eliminating as much of the second order light as possible involves the use of a nitrogen gas filter. The N_2 gas filter consists of a low pressure of nitrogen (400-

500 mTorr) leaked into the vacuum tube. This nitrogen gas filter is used to absorb any light that is greater than 400 eV (N 1s edge), thus preventing most of the higher order contamination from reaching the sample. The filter is not 100% efficient, but it greatly improves the quality of the data and was used for all experiments reported in this thesis.

Another problem in examining C 1s NEXAFS using the STXM arises from carbon photodeposition which interferes with the spectrum of natural carbon contained in the samples. This carbon contamination occurs during X-ray illumination, and photodeposits on the sample as well as the zone plate and Si_3N_4 window, causing distortions in the C 1s NEXAFS spectra of the samples being examined. This becomes evident when samples contain very little inherent carbon, such as our clay samples. In conjunction with collaborators (Dr. Adam Hitchcock Dr. Daniel Hernandez-Cruz, and Jian Wang) at McMaster University, we designed an anticontaminator to help eliminate this problem. The anticontaminator design and experimental validity is currently in preparation for publication and is presented in Chapter 3 of this thesis.

CHAPTER 3

DESIGN AND IMPLEMENTATION OF THE COLD FINGER

One of the major challenges with this project is the study of thin carbon films bound to clay surfaces. This is a difficult task for several reasons. One is the fact that the clay surfaces may contain carbon contaminants. Another reason is that very thin carbon films are difficult to detect because of low signal as well as photodeposition of organic molecules in the STXM chamber. To address the first concern, we use model clays, illites and kaolinites, which have been bleached with hydrogen peroxide and other strong reagents to remove any organic surface contaminants that may be inherently present on the clay's surface. The photodeposition is more difficult to solve.

Most STXM users examine materials with a higher carbon concentration; and would therefore have a strong signal such that the small carbon photodeposition would not be noticeable. In our case, we want to study very thin films of carbon on clays. However, the carbon that photodeposits can easily swamp out the carbon we are interested in. Therefore, we designed, tested and implemented a liquid nitrogen cooled cold trap (or anticontaminator) into STXM 5.3.2 at the ALS. We proved that the use of an in-vacuum, liquid nitrogen cold trap can significantly decrease the amount of carbon that

photodeposits over time in the STXM. This new addition to the STXM has been in use at the ALS in STXM 5.3.2 since the completion of the final design. It was required and used for all of the hydrocarbon-clay studies that will be discussed in this thesis.

The details of the development along with the results and semi-quantitative analysis are in preparation to be submitted to an academic journal for publication. The work is presented in manuscript form, similar to how it will be submitted for publication.

The author of this thesis helped with the design of the cold finger, performed all of the experimental testing and analysis, and prepared the manuscript in close collaboration with Dr. Urquhart. Dr. Hitchcock, Dr. Daniel Hernandez Cruz, and Jian Wang, of McMaster University in Hamilton Ontario, helped with the design and exact measurements required for the creation of the cold finger. They were also helpful with comments and revisions for the manuscript.

The author of this thesis obtained permission from all co-authors to present the work in this thesis.

An anticontaminator for a Scanning Transmission X-ray Microscope

Danielle Covelli,[a] Jian Wang,[b] Daniel Hernandez-Cruz,[b,c] Adam Hitchcock[b] and Stephen Urquhart[a*†]

a.) Department of Chemistry, University of Saskatchewan, Saskatoon, SK, S7N 5C9
b.) Brockhouse Institute for Materials Research, McMaster University, Hamilton, ON, L8S 4M1
c.) Advanced Light Source, Lawrence Berkeley National Laboratory, Berkeley, CA, 94720

Abstract: Scanning Transmission X-ray Microscopy (STXM) is a powerful method for studying the chemical composition of materials at high spatial resolution. However, in most current generation instruments, contamination of the sample, as well as the exit window and the zone plate of the microscope, can occur during X-ray illumination. This carbonaceous deposit reduces the overall transmission and distorts carbon 1s Near Edge X-ray Absorption Fine Structure (NEXAFS) spectra. This can have an adverse impact on studies of materials with low carbon concentrations, as contamination of the sample can quickly swamp the natural carbon NEXAFS spectrum. A liquid nitrogen cooled anticontaminator device has been constructed and added to the polymer STXM microscope at the Advanced Light Source to reduce the partial pressure of organic species that are the source of this contamination. By condensing volatiles onto a cold surface close to the sample, the rate of contamination is significantly decreased. The construction of this anticontaminator is described, its effectiveness is evaluated quantitatively, and its beneficial properties are illustrated.

Manuscript in preparation for submission.

* To whom correspondence should be addressed, stephen.urquhart@usask.ca
† Contribution prepared while on sabbatical leave at the Canadian Light Source (Saskatoon, SK) and at the National Institute for Nanotechnology (Edmonton, AB)

3.1 Introduction

Scanning Transmission X-ray Microscopy (STXM) is a powerful technique for the study of natural and synthetic organic materials. STXM microscopy can provide chemically sensitive imaging by using an X-ray energy that corresponds to a specific X-ray absorption transition, such as the Carbon 1s → π* transition of a phenyl group. By varying the X-ray energy, Near Edge X-ray Absorption Fine Structure (NEXAFS) spectra can be obtained from a small sample region, or a series of STXM images can be acquired at a range of sample energies, providing an image sequence. NEXAFS spectroscopy can provide elemental and chemical (bonding, functional group identity) information,[1-4] orientational information through the linear dichroism of specific NEXAFS transitions,[5] and magnetic information through X-ray magnetic linear dichroism and X-ray magnetic circular dichroism.[6] The combination of high spatial resolution imaging with the chemical sensitivity of NEXAFS spectroscopy is often called X-ray spectromicroscopy. STXM spectromicroscopy is used increasingly for the study of organic materials such as commercial polymers,[7-10] models for soft condensed matter physics,[11] nanostructured organic materials,[9, 12, 13] molecular electronic devices,[14] bioproteins such as silk,[15] and surface bioadhesion.[16] STXM microscopy is also used in the study of molecular environmental sciences[17, 18] as well as magnetization dynamics.[19, 20]

One problem observed in current generation STXM microscopes is sample contamination from X-ray induced photodeposition. When the STXM spot is left focused on a sample for extended time, one observes that the X-ray flux steadily decreases at a much faster rate than the normal decay of the synchrotron beam current. This is due to the build up of

a carbonaceous contamination layer which arises from X-ray induced dissociative adsorption associated with X-ray decomposition of organic species on the sample, which are in turn present due to a significant partial pressure of organic species in the microscope as well as surface creep. These species, which naturally adsorb and desorb from surfaces in the microscope, are believed to be trapped on the X-ray illuminated sample by the X-ray photochemistry. The possible sources of the volatile organic species include lubricants from the mechanical stages and contamination in the microscope from fingerprints and volatile organic samples.

This contamination is a serious problem when analyzing materials that contain a low concentration of carbon, such as thin hydrocarbon films adsorbed to clay surfaces, carbon stabilization in soil,[21] and self assembled monolayers on various substrates, or in cases where very long exposure times (of the order of 10's of seconds on a single spot) are required to measure weak signals, as in studies of magnetization dynamics.[19, 20] In order to reduce this carbon contamination, an in-vacuum liquid nitrogen cold trap (the STXM 'anticontaminator') was designed and tested in the polymer STXM[22] at beamline 5.3.2 at the Advanced Light Source (ALS) in Berkeley, California. This paper reports a quantitative evaluation of the effectiveness of the cold trap on decreasing the rate of contamination in this microscope.

3.2 Experimental

3.2.1 Design and fabrication of anticontaminator

The STXM microscope[22] on ALS beamline 5.3.2[23] can operate in air, in helium atmosphere as well as in coarse vacuum (10 - 100 mTorr). The anticontaminator is a liquid nitrogen cooled surface inside the microscope chamber, upon which contaminants will deposit. A prototype was used to evaluate if an anticontaminator was effective at reducing the rate of carbon build up on samples. It was constructed from commercial plumbing supplies: a short length of copper tube (2" diameter), with end-caps soldered to each end. Thin tubes (1/4") were soldered to this and connected to a conflat liquid nitrogen feedthrough by VCR^{TM} fittings. Solder joints are not recommended for cryo-applications, but were used here for this temporary installation. Figure 3-1 is an image of this anticontaminator. In use, the anticontaminator is cooled by pouring liquid nitrogen into the trap through the feed-through, using a funnel. The exhaust from the liquid nitrogen is able to escape from the second side of the feed-through into air, preventing pressure build-up. After demonstrating the value of the device in reducing the contamination rate, an improved version was designed and fabricated by A.L.D. Kilcoyne. A technical drawing of the final device is shown in Figure 3-2. While there is only one inlet, its diameter is sufficiently large (2.0 cm) to prevent freeze-up and allow escape of N_2 gas.

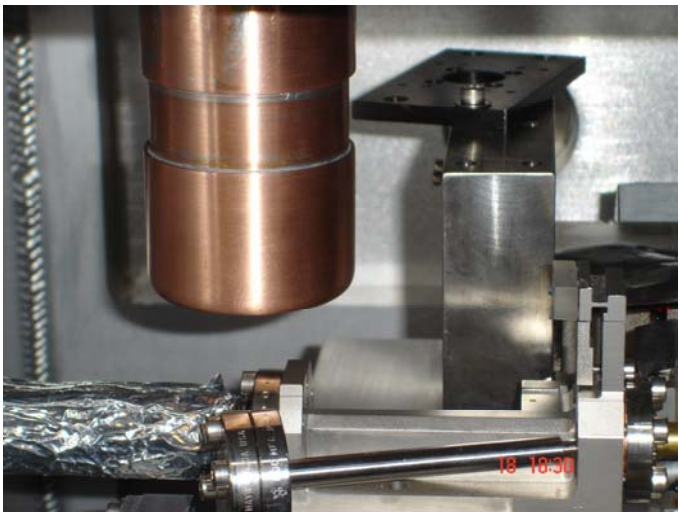

Figure 3-1. Photograph of the prototype cold finger used to evaluate the effectiveness of the anticontaminator concept.

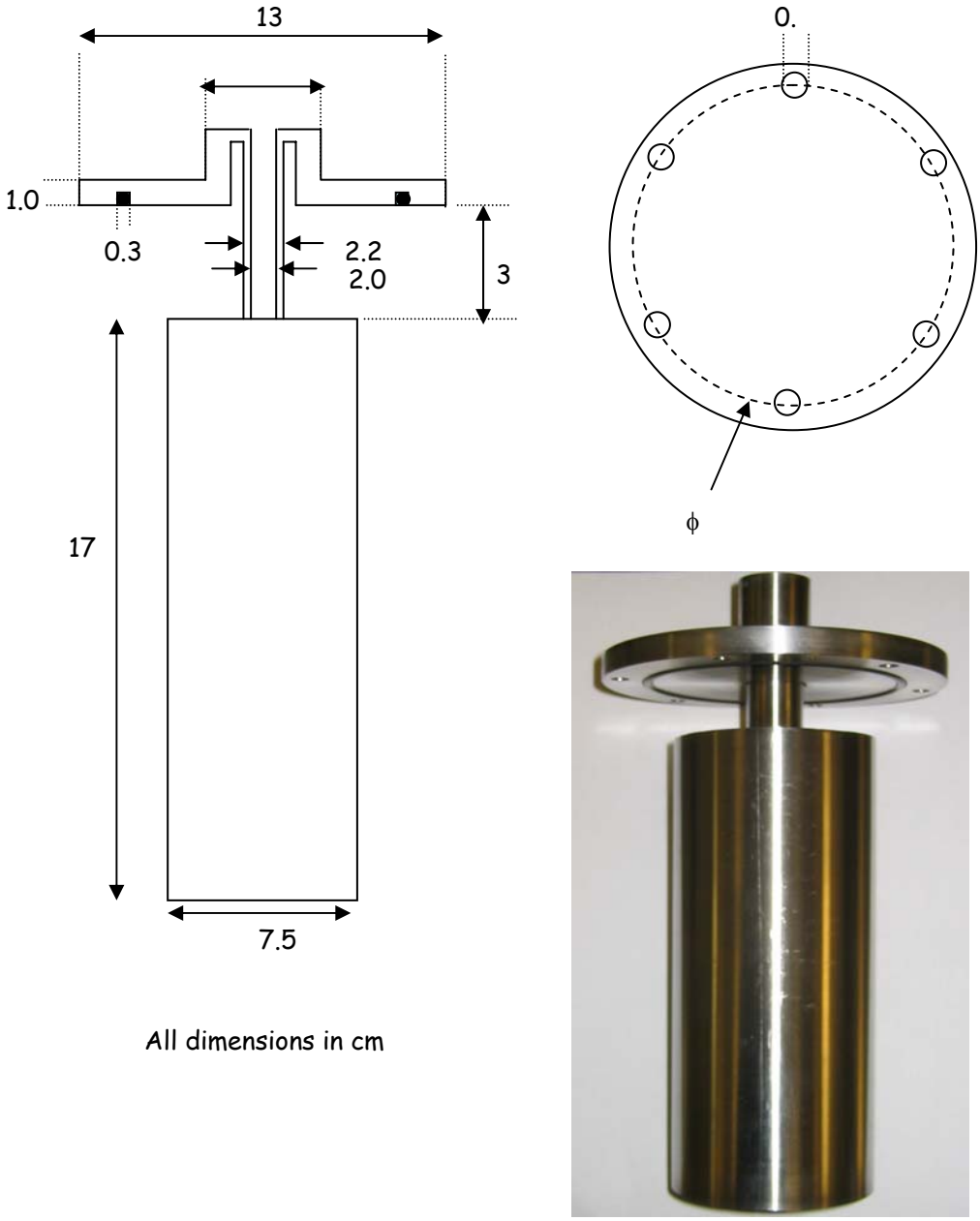

Figure 3-2. Schematic of the final anticontaminator device in the Scanning Transmission X-ray Microscope (Beamline 5.3.2 at the Advanced Light Source).

3.2.2 Photodeposition Procedure

In order to test the effectiveness of the cold trap, the rate of carbon contamination was monitored in several experiments. A clean Si_3N_4 window[24] was used as a substrate to assess the impact of the anticontaminator on the rate of photodeposition of carbonaceous deposits. The deposition experiments were carried out under four distinct conditions:

a.) ambient temperature (no cooling), in a helium atmosphere (250 Torr)
b.) ambient temperature with active pumping using an oil free scroll pump to achieve a pressure <100 mTorr
c.) liquid nitrogen cooled cold trap with active pumping (P<100 mTorr)
d.) liquid nitrogen cooled cold trap in a helium atmosphere (P = 250 Torr)

These four scans were completed within a 36 hour period.

The following procedure was used to induce and quantitatively monitor photodeposition onto the blank window. The zone plate was fabricated by the Centre for X-ray Optics (LBNL) and features a 35 nm outer zone and a 155 micron diameter. The microscope was focused on the edge of the broken fragment Si_3N_4 membrane, which provides a sharp, high contrast feature for attaining a high quality focus. A small, 5 μm x 5 μm region that contains a fragment of a Si_3N_4 window and an open area was imaged at 390 eV, the energy with the greatest intensity on the ALS polymer-STXM beamline. A total dwell time of 15 ms per pixel was used, with a pixel spacing of 50 nm, similar to the spatial resolution of the STXM. The beamline entrance slit was set to 80 or 90 microns, and the exit slits were set to 30 or 45 microns. In these conditions, the measured flux on the sample was 14.8 MHz. With an estimated detection efficiency of 30%[29] and a 50 nm pixel size, a dose rate of approximately 7.7 x 10^6 eV/nm^2/s is realized.

One can measure the photodeposition rate by monitoring the change in transmission of a sample with time while the X-ray beam is left focused on a single point. However, exposure of a larger square area allows acquisition of C 1s spectra during and after the exposure, and also provides a more precise way to evaluate the accumulated dose. The amount of carbonaceous contamination deposited as a function of X-ray exposure was measured by recording a spectrum of the exposed region using a 1 μm defocused beam. A point spectrum was also acquired in an open area in order to obtain the incident beam (I_0) spectrum so that optical density could be calculated. Cycles of long dwell time exposure followed by a defocused carbon 1s spectrum of the area, were repeated until a significant carbon build-up was observed and characterized spectroscopically.

3.3 Calculations

3.3.1 Radiation dose calculation

In order to quantify the effectiveness of the cold trap, the radiation exposure was calculated according to the following formula:

$$\text{Radiation Dose} = \frac{N\, n\, E}{A\, \eta} \qquad (1)$$

where N represents the number of photons per pixel absorbed, *n* indicates the number of pixels, E is the energy, A is the image size and η is the detector efficiency. This formula provides radiation dose in units of eV/nm^2. Typically, radiation doses are expressed in units of eV/volume (e.g. nm^3),[25, 26] or Gray (J / kg), where the volume (or mass) is determined by sample thickness. Since we are depositing a thin film whose thickness

increases with dose, the sample volume and thus the absorbed dose increases with time. For this reason the radiation dose is reported in areal units, eV/nm^2. The detector efficiency at 300 eV has been previously estimated to be 30%,[22, 27]and therefore this value was used for these calculations.

3.3.2 Relative rate of carbon photodeposition

To perform quantitative analysis, the transmitted signal is converted to optical density through:

$$OD = - \ln (I/I_0) = \mu\rho t \qquad (2)$$

where I_0 is the incident X-ray flux, I is the transmitted flux through an area of the sample, μ is the mass absorption coefficient, ρ is the density, and *t* is the sample thickness. Since the rate of photodeposition will depend on the microscope's history, we focus on the *relative* rates of deposition under the different operating conditions discussed above. All experiments were performed within 36 hours to avoid variation in the cleanliness of the microscope.

3.4 Results

3.4.1 Spectroscopic observations

Figure 3-3 presents the carbon 1s NEXAFS spectra of the Si_3N_4 window after being exposed to the four different conditions described above, normalized to a common intensity scale for comparison and offset for clarity. The spectra do not vary with deposition conditions, and provide some clue to the chemistry of the contaminant film. A C 1s $\rightarrow$ $\pi^*_{C=C}$ transition at 285 eV is characteristic of aromatic phenyl groups or carbon-

carbon double bonds. The shoulder at ~288 eV may represent unsaturated carbon (1s → σ^*_{C-H} transitions) or carboxylic functionalities (e.g. C 1s → $\pi^*_{C=O}$ transitions).[2]

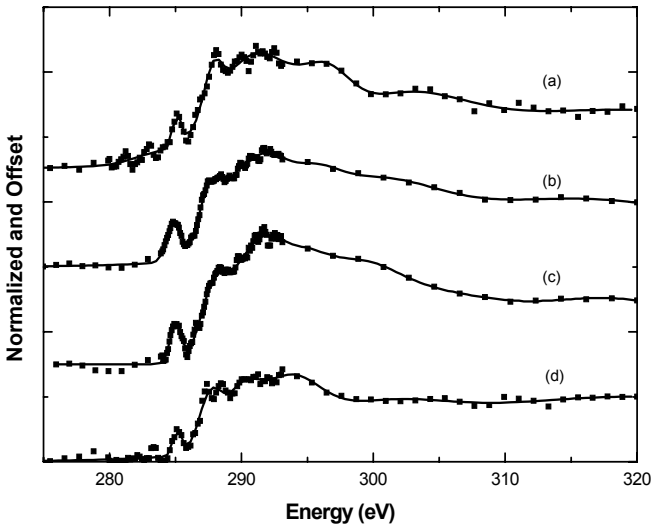

Figure 3-3. C 1s NEXAFS spectra of the photoinduced contamination deposit under different experimental conditions: (a) Liquid nitrogen cooled and helium atmosphere; (b) Ambient temperature and active pumping; (c) Ambient temperature and helium atmosphere; (d) Liquid nitrogen cooled and active pumping. These spectra have been offset for clarity.

In order to determine the relative contamination rate, the accumulation of contamination is examined as a function of radiation dose. presents a plot of the deposition of organic species as a function radiation dose for the 4 experimental conditions described above. The areal optical density, integrated over the range 284-293 eV, is used to provide a measure of the carbon build-up with better statistical precision than measuring the optical density at a single energy. These spectra were first subjected to a 5 point Savisky-Golay smoothing and the background signal from absorption by the Si_3N_4 window was subtracted. Axis2000[28] was used for all data processing.

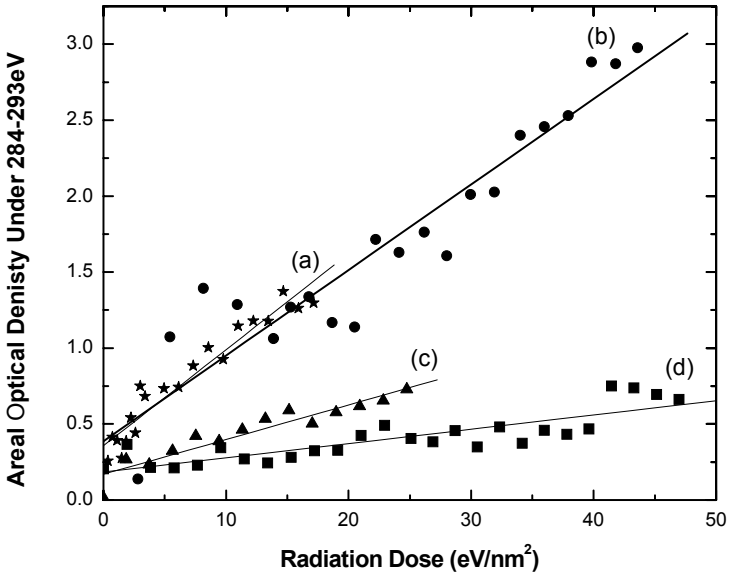

Figure 3-4. Plots of the integrated areal optical density of carbon as a function of radiation exposure.

The rate of contamination can be quantified by determining the slope of the deposition versus dose traces in . The results of linear least squares fit are presented in Table 1. The fit quality is highest when the rate of contamination is highest. When the rate of deposition is very low, other experimental variations can become more significant and decrease the quality of the fit.

Conditions	Liquid N_2 Cooling?	Rate of Contamination [(a)]	Y Intercept	Fit quality (R^2)
active pumping	N	$6.3 \times 10^{-2} \pm 4.2 \times 10^{-3}$	$3.6 \times 10^{-1} \pm 3.7 \times 10^{-2}$	0.92
250 Torr He	N	$5.6 \times 10^{-2} \pm 4.7 \times 10^{-3}$	$3.9 \times 10^{-1} \pm 1.3 \times 10^{-1}$	0.88
active pumping	Y	$2.3 \times 10^{-2} \pm 2.3 \times 10^{-3}$	$1.7 \times 10^{-1} \pm 3.3 \times 10^{-2}$	0.89
250 Torr He	Y	$9.4 \times 10^{-3} \pm 1.2 \times 10^{-3}$	$1.8 \times 10^{-1} \pm 3.2 \times 10^{-2}$	0.72

Table 3-1. Rate of contamination as function of experimental conditions

(a) The rate is the slope of the plot of integrated areal optical density versus dose (Fig 4), with units of eV^{-1} nm^2

The rate of contamination is similar for both conditions where the cold trap is not used. We interpret this to indicate that the arrival / residence rate of contaminants on a Si_3N_4 surface is the same whether the system is at $1/3^{rd}$ atmosphere He or vacuum. When the cold trap is used with continuous pumping, the rate of contamination is reduced approximately 3 fold relative to when the trap is not used. When the cold trap is used with a helium atmosphere inside the STXM, the rate of contamination is reduced approximately ~7 fold when compared to the conditions without the cold trap. The reduced rate of contamination when backfilled with He (~250 Torr) may be attributed to convective cooling of the microcope's internal surfaces in the He atmosphere, as well as the increased rate of out-gassing of microscope stages when in vacuum. After an extended experimental run with the cold trap in a helium atmosphere, the internal surfaces of the STXM microscope are found to be slightly below room temperature. These comparisons are approximate, given the quality of the fit and other uncertainties, but the data clearly show a significant difference when the cold trap is used in a helium atmosphere.

It has been anecdotally observed that the rate of contamination can be reduced if the microscope is kept constantly pumped. These experiments were performed immediately after the inside of the STXM microscope was cleaned. Otherwise, the microscope conditions were kept constant to the extent possible: helium backfill was performed immediately after the microscope was pumped down to <100 mTorr. Experiments under constant pumping were performed shortly after the microscope was pumped down to <100 mTorr.

3.4.2 Sample drift

A significant sample drift *(0.02 microns per minute)* was observed when active pumping (<100 mTorr) was used in the STXM microscope. This sample drift was not observed when the microscope was backfilled with helium (~250 Torr). We speculate that the helium atmosphere provides some convective cooling for the microscope's stages and 3components, reducing out-gassing and therefore the partial pressure of organic molecules to photodeposit. When using constant pumping, the microscope stages can sometimes drift due to thermal expansion. In order to obtain the C 1s NEXAFS spectra with minimal drift and photodeposition contamination, it is desirable to backfill the microscope with helium.

3.4.3 Kinetics of Photodeposition

The linear increase in contamination with dose observed in Figure 4 is in sharp contrast to the exponential-like form of radiation damage kinetics. When polymers are irradiated by soft x-rays, the intensity of specific electronic transitions can increase or decrease and mass-loss of the polymer can occur. Frequently, plots of the evolution of optical density versus dose due to radiation damage have an exponential or an exponential-like behavior.[25, 26] This behavior can be attributed to pseudo-first order reaction kinetics, where the rate of damage is proportional to the quantity of undamaged polymer remaining.

Contamination through photodeposition has been studied for the semiconductor photolithography industry.[29, 30] The photodeposition rate is difficult to simulate as many different photochemical reactions can occur in the gas phase and on the surface.

Recently, Kunz et al [30] studied the photodeposition of trace levels (ppb to ppm) of organic contaminants such as hydrocarbons on optics used for lithography. They apply a mass-deposition model to describe the surface photochemical reactions, with parameters that include the surface coverage of the adsorbed precursors, the photoabsorption cross section and quantum yield of the precursors, and the photon flux. In this model, the deposition rate has a high-order dependence on the exposure time when the surface is partially populated by contamination nuclei, but the rate becomes linearly dependent on exposure time when a continuous contamination film is formed. Our photodeposition measurements in the STXM microscope are clearly in the continuous coverage limits, as a substantial coverage is required for a measurable optical density.

3.5. Discussion and Conclusions

Our results suggest that an anticontaminator may be useful for reducing carbon deposition on beamline optics when they are first exposed to the X-ray beams. When first exposed to a beam, the pressure in the optical chamber rises as out-gassing occurs. If the partial pressure of these outgassed species can be decreased during this X-ray exposure, then the rate of X-ray induced photodeposition on the mirror or grating will decrease, and with this the amount of contamination on the optical element will be decreased. Similarly, consistent use of an anticontaminator may be effective in reducing the rate of carbon buildup on windows and zone plates in STXM, thus extending their life, and the time between changes.

This paper described the development and testing of an anticontaminator, a cold trap to reduce the rate of carbon contamination from X-ray induced photodeposition on samples

in the STXM, The anticontaminator was tested with active pumping and with the chamber backfilled with helium. It was found that using it with a partial atmosphere of He provided the greatest reduction in the rate of contamination. These tests have proved that the liquid nitrogen cooled anticontaminator is successful at significantly suppressing the rate of carbon photodeposition inside the STXM chamber. The anticontaminator apparatus (Figure 2) is now in regular use in the polymer STXM microscope.

Acknowledgements

We thank A.L.D. Kilcoyne for his work in developing and maintaining STXM 5.3.2 at the ALS, and T. Tyliszazak for helpful discussions. We acknowledge the University of Saskatchewan Physics Machine Shop for the fabrication of the temporary model of the cold trap that was used for these tests and A.L.D. Kilcoyne for the design of the permanent stainless steel cold trap. The research was supported by Natural Sciences and Engineering Research Council, the Canadian Foundation for Innovation and Canada Research Chair. The Advanced Light Source (ALS) is supported by the Director, Office of Science, Office of Basic Energy Sciences, of the U.S. Department of Energy under Contract No. DE-AC03-76SF00098. The use of the NCSU-McMaster-Dow-ALS Polymer STXM microscope (BL 5.3.2) at the ALS is supported by the National Science Foundation (DMR-9975694), the Department of Energy (DOE, DE-FG02-98ER45737), Dow Chemical, an NSERC Major Facilities Access grant, and CFI.

References:

[1] J. Stöhr, NEXAFS Spectroscopy, Springer-Verlag, 1992.

[2] S.G. Urquhart, H. Ade, Journal of Physical Chemistry B 106 (2002) 8531.

[3] R.R. Cooney, S.G. Urquhart, Journal of Physical Chemistry B 108 (2004) 18185.

[4] A.P. Hitchcock, D.C. Mancini, Journal of Electron Spectroscopy and Related Phenomena 67 (1994) 1.

[5] J. Stöhr, D.A. Outka, Physical Review B 36 (1987) 7891.

[6] J. Stöhr, H.C. Siegmann, Magnetism: From Fundamentals to Nanoscale Dynamics, Springer, Berlin, 2006, p. 820.

[7] E.G. Rightor, S.G. Urquhart, A.P. Hitchcock, H. Ade, A.P. Smith, G.E. Mitchell, R.D. Priester, A. Aneja, G. Appel, G. Wilkes, W.E. Lidy, Macromolecules 35 (2002) 5873.

[8] S.G. Urquhart, A.P. Hitchcock, A.P. Smith, H.W. Ade, W. Lidy, E.G. Rightor, G.E. Mitchell, J. Electron Spectrosc. Relat. Phenom. 100 (1999) 119.

[9] A.P. Hitchcock, I. Koprinarov, T. Tyliszczak, E.G. Rightor, G.E. Mitchell, M.T. Dineen, F. Hayes, W. Lidy, R.D. Priester, S.G. Urquhart, A.P. Smith, H. Ade, Ultramicroscopy 88 (2001) 33.

[10] G.E. Mitchell, L.R. Wilson, M.T. Dineen, S.G. Urquhart, F. Hayes, E.G. Rightor, A.P. Hitchcock, H. Ade, Macromolecules 35 (2002) 1336.

[11] S. Zhu, Y. Liu, M. H. Rafailovich, J. Sokolov, D. Gersappe, D. A. Winesett, H. Ade, Nature 400 (1999) 49.

[12] J. Fu, S.G. Urquhart, Langmuir 23 (2007) 2615.

[13] R. Takekoh, M. Okubo, T. Araki, H. Stöver, A.P. Hitchcock, Macromolecules 38 (2005) 542.

[14] C.R. McNeill, B. Watts, L. Thomsen, W.J. Belcher, N.C. Greenham, P.C. Dastoor, Nano Letters 6 (2006) 1202.

[15] D. Hernandez-Cruz, M.-E. Rousseau, M.M. West, M. Pezolet, A.P. Hitchcock, Biomacromolecules 7 (2006) 836.

[16] C. Morin, A.P. Hitchcock, R.M. Cornelius, J.L. Brash, S.G. Urquhart, A. Scholl, A. Doran, Journal of Electronic Spectroscopy and Related Phenomena 137-140 (2004) 785.

[17] J.J. Dynes, T. Tyliszczak, T. Araki, J.R. Lawrence, G.D.W. Swerhone, G.G. Leppard, A.P. Hitchcock, Environmental Science and Technology 40 (2006) 1556.

[18] G.E. Brown Jr., K. Benzerara, T.H. Yoon, J. Ha, C.D. Cordova, A.M. Spormann, T. Tyliszczak, K.S. Tanwar, T.P. Trainor, P.J. Eng, T. Kendelwicz, S. Yamamoto, H. Bluhm, G. Ketteler, M. Salmeron, A. Nilsson, Geochimica et Cosmochimica Acta 70 (2006) A69.

[19] B. Van Waeyenberge, A. Puzic, H. Stoll, K.W. Chou, T. Tyliszczak, R. Hertel, M. Fähnle, H. Brückl, K. Rott, G. Reiss, I. Neudecker, D. Weiss, C.H. Back, G. G. Schütz, Nature 444 (2006) 461.

[20] Y. Acremann, J.P. Strachan, V. Chembrolu, S.D. Andrews, T. Tyliszczak, J.A. Katine, M.J. Carey, B.M. Clemens, H.C. Siegmann, J. Stöhr, Physical Review Letters 96 (2006) 217202.

[21] J. Kinyangi, D. Solomon, B. Liang, M. Lerotic, S. Wirick, J. Lehmann, Soil Science Society of America Journal 70 (2006) 1708.

[22] A.L.D. Kilcoyne, T. Tyliszczak, W.F. Steele, S. Fakra, A.P. Hitchcock, K. Franck, E. Anderson, B. Harteneck, E.G. Rightor, G. Mitchell, L. Yang, T. Warwick, H. Ade, Journal of Synchrotron Radiation 102 (2003) 125.

[23] T. Warwick, H. Ade, A.L.D. Kilcoyne, M. Kritscher, T. Tylisczcak, S. Fakra, A.P. Hitchcock, P. Hitchcock, H.A. Padmore, Journal of Synchrotron Radiation 9 (2002) 254.

[24] Norcada Inc., www.norcada.com.

[25] E.G. Rightor, A.P. Hitchcock, H. Ade, R.D. Leapman, S.G. Urquhart, A.P. Smith, G. Mitchell, D. Fischer, H.J. Shin, T. Warwick, Journal of Physical Chemistry B 101 (1997) 1950.

[26] T. Coffey, S.G. Urquhart, H. Ade, Journal of Electron Spectroscopy and Related Phenomena 122 (2002) 65.

[27] J. Wang, C. Morin, L. Li, A.P. Hitchcock, A. Scholl, A. Doran, submitted to the Journal of Electron Spectroscopy and Related Phenomena (2006) .

[28] A.P. Hitchcock, Axis2000 (2006).

[29] R.L. Jackson, T.H. Baum, T.T. Kodas, D.J. Ehrlich, G.W. Tyndall, P.B. Comita, in: D.J. Ehrlich and J.Y. J.Y. Tsao (Eds.), Laser Microfabrication - Thin Film Processes and Lithography, Academic Press, Boston, 1989, p. 385.

[30] R.R. Kunz, V. Liberman, D.K. Downs, Journal of Vacuum Science and Technology B 18 (2000) 1306.

CHAPTER 4

RESULTS AND DISCUSSION: MODEL ORGANIC-CLAY SYSTEMS

The goal of this project was to understand how different organic species interact with clay surfaces to facilitate a better understanding of the behavior of clays in oil sand processing. To achieve these goals, we have developed characterization methods that allow us to study the adsorption of organic species on clay surfaces. Our study starts with examination of controlled model systems. Our control experiments include a set of two model clays, two organic species and mixture of these, to assess the presence or absence of any preferential interactions that may occur between the hydrocarbon model species and model clay particles. In this chapter, § 4.1 gives details on difficulties encountered in data analysis and provides explanations on how these problems were overcome for our analysis. In § 4.2, the studies of the model clays, including sample preparation, results and discussion are addressed. Section 4.3 describes the sample preparation, spectral assignments and analysis of the model organic species. The preparation, results and discussion of the hydrocarbon-clay studies are provided in § 4.4. Section 4.5 gives a brief summary of the results obtained from these experiments.

4.1 Problems with STXM Analysis

All of the model clays, model organic species and mixtures of the two were examined in the STXM microscope at beamline 5.3.2 at the ALS. For all data obtained, the STXM

was run with a helium atmosphere inside the main chamber, using the N_2(g) filter (400-500 mTorr pressure) to reduce higher order light contamination (as discussed in §2.4), and using the liquid nitrogen cold trap to reduce carbon contamination (as described in chapter 3). However, when studying our model systems, we discovered two new challenges that impeded our ability to analyze our data appropriately.

The first problem was obtaining proper spectral normalization. Since transmission detection was used for our experiments, a clean Io spectrum is required for proper normalization. Ideally, using the STXM, normalization can be done by obtaining an I and Io spectrum simultaneously using image sequences (§ 2.2). However, for surfaces of organic model species and organic models mixed with clays, obtaining proper normalization was very difficult because a thin layer of organic species is sometimes found in the region that would normally be used as the Io. The three different normalization conditions encountered are shown below in Figure 4-1. Figure 4-1 (a) shows how our ideal normalization works. A blank area near the clay particles would be used for normalization. Figure 4-1 (b) shows the major complication that surfaced for the organic and organic-clay samples. The normalization was troublesome because the surface of the Si_3N_4 membrane was coated with a thin layer of organic species, therefore causing normalization artifacts. These normalization artifacts include features in the spectra which should not be present, such as dips in the carbon pre-edge region, and suppression of carbon pre-edge peaks. These artifacts occur when an Io which is not from a completely blank substrate is used for normalization. Figure 4-1 (c) exemplifies the technique we used to remove normalization artifacts that appear from the presence of an organic film covering the entire substrate. An external source, a blank substrate, was used

for normalization (external normalization). Although this method works, it is not perfect because the Io cannot be obtained simultaneously with the I spectrum, therefore slight variations in photon flux need to be taken into account for correct normalization.

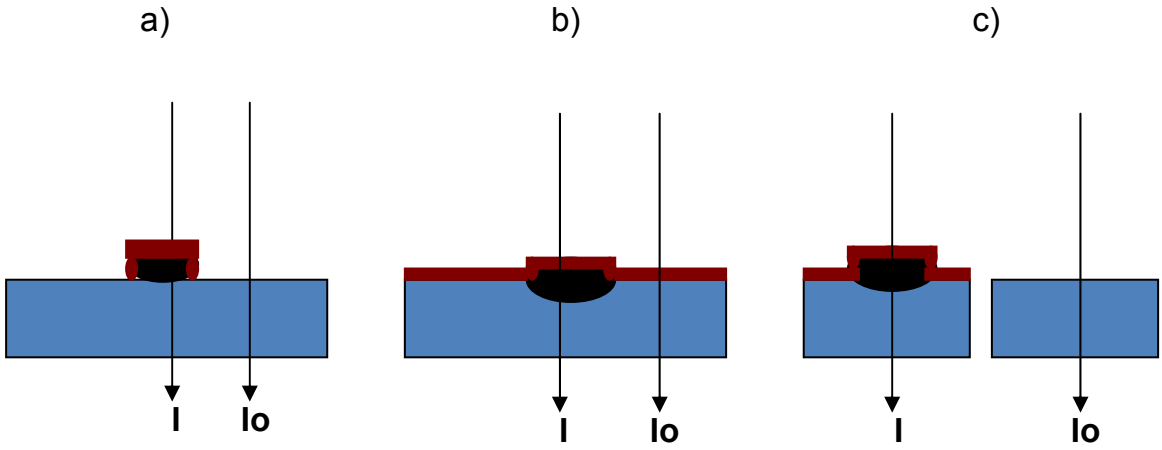

Figure 4-1. Illustration of the 3 types of normalization; a) Ideal normalization, b) Poor normalization (organic film obstructing the Io), and c) External normalization to avoid artifacts from the organic film.

The spectra of pure organic models and model organic-clays require very careful normalization to ensure the absence of spectral artifacts. Improper sample preparation can lead to the organic film covering the entire surface of the substrate as seen in Figure 4-1 (b). These artifacts can occur, as in case "b" of Figure 4-1, because the I and Io are identical except for the clay absorption. Therefore, when converting to O.D., the beamline variation, absorption by the substrate membrane also present in the carbon film is cancelled out.

An example of a typical "blank" area that would be used as the Io spectrum for normalization is illustrated in Figure 4-2. However, when this type of Io was used for normalization, some of the carbon peaks in the spectra of the model organics and model organic-clay spectra were distorted, and in some cases completely suppressed. An

example of this distortion and peak suppression can be seen below in Figure 4-3. Spectrum "a" was obtained using an Io taken from the Si_3N_4 membrane near the sample which we believe is contaminated by a thin carbon film (as shown in Figure 4-2) and spectrum "b" used an external Io, obtained from a blank Si_3N_4 membrane. Examination of these two spectra indicates spectrum "a" is missing a peak at 285 eV, which is clearly visible in spectrum "b". To further exhibit this point, Figure 4-4 shows a spectrum of the background near the sample used for I, normalized using an external source as Io. This background near the clay particles (used as the Io for spectrum "a" in Figure 4-4) shows a strong absorption peak at 285 eV. This peak corroborates our reasoning for the disappearance of the 285 eV peak in spectrum "a" and validates our use of external normalization for organic containing samples. A thin organic film appears to coat the Si_3N_4 window during sample preparation.

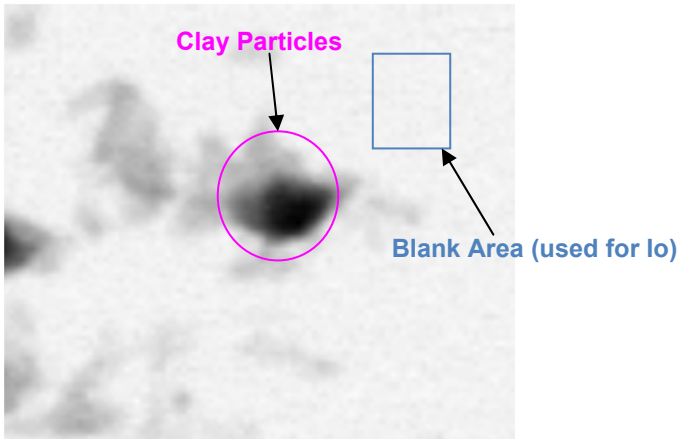

Figure 4-2. STXM micrograph of a clay sample, highlighting the clay particles and the typical background near these particles that could be used for Io.

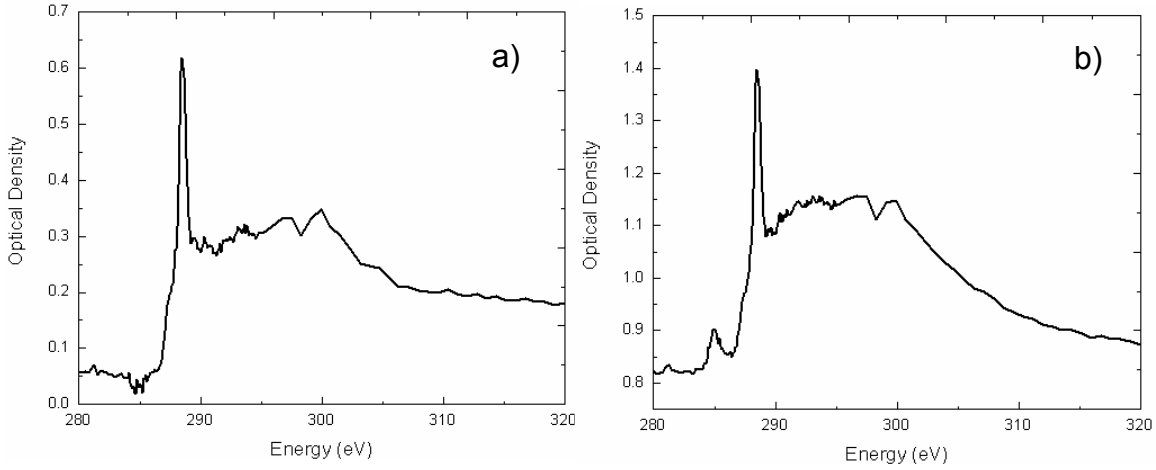

Figure 4-3. C 1s NEXAFS spectra of a sample of naphthenic acid a) normalized using a region of Si_3N_4 membrane near the sample, and b) normalized using an external source (blank Si_3N_4 membrane).

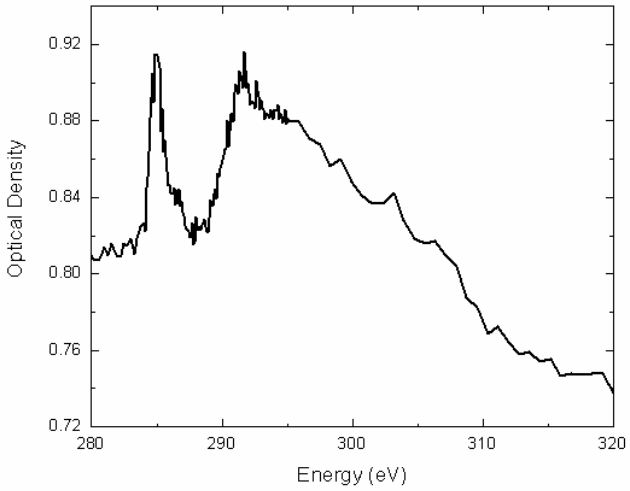

Figure 4-4. C 1s NEXAFS spectrum of the substrate background near the organic sample, normalized using an external source for Io.

The second, more difficult problem encountered with data processing and analysis was only found when examining the mixture of organic models with bleached illite. We used external normalization for these samples, but encountered additional complications, all of which are not completely understood. A "dip" occurs in the spectrum located at

approximately 285-286 eV. In some instances, only a dip before the peak at 285 eV would be seen, while in other cases the dip almost completely suppresses the peak. An example of this is shown in Figure 4-5.

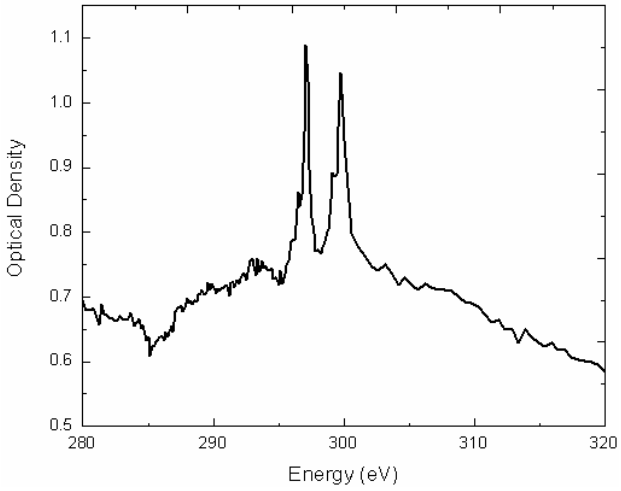

Figure 4-5. An example of a C 1s NEXAFS spectrum of organic-illite distorted by a "dip" at 285 eV.

Despite the fact that we were normalizing the spectra using carbon free external normalization, we could still not obtain clean spectra for many of our organic-clay samples. The dip at 285 eV was distorting a significant portion of the carbon pre-edge region which was of significant interest in our studies. It was suggested that this dip could be arising as an effect of contamination from second order light even though we were using the N_2 gas filter.[63] Second order light is a large concern, especially using STXM 5.3.2 because of high intensity from the bend magnet, but there are several tools used to eliminate the contamination, all which were implemented for our experiments.

However, if the clays contained a large amount of oxygen, then even a small amount of second order light would distort the spectra. A beamline scientist at the ALS, Dr. Tolek Tyliszczak, indicated a method he commonly uses to remove artificial dips from

data. The method involved subtracting a constant from the I spectrum of the sample, to account for higher order contamination due to the presence of oxygen. To understand this suggestion, it is important to examine the equation used to create the spectra originally. Because we are using transmission, our optical density spectra arise from using Beer's Law:

$$OD = -\ln (I/Io).$$

However, when 2nd order light is present in the chamber, we have a slightly modified equation;

$$OD = -\ln ((I+b)/(Io+b'))$$

where b and b′ are unknown constants corresponding to transmission by higher order photons. The unknown constants should not cause a problem because they are present in both the I and Io spectra, unless the signal level is low (I not much greater than b). We speculate that a difference occurs because the I spectrum is transmitted through the Si_3N_4 membrane and the clay particles while the Io spectrum is only transmitted through the membrane thus providing different values of b and b′. The oxygen content of clay particles would filter out some higher order light reaching the detector decreasing b. However, a constant is subtracted from the I spectrum, implying more higher order light is present in this spectrum. This dip could also arise from oxygen 2nd order EXAFS oscillations but we are not certain. Despite our lack of physical understanding, the suggested method is effective and was used for our analysis of the naphthenic acid-illite spectra.

To demonstrate the effectiveness of the method, we show a comparison of the same spectrum processed using both methods. A constant of 20 was subtracted from the I spectrum used in Figure 4-5 and the new spectrum is shown in Figure 4-6. The dip at 285 eV is no longer present and the rest of the spectrum remained unchanged. We are not completely satisfied with this method, since a pre-edge peak is apparent at the same energy as the dip and because the physical understanding is lacking. However, this was the best method found and was used for our naphthenic acid-illite samples. The naphthenic acid-illite mixture was tested on two separate occasions at the beamline, and both events provided essentially the same spectra, providing confidence in this data.

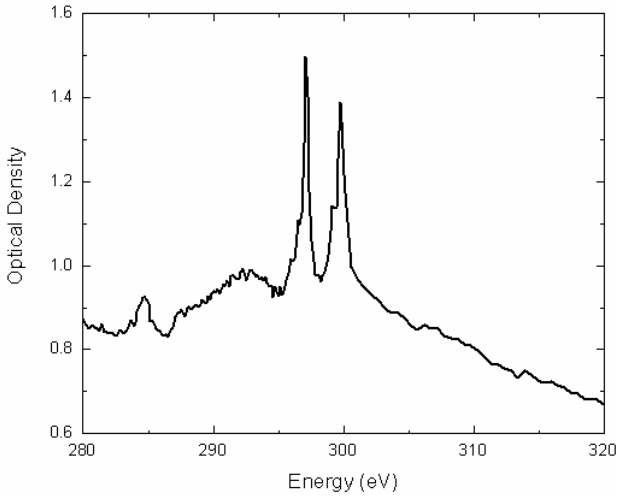

Figure 4-6. An example demonstrating the removal of the carbon "dip" at 285 eV from a C 1s NEXAFS spectrum of an organic-clay sample.

This section has demonstrated several difficulties encountered during data processing. Once these processing problems were addressed and techniques were created and tested to account for them, they were utilized where necessary for data processing. The results and discussion sections in this chapter as well as chapter 5, will indicate the types of normalization and corrections used in data processing.

4.2 Model Clays

Before studying the chemical interactions between clay surfaces with organic species, it was necessary to test our experimental methods on simpler systems where all components were well known. To study hydrocarbon-clay interactions, we must be certain that our original model clays are free from any pre-existing organic species, otherwise we cannot differentiate these organic species from our model species. The model clays were provided by our collaborators at NRCan; however, they originated from international clay banks in Japan and Georgia. To obtain data for our model clays, we used fast imaging to find good regions of small clay particles, followed by 5 μm x 5 μm image sequences to obtain C 1s NEXAFS spectra in conjunction with spatially resolved images.

4.2.1 Sample Preparation of Model Clays

Illite and kaolinite were used for model clays as they are present in the highest abundance in the oil sands. For a properly controlled study, it was important to compare clays in both their natural version (as received from clay banks) as well as a bleached version. The reason for using bleached clays was to ensure the clays were free from all extraneous carbon. This is important because we want to look at the surface interactions between hydrocarbons with clays. If the clays are not bleached to remove surface contaminants, they may contain organic components covering part or all of their surfaces. The signal from this contamination could be stronger than from model hydrocarbons, which would invalidate our experiments. For these studies, we acknowledge using bleached clays is not ideal as the bleaching procedures may change the surface chemistry of the clays. However, this is an essential starting point. This was first imperative to show

that X-ray spectromicroscopy experiments could be used to study hydrocarbon-clay surface chemistry.

Bleaching Procedures

To remove all organic contaminates from the model clays, two different bleaching procedures were used. The first bleaching process consisted of a peroxide bleaching technique which was used for the kaolinite clays in our studies. The protocol for this technique is as follows:

1. 25 mL of 30% H_2O_2 was added to 2.5 g of clay in a 250 mL beaker.
2. When the reaction subsided, the beaker was placed on a hotplate and a 5 mL aliquot of 30% H_2O_2 was added and stirred with a glass rod. (If the reaction was too violent, the beaker was placed in cold water)
3. H_2O_2 was added until the organic matter was largely destroyed.
4. Evaporation was permitted such that a concentration of H_2O_2 was approximately 20% in the beaker. After 2-4 hours of digestion, the organic matter removal was complete, and any remaining material was washed from the sides of the beaker with de-ionized water.
5. The beaker was made up to approximately 70 mL using de-ionized water and centrifuged at 15,000 rpm for 15 minutes.
6. The supernatant was discarded and the clay was quantitatively transferred into an evaporation dish and allowed to dry at 105ºC for 24 hours.

The second method used for bleaching, citrate-bicarbonate-dithionate (CBD), was found to be more effective and was used for the model illite. The protocol for CBD is:

1. 40 mL of 0.3 M sodium citrate solution and 5 mL of 1 M $NaHCO_3$ solution were added to 1 g of over dried clay in a 200 mL beaker.

2. The beaker was placed in a water bath and maintained at 75-80ºC. 1 g of sodium dithionate was added, and the mixture was stirred constantly for 1 minute, then occasionally every 5 minutes. (If a brown or red color remained, 1 g more of sodium dithionate was added while the mixture was being constantly stirred).

3. After 15-30 minutes of digestion, 1 M NaCl was washed and centrifuged.

4. The clay was washed with de-ionized water, and left to dry.

The experimental details of these procedures were provided by our collaborators at NRCan. All of the bleaching was also performed by workers at NRCan, and the final bleached products were provided to us for investigation.

Clay Casting Procedure

The clay samples were suspended in Millipore water and cast onto Si_3N_4 membranes using a 0.1 µl Eppendorf pipette. An Eppendorf pipette was used to avoid cross contamination from incomplete cleaning of reusable syringes. Very tiny droplets, less than 0.1 µl, are required to ensure that the entire membrane surface is not covered by solution so that an unexposed area is present for measuring the incident flux (example case "a" in Figure 4-1). A small droplet was created at the tip of an Eppendorf pipette and was lowered onto the membrane surface leaving behind a very small droplet of sample on the substrate. This method was the approach used for casting all of the samples onto their substrates.

Once the samples were prepared, they were mounted on a STXM sample holder and examined by the Visual Light Microscope (VLM) contained in the hutch at STXM 5.3.2. The stages of the VLM and STXM microscope have their indices correlated in order to locate areas of interest in the sample. This correlation facilitates an easier and faster means to locate desired regions of the sample when inside the STXM chamber.

4.2.2 Results of Model Clays

To access the validity of using these clays as models, we examined both the bleached and unbleached versions of the clays. We found that the original, unbleached clays contained various forms of carbon on their surfaces. An example of this carbon can be seen below in Figure 4-7. This figure represents a C 1s NEXAFS spectrum obtained from one of our unbleached kaolinite samples. A large amount of organic species present in the kaolinite. A small amount of unsaturation is apparent from the low energy peak at 285 eV, and the larger feature at 288.5 eV appears to be a type of carboxylate (eg. -COOH).[10]

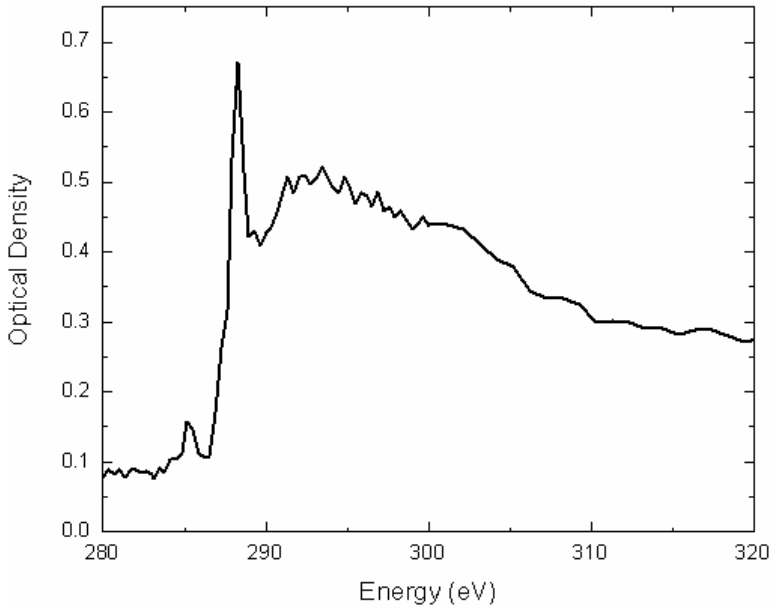

Figure 4-7. C 1s NEXAFS spectrum of clay particles from the Clay Society of Japan without purification.

It should also be noted that this sample was particularly undesirable, because by closer examination of the spectrum, the background is fairly flat and close to zero; indicating that we were examining only organic material and not clay. If clay particles were present, then one would expect the background to be tilted with a negative slope due to the absorption of the Al-Si-O layers of clays. A representative spectrum of 0.2 μm clay ($Al_2Si_4O_2$) is shown in Figure 4-8. Since we did not observe a strong background in our spectra, we were actually examining a thin organic film. When the kaolinite was cast onto the Si_3N_4 membrane and allowed to dry, an organic component dried separately, most likely originating from organics loosely bound to the clay particles.

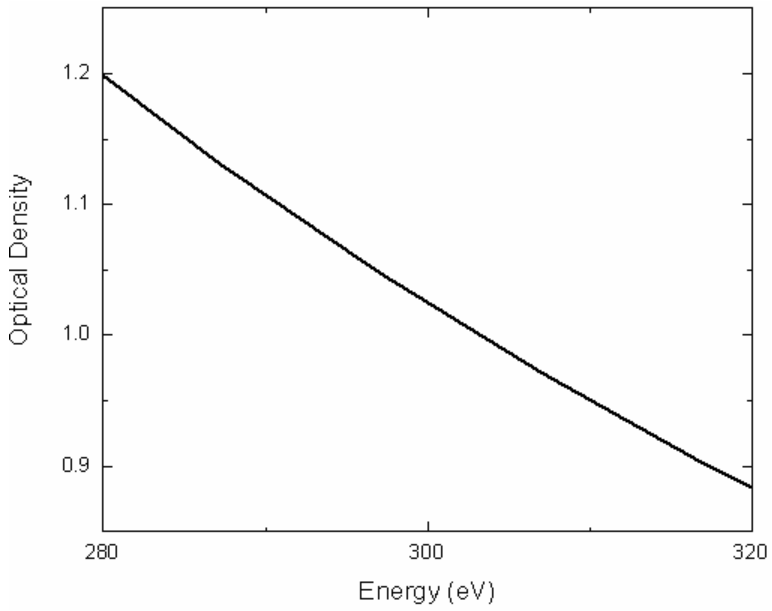

Figure 4-8. Simulation of the typical background absorption from clay particles in the carbon region.

To test our hypothesis regarding this sample preparation issue, we re-made the sample using a slightly different technique. Once the sample was cast onto the membrane, intense heat from a microscope lamp was used to speed up the drying process.

This process was observed using a light microscope, and a very evident spatial separation was seen as the sample dried. When examined using the STXM, we discovered the organic species dropped out of solution first (near where the drop was cast on the membrane), and the clay particles would deposit in a different region of the droplet. This type of separation allowed us to investigate the clay particles rather than organic species as there was a separation on the window. Figure 4-9 shows the C 1s NEXAFS spectrum we obtained from one of these kaolinite particles along with another kaolinite particle from a different sample. Although the new preparation method was useful for separating the organic species from the clays, the spectra indicate that both kaolinites contained large amounts of organic species and were therefore undesirable for use in our studies with model organics.

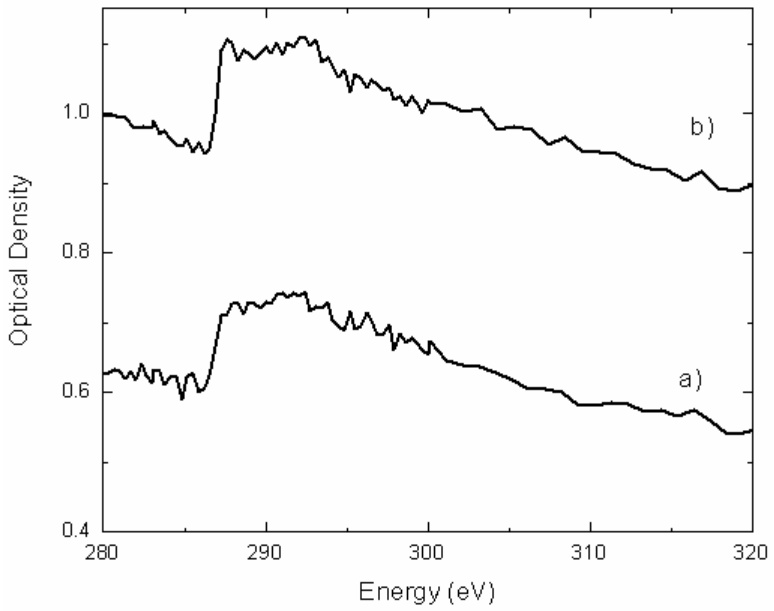

Figure 4-9. C 1s NEXAFS spectrum of unbleached kaolinites from a) Japan and b) Georgia clay banks.

After discovering that our library kaolinite clays contained significant amounts of carbon, in conjunction with our collaborators, we decided to investigate peroxide bleached versions of these clays. Exposing the clays to a peroxide bleaching procedure should remove the organic species associated with the clays. However, when the bleached kaolinites were first examined in the STXM, we found that they still contained organic contamination. Representative C 1s NEXAFS spectra of the bleached samples are displayed in Figure 4-10. There was a large variance between different regions within the same sample as can be seen by comparing spectrum "a" and "c" in Figure 4-10. These two spectra were obtained from two regions within the same bleached kaolinite sample. They are substantially different, as spectrum "a" appears to be well bleached, showing very little carbon, while spectrum "c" has a large amount of carbon and potassium contamination. This problem is attributed to incomplete bleaching procedure, leaving contamination behind in some of the clay particles. Clearly, these new samples were not sufficient for our model studies; thus our search for clean model clays needed to be revisited. After our failed attempts to obtain clean kaolinite clays, illite was bleached using CBD rather than peroxide.

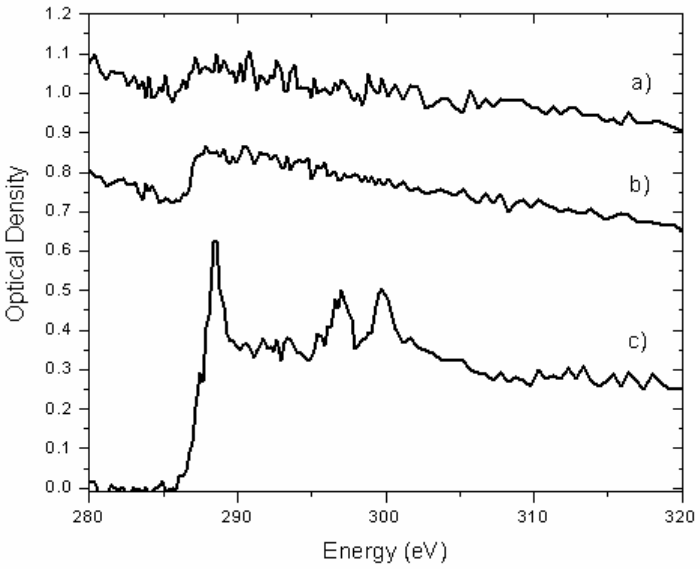

Figure 4-10. C 1s NEXAFS spectra of a) Bleached kaolinite (Georgia), b) Bleached kaolinite (Japan), and c) Bleached kaolinite (Georgia second region showing variation)

Exploring the newly bleached (CBD) illite sample in STXM 5.3.2 at the ALS represented our first C 1s NEXAFS spectra of clays fairly free from organic species. An example of a C 1s NEXAFS spectrum obtained from the bleached illite is shown in Figure 4-11. Several repeated stacks were obtained on this sample and they all produced similar spectra; clean clays with only a small "bump" present near the carbon edge. Due to the repeatability of the carbon free spectra, the bleached illite sample was used for our studies of model organic species mixed with clay particles.

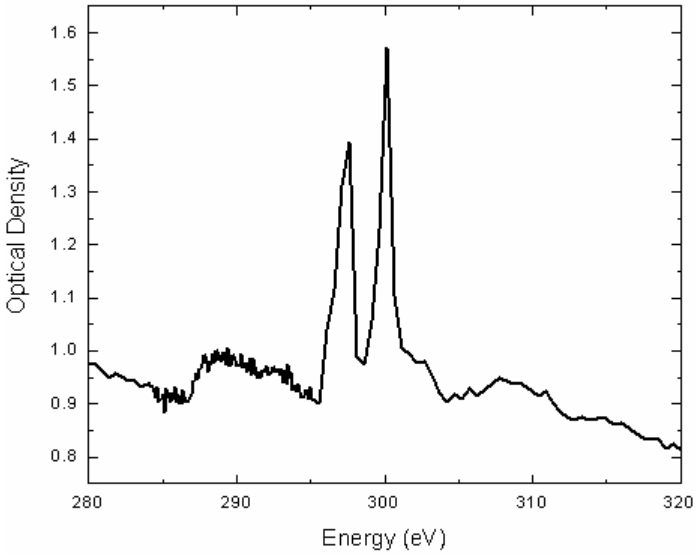

Figure 4-11. C 1s NEXAFS spectrum of CBD bleached illite.

4.2.3 Discussion and Summary of Model Clays

We observed a large amount of carbonaceous material associated with the clays obtained from the clay banks. Both kaolinites contained organic species which remained even after peroxide bleaching. In some cases, it appeared that different organic species were present after the clays underwent bleaching. This can be seen from the C 1s spectra shown for the Georgia clay before (Figure 4-9(b)) bleaching and after (Figure 4-10(c)) bleaching. Before bleaching, the kaolinite C 1s spectra had peaks at 287 eV and 291 eV, but after bleaching, there are 2 sharp peaks at 288 eV and 290 eV which were not present in the original kaolinite as well as two large potassium peaks at 297 eV and 300 eV and most likely arose as a contaminant from bleaching.

In other cases, similar organic species were found before and after bleaching. An example of this is shown in Figure 4-12. These spectra were extracted from the bleached and unbleached versions of kaolinite from Japan. Both of these spectra show the presence

of carbon at 285 eV (unsaturated carbon) and at 287 eV (aliphatic carbon) indicating the peroxide bleaching was extremely inefficient for these clays.

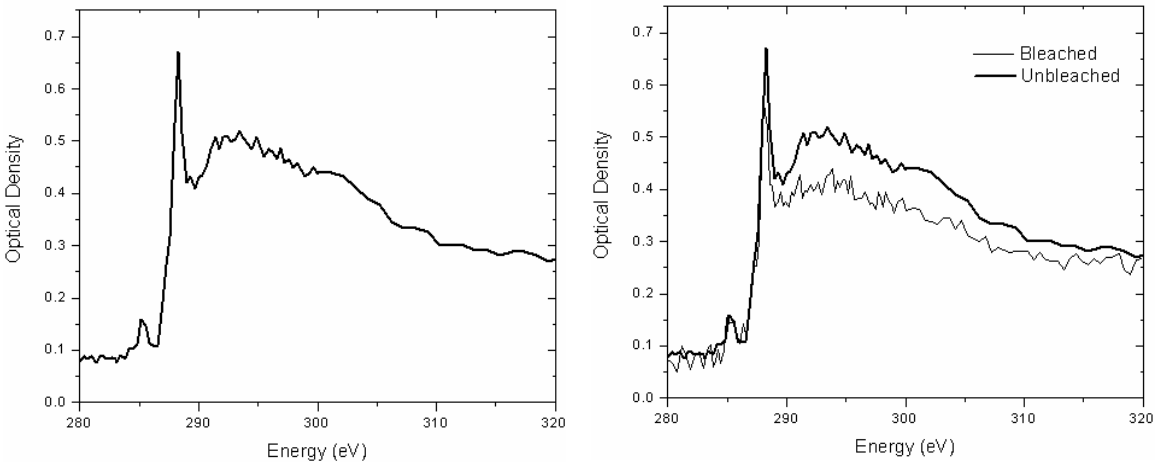

Figure 4-12. C 1s NEXAFS spectra of (a) Bleached kaolinite from Japan and (b) Overplot of bleached and unbleached kaolinite from Japan.

After examination of many image sequences, we hypothesize that we had regions in both the bleached and unbleached kaolinites where an organic film encapsulated our clay particles. Also, we were able to see that areas that appeared as clay particles without this organic encapsulation still contained carbonaceous material. Therefore both peroxide bleached kaolinites were not suitable for our studies.

4.3 Model Organics

To determine the association between model organics with bleached illite, it is imperative to have C 1s NEXAFS spectra of the pure organic species. Thin cast films of naphthenic acid and methylene blue were prepared. To obtain this data, we first used the STXM in imaging mode to identify regions where there was a thin molecular film, and then high resolution line scans were used to obtain the C 1s NEXAFS spectra. Line scans were used rather than image sequences because they are less time consuming, while they

still provide high resolution spectra. Furthermore, we were only interested in spectra, not morphological information.

4.3.1 Model Organics

Methylene blue and naphthenic acid were chosen as the two model organics to be associated with our bleached illite. The chemical structure of methylene blue is shown in Figure 4-13. Naphthenic acid is a complex mixture of many types of carboxylic acids; therefore it does not have one specific chemical structure; however, Figure 4-14 shows several carboxylic acids commonly found in the mixture. Naphthenic acids are common components found in oil sand tailings and they contain carbonyl functional groups which are not present in methylene blue. Therefore, they were used as the second type of organic species to be mixed with the model illite.

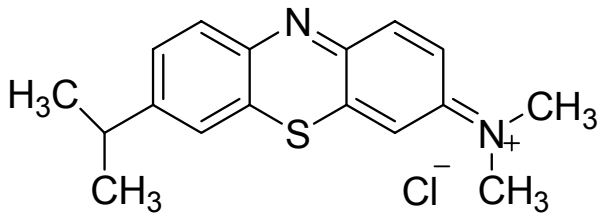

Figure 4-13. Chemical structure of methylene blue.

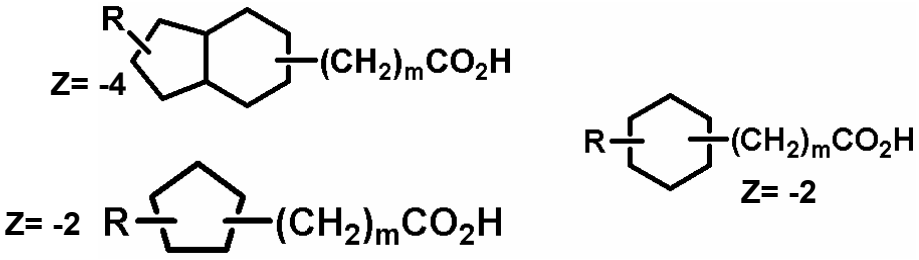

Figure 4-14. Chemical structure of some of the components of naphthenic acid.(R represents an alky group, m represents the alkyl chain length and z is the H deficiency due to ring formation)[64]

4.3.2 Sample Preparation of Organic Species

The two model organics were prepared identically. The sample preparation for the organic species was very similar to the previously described model clay preparation. The samples were fairly low in concentration ~ (0.001 M) and a 0.1 μl Eppendorf pipette was used to cast a small droplet of each organic species onto a blank Si_3N_4 membrane. The solutions were allowed to dry and were then mounted to STXM sample holders.

4.3.3 Results and Discussion of Pure Organics

To obtain properly normalized spectra for the two pure organic species, external normalization, using a blank Si_3N_4 membrane as shown earlier, was utilized. High resolution C 1s NEXAFS spectra were obtained for these samples using line scan acquisition in the STXM.

The C 1s NEXAFS spectrum of naphthenic acid, obtained using external normalization, was shown earlier in Figure 4-3(b). Two main features can be seen in this spectrum, a small peak at 285 eV that can be attributed to a weak aromatic component, C 1s (C-H) $\rightarrow \pi^*_{(c=c)}$, and an intense peak at 288.5 eV from C 1s (C=O) $\rightarrow \pi^*_{(c=o)}$, due to the carbonyl component (carboxylate) in the naphthenic acid. As seen in Figure 4-4, the background on the Si_3N_4 membrane near the naphthenic acid shows a large absorption at 285 eV. This indicates that the membrane has a thin film of an aromatic species covering it, thereby invalidating the use of a nearby substrate region for normalization. The spectrum obtained from the membrane region near the thicker organic thin film is completely different from the COOH contribution; leading us to believe that we could be seeing a separation of the organic species contained in naphthenic acid. More specifically, a thin layer of aromatic rich species could be depositing on the Si_3N_4

membrane first as the film dries on the membrane, perhaps indicating a strong association with the surface of the membrane. This is evidence for differential segregation of different naphthenic acid components on the Si_3N_4 membrane.

The C 1s NEXAFS spectrum of methylene blue is shown below in Figure 4-15. The spectrum exhibits four well resolved peaks at 283.9 eV, 285.3 eV, 286.5 eV and 287.3 eV, and two broader features at 289.5 eV and 290.1 eV. The assignments of these features are documented below in Table 4-1. In contrast to the external normalization used for naphthenic acid, a region close to the methylene blue was suitable for normalization. This normalization was valid because there was no evidence of any organic species covering the surface of the Si_3N_4 membrane next to the organic deposit.

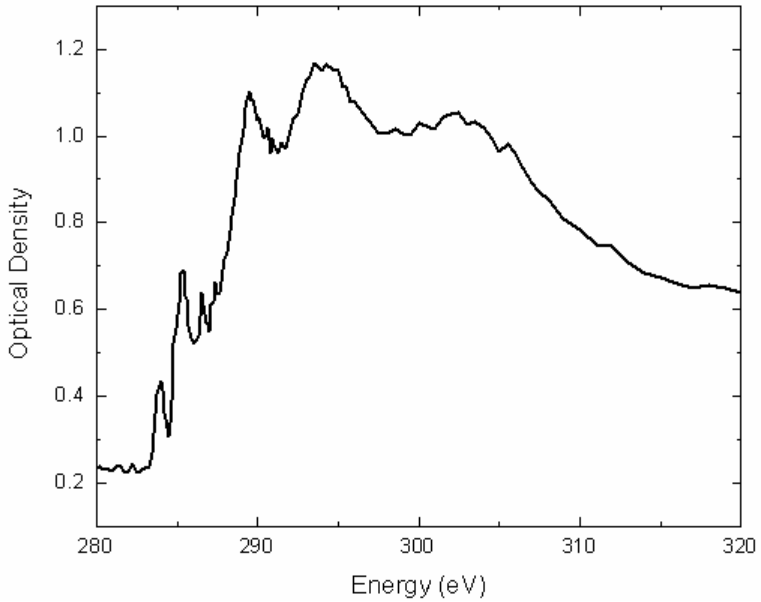

Figure 4-15. C 1s NEXAFS spectrum of methylene blue.

Peak Energy (eV)	Assigned Transition
283.9	C 1s (C-H) → $1\pi^*_{(C=C)}$
285.3	C 1s (C-H) → $1\pi^*_{(C=C)}$
286.5	C 1s (C-R) → $1\pi^*_{(C=C)}$ (functionalized aromatics)
287.3	C 1s (C-R) → $1\pi^*_{(C=C)}$ (functionalized aromatics)
289.5	C 1s → $\sigma^*_{(C-H)}$
290.1	C 1s → $\sigma^*_{(C=C)}$

Table 4-1. Assignment of the absorption peaks at the C 1s NEXAFS spectrum for methylene blue.

The differences between the behavior of naphthenic acid and methylene blue when cast on Si_3N_4 membrane surfaces could be because naphthenic acid is a mixture of many substances whereas methylene blue (99% Alfa Aesar high purity) contains one major component. These different behaviors play an important role in the data processing, as the normalization for the mixture of the organics with the bleached illite must be performed with caution.

4.4 Hydrocarbon-Clay Mixtures

The two model systems investigated were mixtures of illite with naphthenic acid and illite with methylene blue. All of the spectra obtained for these two systems were collecting using image sequences. Due to the previously mentioned normalization issues, external normalization (case "c" in Figure 4-1), using either a blank Si_3N_4 membrane or multi-region image sequences, was used for data processing of the naphthenic acid with illite sample. Multi-region image sequences involve setting the STXM to acquire an image sequence in two slightly displaced regions of the sample, such that data is obtained in one region for one energy (I), then the sample is moved to the second (clean) region, untouched by solution drying, and the Io data is obtained.

4.4.1 Sample Preparation of Hydrocarbon-Clay Mixtures

To prepare the model hydrocarbon-clay mixtures, a preparation method, similar to the model clays and model organics was used. First the clays were mixed into a dilute solution of the different organics, naphthenic acid and methylene blue. These mixtures were left overnight to ensure enough time for adsorption. It is important to note that the exact ratio of clay in the mixture of organic species was unknown. This Masters project was concerned with proving that the STXM could be used to study such systems, thus simple model systems were examined. However, in the future, it would be very interesting to have more comprehensive sample preparation to explore how factors such as solution pH, and solid to organic ratio affect the outcome of the experiments.

An Eppendorf pipette was used to cast droplets (1 μl) of the solutions onto clean Si_3N_4 membrane (75 nm from Norcada Inc.). When small clay particles could be seen settling to the membrane, a small stream of air was blown across the membrane to remove the liquid drop from the surface of the clays on the membrane. This step was very important for two reasons; first because we want to investigate organics attached to clay surfaces and not organics that dried on top of the clays, and secondly to avoid having the organic liquid drying on the membrane. This makes obtaining a blank area of Si_3N_4 near the deposited clay to use as an Io for normalization possible.

4.4.2 Results and Discussion of Hydrocarbon-Clay Mixtures

The C 1s NEXAFS spectrum for naphthenic acid mixed with illite is presented in Figure 4-16. To obtain accurately processed spectra for this mixture, we utilize external normalization with a small 1 μm x 1 μm stack on a blank Si_3N_4 membrane as the Io spectrum. A small stack was done for the normalization to ensure all of the parameters,

including dwell time and STXM acquisition mode, were the same for both the I and Io spectra. The use of external normalization was necessary for this sample, because, as shown below in Figure 4-17, the background of the membrane near the naphthenic acid-illite mixture contains a thin film of organic species. The C 1s NEXAFS spectrum obtained in this background is almost identical to the one shown earlier in Figure 4-4, which was background near pure naphthenic acid. The fact that the two background spectra are almost identical is indicative that our presumption that there is a weak aromatic component in naphthenic acid which associates well with the Si_3N_4 membrane surface. The spectra shown may not be 100% representative of the chemistry, due to normalization issues; however, they are evident that there is definitely some organic species bound to the substrate.

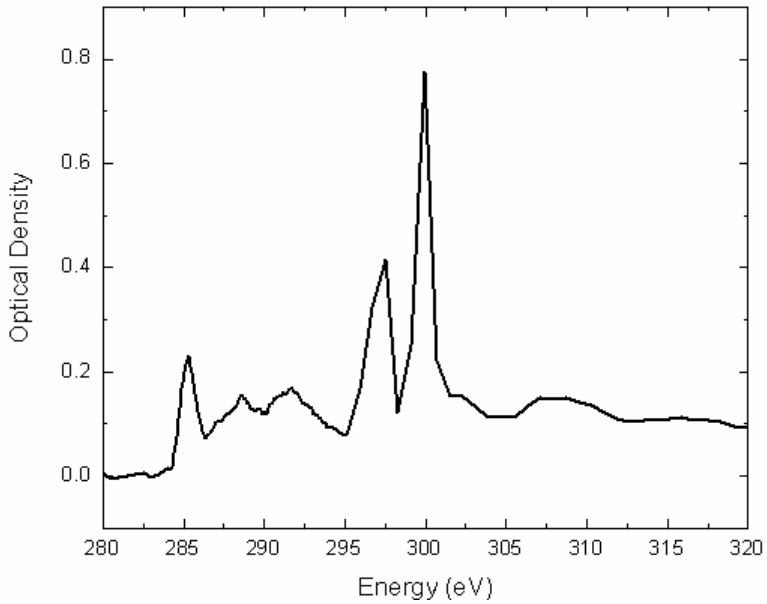

Figure 4-16. C 1s NEXAFS spectrum of bleached illite mixed with naphthenic acid.

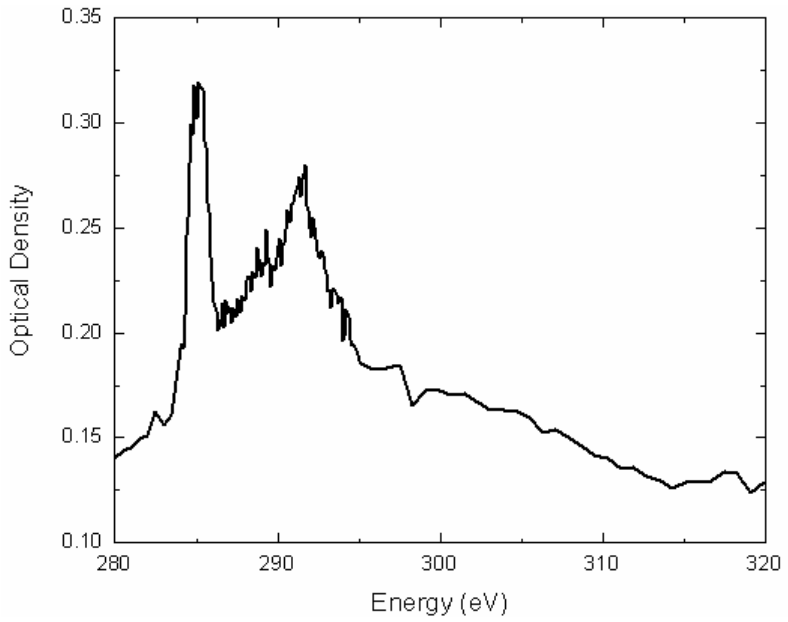

Figure 4-17. C 1s NEXAFS spectrum of the background Si_3N_4 membrane near the illite-naphthenic acid mixture.

In the C 1s NEXAFS spectrum of naphthenic acid associated with illite shown in Figure 4-16, we see four major features at 285.2 eV, 291.5 eV, 297.3 eV and 299.6 eV. The spectral assignments for these peaks are provided in Table 4-2. The two last peaks are attributed to the potassium 2p edges in illite, which ensures us that we are investigating the illite and not an organic thin film without clay. At 288.5 eV, a weak feature can be seen which arises due to C 1s (C=O) $\rightarrow \pi^*_{(C=O)}$ transitions from the carbonyl functionality of the carboxylic acids.[10] Several different image sequences were acquired on this system; all produced similar spectra. To show the reproducibility, three representative spectra are shown in Figure 4-18 from naphthenic acid mixed with illite collected by different image sequences on varying occasions. The small feature at 288.5 eV provided the only variation because in some spectra it was not as strong as in others. All of the repetitions showed that the background near the clays contained organic species therefore validating the use of external normalization for this sample.

Peak Energy (eV)	Assigned Transition
285.2	C 1s (C-H) → $1\pi^*_{(C=C)}$ (aromatic)
288.5	C 1s (C=O) → $\pi^*_{(C=O)}$
291.5	C 1s (C-C) → $\sigma^*_{(C-C)}$
297.3	K $2p_{3/2}$
299.6	K $2p_{1/2}$

Table 4-2. Assignment of the absorption peaks in the C 1s spectrum of naphthenic acid.

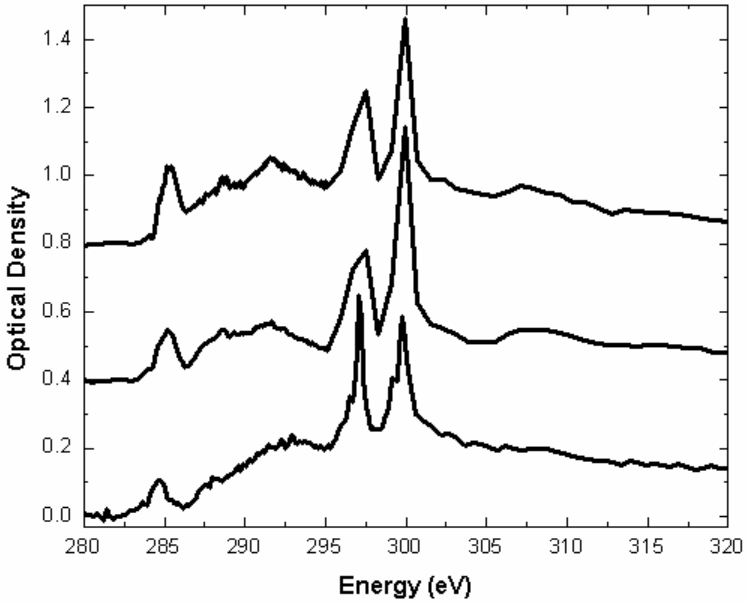

Figure 4-18. C 1s NEXAFS spectra of naphthenic acid mixed with illite indicating good spectral reproducibility (spectra offset for clarity).

In comparing the spectrum of pure naphthenic acid and naphthenic acid mixed with illite, large differences are observed. An over-plot of the two spectra is shown below in Figure 4-19. The spectrum of naphthenic acid alone shows a very strong (as expected) peak at 288.5 eV from the carbonyl groups; however, this peak is barely apparent (small feature) in the spectrum of the naphthenic acid mixed with illite. This observation can be attributed to a separation of many different components in naphthenic acid. For example, a component with a different COOH/aromatic ratio may be segregating to the clay surfaces.

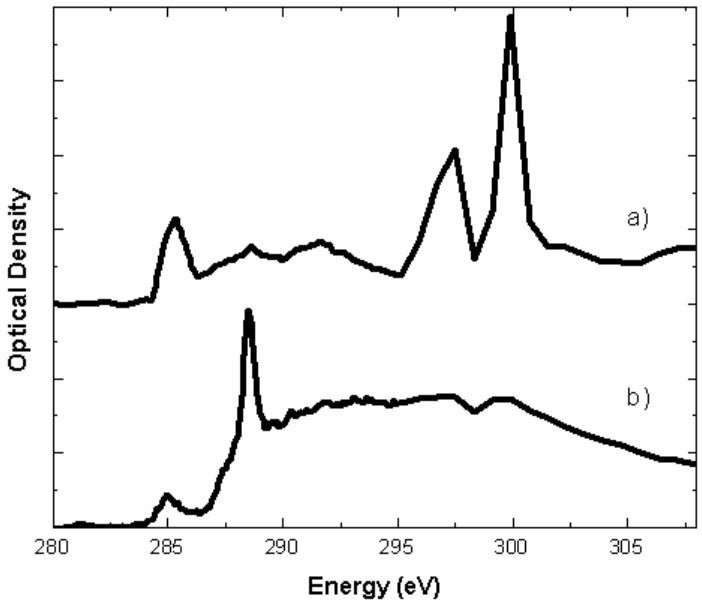

Figure 4-19. Over-plot of C 1s NEXAFS spectra of a) Naphthenic acid with illite and b) pure naphthenic acid (offset for clarity).

The C 1s NEXAFS spectrum for the mixture of methylene blue with illite is presented in Figure 4-20. Three separately acquired spectra are shown to demonstrate the reproducibility of the data. An important note on this sample was that external normalization was not necessary for the processing and analysis, although multi-region stacks were taken as a precaution. The areas of Si_3N_4 membrane near the mixture of illite and methylene blue appeared to be free of organic film, unlike what was observed for the mixture of illite with naphthenic acid. This result indicates that methylene blue only absorbs on the clay surfaces and not on the Si_3N_4 membrane. Figure 4-21 shows a C 1s spectrum using the background near the mixture of methylene blue with illite as the transmitted flux (I) and a blank Si_3N_4 membrane as the incident flux (Io). The noisy line, centered near the origin corroborates our observation that there is no thin film of organic contaminants in the regions neighboring methylene blue and the methylene blue with illite samples.

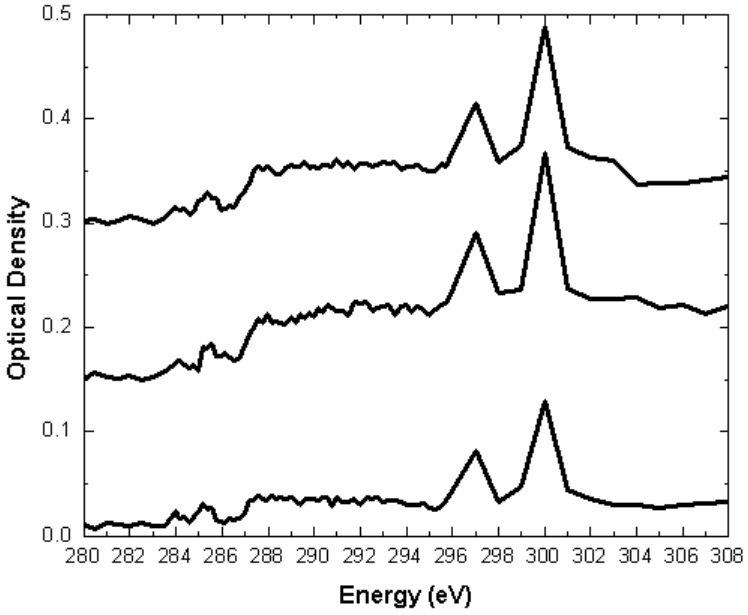

Figure 4-20. C 1s NEXAFS spectra of methylene blue mixed with illite showing spectral reproducibility (offset for clarity).

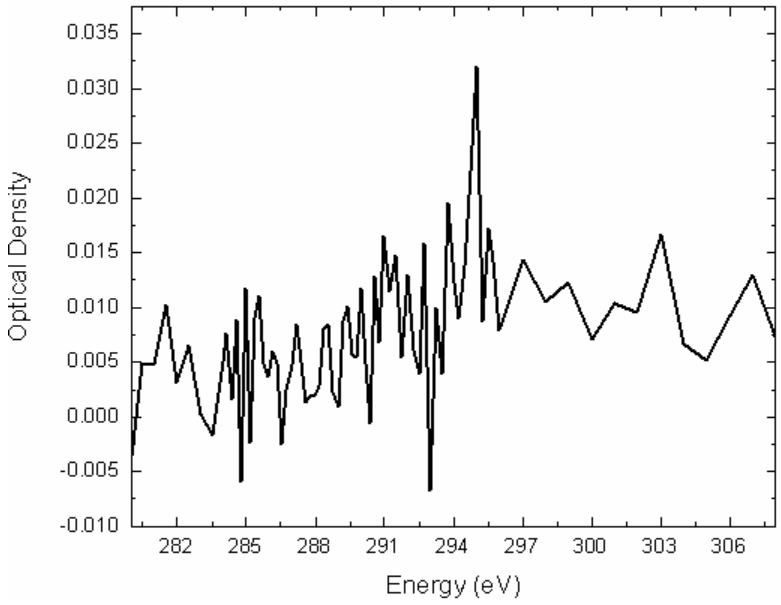

Figure 4-21. C 1s NEXAFS spectrum of the background near the sample of methylene blue mixed with illite.

The C 1s NEXAFS spectrum of the methylene blue with illite exhibited features at similar energies as seen in the spectrum of pure methylene blue. An over-plot of the two

spectra is shown below in Figure 4-22. A peak was seen at 283.9 eV attributed to C 1s (C-H) $\rightarrow 1\pi^*_{(C=C)}$, 285.3 eV from C 1s (C-H) $\rightarrow 1\pi^*_{(C=C)}$ transitions, 286.5 eV and 287.5 eV from C 1s (C-R) $\rightarrow 1\pi^*_{(C=C)}$ (functionalized aromatics) transitions. The two strong absorptions seen at 297 eV and 300 eV represent the potassium $L_{2,3}$ edges from the potassium present in the illite interlayer. There is also a smaller feature around 288 eV which is not present in the spectrum of pure methylene blue. Our best assignment of this feature is a small amount of photodeposition. The broad features seen at 289 eV and above in the spectrum of pure methylene blue are not present, or at least not well defined in the spectrum of the mixture. This is most likely due to the large potassium peaks from the illite dominating this higher energy region. Overall, the peaks present in our mixture compare very well with the peaks observed in our pure methylene blue spectrum, providing us with confidence that methylene blue is attached to the surface of bleached illite. Also, the fact that we have a clean background near the illite-clay species gives us confidence that there is preferential binding for the methylene blue with the illite surface rather than with the Si_3N_4 membrane. Because methylene blue highlights ionic interactions with the illite surface, we suspect that clay surfaces associate preferentially with ionic (cationic) substances. This agrees well with the ability of clays to undergo cationic exchange discussed previously in literature.[50,65] By comparison, the polar interactions that would be induced with naphthenic acid, did not exhibit very good association with illite which could be lack of selectivity to illite, or because of adsorption to the Si_3N_4 substrate. Therefore, it appears that for our model study, ionic interactions are more selective to the illite surface than polar interactions.

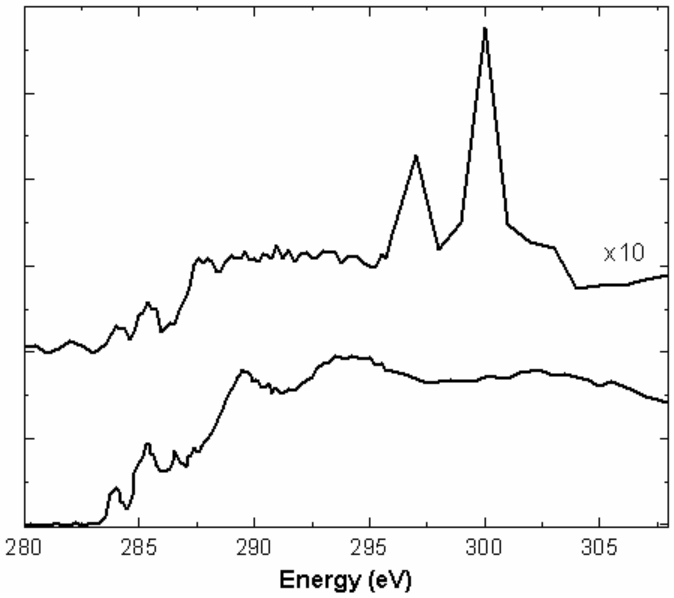

Figure 4-22. Over-plot of C 1s NEXAFS spectra of a) Methylene blue with illite and b) Pure methylene blue (offset for clarity).

To further enhance the confidence in our MB-illite data, we compared our newly obtained data with results from a study by *Hähner et al.* (1996).[50] They investigated both the orientation and electronic structure of methylene blue on mica using NEXAFS spectroscopy. Their measurements were detected using partial electron yield detection with an energy resolution of only 0.5 eV at the C 1s edge.[50] They acquired C 1s NEXAFS spectra of methylene blue bound to mica which appeared similar to our spectra of methylene blue bound to illite providing us with assurance that the data we obtained was accurate.

4.5 Summary

Our model system studies provided us with some invaluable information regarding sample preparation and processing issues. The search for our model clay proved that some of the bleaching methods being used to remove organic contaminants from clay

surfaces are not completely effective. Also, it showed that clays from clay banks contain inherent organic contaminants.

During the course of model studies, we encountered many problems in sample preparation. We were able to identify and develop methods to overcome these problems. These include:

1.) A troublesome problem involved spectral artifacts from sample drying. Originally, we solution cast samples and allowed them to dry but we observed precipitation of organics on the clays. Then, we rinsed the samples in Millipore water and used heat from a microscope lamp to speed up the drying. This method appeared to prevent organics from drying on the clays, but was only useful for substances where there was a low concentration of organic species present.

2.) When examining the organic species mixed with clays, we had to develop a new preparation method. The previously used preparation did not work for these samples because we found that the substrate was coated with a layer of precipitated organic components which we were unable to remove by rinsing with Millipore water. Therefore, we decided to use a light pressure of air to blow off the excess solution from the membrane's surface so that the solution would not have a chance to dry on the sample surface nor on the Si_3N_4 membrane.

Encountering these various preparation problems required us to develop sample preparation procedures that could be used to eliminate the difficulties. We successfully developed procedures that worked adequately for all of our samples.

Once our model clay was obtained and we were able to overcome sample preparation issues we were able to study clean clay surfaces without drying artifacts and organic film encapsulation impeding our studies. In our study of hydrocarbon-clay interactions, we were able to show that there was a fairly strong association between the methylene blue and illite particles, perhaps due to favorable ionic interactions. Our study of naphthenic acid mixed with illite showed weak interactions between a subset of hydrocarbons and illite particles. The naphthenic acid appeared to exhibit several different components, some of which appeared to have an affinity towards the substrate rather than, or just as much as, the clay's surface. Our methylene blue mixed with illite data agreed well with previous literature data providing us with confidence in our methods. The results from these studies showed that although we used bleached clays which may have altered the surface of the illite particles, we were still able to achieve results which would be expected based on physical arguments.

CHAPTER 5

RESULTS AND DISCUSSION OF PROCESS SAMPLES

The overall goal for this project was to develop characterization techniques to examine hydrocarbon-clay interactions in oil sand samples. Chapter 4 discussed experiments examining organic-clay interactions in controlled model systems, where both the clay particles and organic species were known. We were able to identify and assess the associations between organics and clays when they were mixed together.

However, we would like to apply our STXM experiments to process samples from the oil sands. In this chapter, we discuss our studies on a set of four bitumen froths samples. Section 5.1 provides a brief introduction to the samples, including our rationale for studying them. In § 5.2, all of the experimental details, including STXM operating conditions, sample preparation and data processing are discussed. The results and discussion of the samples are presented in § 5.3, and a summary of the findings is provided in § 5.4.

5.1 Process Samples

During bitumen extraction in oil sands processing, separation of the oil/sand mixture occurs into three regions, a bottom layer of large solids, a middle layer (clay-middlings) containing water and small fine clay particles, and a top layer composed of the bitumen froth. Our experiments investigate samples from the top layer of bitumen froth. The froth samples were obtained from our collaborators at NRCan, and their preparation will be described in § 5.2.

5.1.1 Rationale

Two bitumen froths were from Suncor Inc., a primary bitumen froth and a secondary bitumen froth, and two other froths originated from Petrocan. At the beginning of this study, we were interested to see if we could locate differences between organic species contained in the primary and secondary froths. As well, the amount of unsaturated carbon contained in the different froths could be investigated to make a correlation with earlier findings by our collaborators. Previously, they performed studies using confocal laser scanning microscopy and discovered different bitumen froth morphologies present due to the quantity of degraded bitumen present. They concluded that the diverse morphologies were linked to differences in bitumen chemistry in conjunction with distinctly different fluorescence behavior. Their investigations provided microscopic characterization of the bitumen components; however, they were not chemically sensitive to the different bitumen species. Therefore, our goal was to examine the froth samples to find chemical differences in the carbon spectra and make correlation between our chemical findings and their morphological/fluorescence changes.

5.2 Experimental Issues

All experiments were performed on STXM 5.3.2 at the ALS, in Berkeley California. The STXM was run using the liquid nitrogen cold trap (discussed in chapter 3), along with the nitrogen gas filter (pressure between 400 – 500 mTorr), to suppress higher order light (§ 2.4) and the STXM chamber was backfilled with helium.

5.2.1 Bitumen Froth Sample Preparation

All four froth samples were examined in the STXM by first using imaging to find uniform regions of the sample and then using line scans to collect the spectroscopic NEXAFS data rather than image sequences. Line scans were used for the froth samples because we were interested in assessing repeatability throughout many different regions of these samples. This was more easily done using line scans because they are much less time consuming than image sequences.

The four bitumen froth samples were all prepared in exactly the same manner. The substrates used for these samples were all 75 nm thick Si_3N_4 membranes from Norcada Ltd. A small amount of the black, crude froth was placed in a clean test tube, and dissolved in high purity toluene (optima), creating brownish/black solutions. Approximately 2 mL of this solution was removed and further diluted with optima toluene. Tiny droplets of the new diluted solution were cast onto Si_3N_4 membranes using very small droplets from the tip of an Eppendorf pipette. Clean Millipore water was used to rinse away the excess liquid from the membrane and heat from a microscope lamp was used to speed up the drying of the samples. The prepared membranes were attached to the STXM sample holder using either two sided tape or in a few cases, melted candle wax.

5.2.3 Data Processing

The froth data was processed in a manner which allowed for direct comparison between the various froth samples. This required quantization and careful normalization which is described below.

Normalization and Processing of the Bitumen Froths

For the model systems, normalization, using an Io spectrum from areas very close to the sample region, created spectral artifacts and inconsistencies in the C 1s NEXAFS spectra. This problem was attributed to a thin organic film covering most of the Si_3N_4 window, which was likely of similar thickness to the organics present on the clays' surface. Fortunately, this situation was not a problem for the bitumen froths because the carbon in the froths was extremely thick; therefore, a very thin layer of carbon on the membrane's surface would not affect the spectra after normalization. Thus, all of the froth data was normalized using a blank area of Si_3N_4 membrane close to the sample of froth, rather than a separate external source. Using this form of normalization, the I and Io spectra were obtained simultaneously, thereby eliminating the possibility of encountering intensity offsets in the I and Io spectra, which can distort and disrupt the correct NEXAFS spectra.

Our interests in studying the various froths transformed from looking at distinct differences between the froth samples, into a comparison of the amount of unsaturated carbon present in each of the froths. In C 1s NEXAFS spectra, unsaturated carbon, C 1s (C-H) $\rightarrow \pi^*_{(c=c)}$, exhibits absorption peaks at approximately 285 eV. In order to process our data in a manner that would allow proper comparison of the quantity of unsaturated carbon present in each froth, each C 1s NEXAFS spectra were consistently normalized to

a common carbon atomic cross section. The atomic cross section that was used for the normalization of these froths was a pure carbon atomic cross section, with a density of 1g/cm^3 and a thickness of 0.04 μm. This was used consistently throughout all of the data processing of froth samples and will be reported in the results and discussion section below.

5.3 Results and Discussion

This section focuses on the analysis of the four bitumen froth samples. After careful normalization and quantization the findings were compared with previous data from NRCan.

5.3.1 Analysis and Discussion of Bitumen Froths

All four of the bitumen froths appeared fairly similar, dark brown sticky tar-like materials, some of which were slightly less viscous than others. The primary and secondary froths were provided from Suncor, and the bitumen froths #1 and #9 were from Petrocan. No extra processing was performed on the samples.

Our goal was to quantitatively measure the relative strength of the C 1s → π* transition in the NEXAFS spectra of the four froths, to provide a quantitative measurement of the relative concentration of aromatic groups present in the froths. To achieve this, a set of consistent, high quality spectra for each of the froths was required. Obtaining spectra with both long pre and post edge regions was desirable to support the accuracy of the normalization procedures. To build statistical confidence in our measurements, several repetitions of each froth sample on separate occasions were acquired.

Normalized, C 1s NEXAFS spectra of the four bitumen froths are shown in Figure 5-1. Several repetitions of each sample were obtained; therefore the spectra shown are representative examples of the different froths. All four froths exhibited similar C 1s NEXAFS spectra, with main features occurring at 285 eV from C 1s $\rightarrow \pi^*_{(C=C)}$ transitions (unsaturated carbon), 287.5 eV from C 1s $\rightarrow \sigma^*_{(C-H)}$ transitions (aliphatic carbon) and a broader feature centered around 293 eV from C 1s $\rightarrow \sigma^*_{(C-C)}$ transitions. For all froth samples, there was little evidence of potassium. Although the absence of potassium does not imply that the samples are free of clay particles, the lack of potassium in combination with much lower backgrounds, indicates a vast reduction in the amount of clay particulates present in these four froths.

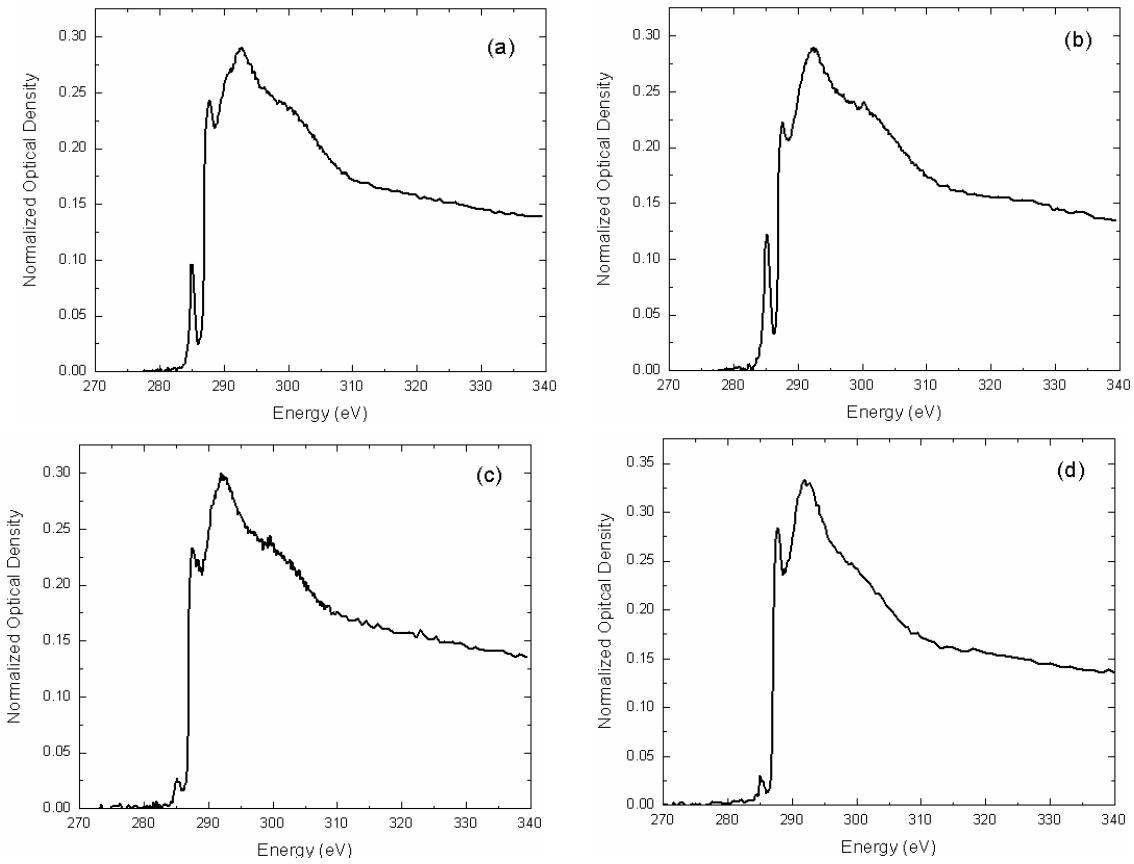

Figure 5-1. Normalized C 1s NEXAFS spectra of (a) Petrocan froth #1, (b) Petrocan froth #2, (c) Primary froth and (d) Secondary froth.

To achieve a quantitative comparison of the unsaturated carbon in the different froths using NEXAFS spectroscopy, froth spectra were carefully background subtracted and normalized to a common carbon atomic cross section. An overlay showing one spectrum from each froth sample as well as the cross section used for normalization is shown in Figure 5-2. To evaluate the amount of unsaturated carbon present, the area under the peak from 284 eV to 286 eV was calculated. This area was calculated for the unsaturated carbon peak in each sample for all trials, and the average with standard deviation and percentage error is reported. Spectroscopic sum rules indicate that the total area calculated under a background subtracted C 1s NEXAFS spectrum, integrated from the

far pre-edge region to infinity, normalized to an atomic cross section, is independent of chemistry. Therefore, the total area under the curve from the pre-edge to the far post-edge was evaluated and used as a measure to indicate error in the normalization. The outcomes of this study, including normalization consistency tests reported by average with standard deviation and percent error as well as unsaturated carbon data is presented in Table 5-1.

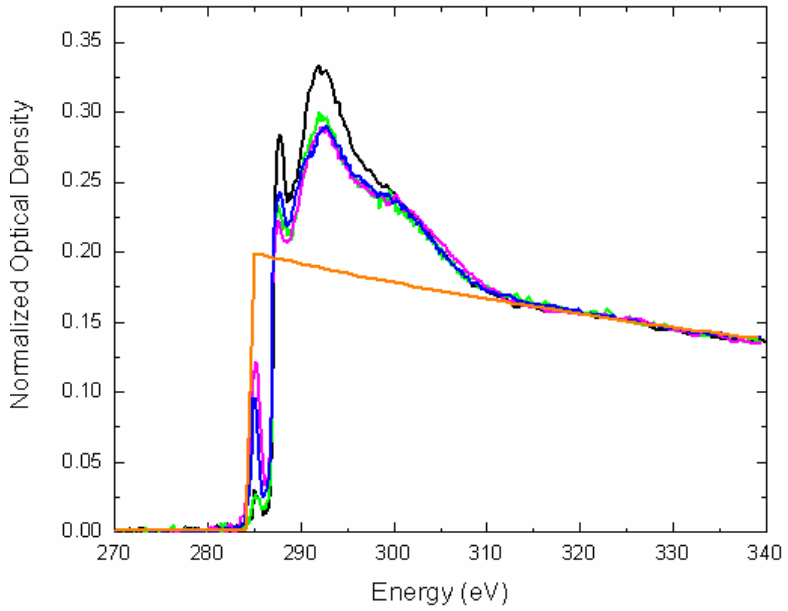

Figure 5-2. Overlay plot of normalized C 1s NEXAFS spectra of the primary froth (green), secondary froth (black), Petrocan #1 froth (blue) and Petrocan #9 froth (pink). The orange trace indicates the carbon atomic cross section used for normalization.

Sample	Average π area (std dev; % error)	Number of Spectra	Area under spectra (std dev; % error)
Petrocan #1	0.08 (±0.02; 20%)	4	10.1 (±0.4; 4.3%)
Petrocan #9	0.1 (±0.02; 18%)	3	9.8 (±0.2; 2.3%)
Primary	0.03 (±0.01; 33%)	3	10.0 (±0.1; 1.4%)
Secondary	0.03 (±0.01; 41%)	4	10.1 (±0.3; 3.2%)

Table 5-1. Peak areas of the unsaturated carbon peak with standard deviation and areas indicating normalization consistency.

By examining data reported in Table 5-1, the area under the π* peak in the two Petrocan froths is significantly greater than that in both the primary and secondary froths. This indicates that the Petrocan froths have a greater amount of unsaturated carbon than the two other froths. There is also a statistically significant difference in the amount of unsaturated carbon present in Petrocan #1 froth compared to the Petrocan #9 froth. In contrast, the area under the π* peak of the primary and secondary froths is identical within the statistics of these experiments.

The area under the entire spectrum that was reported represents an estimate of the quality of the normalization process. A larger variation in the area under the normalized spectrum reflects a greater non-statistical error in our normalization. The variation in the total area is low for all of the froth samples, and is significantly lower than the variation in the area of the π* peaks. This implies the froth samples may not have a homogeneous distribution of aromatic content, as the repeated spectra of the same samples exhibit slightly different π* peak areas. The small variation in the total peak areas indicates that the normalization method was reasonably effective and consistent.

Although some of our findings, particularly the comparison between the unsaturated carbon in the primary and secondary froths was not well determined, it is still desirable to compare our findings with data obtained by our collaborators. Using confocal laser scanning microscopy, they were able to develop semi-quantitative methods to assess the amount of degraded bitumen present in the different froths. The changes to the bitumen component were attributed to changes in bitumen chemistry which are believed to cause processing problems.[3] They quantified the amount of degraded bitumen present in the froths. Low fluorescence is associated with larger amount of inorganic particles and

degraded bitumen, and in our case, a decrease in the area under the π* peak. NRCan found that Petrocan #1 showed 100% degraded bitumen with large structures (250-300 μm) and Petrocan #9 showed only 5% degraded bitumen with smaller structures (mostly less than 100 μm). Our findings correspond well with their results. Our findings indicated the largest unsaturated carbon was in Petrocan #9, followed by Petrocan #1. However, their findings for the primary and secondary froths did not fit the data obtained using our quantitative NEXAFS, indicating that perhaps there is more variation in the samples then expected.

5.4 Summary

Investigations of the bitumen froths indicated that all four froths exhibited very similar spectra, three main carbon features. However, our major focus remained on the quantity of unsaturated carbon present in each of the froths. Within the statistical limits of our experiments, we were able to determine that the two Petrocan froths contain significantly more unsaturated carbon than both the primary and secondary froths from Suncor. However, no differences were observed between the amount of unsaturation contained in the primary and secondary froths. When comparing our quantitative NEXAFS analysis with NRCan's previous findings, the two Petrocan froths showed that the more unsaturated carbon present in our quantitative study corresponded to froths previously characterized by having less degraded bitumen thus more fluorescence. However, the primary and secondary froths did not fit into this correlation indicating more sample variation then expected for these samples.

CHAPTER 6

CONCLUDING REMARKS

6.1 Conclusions

The hydrocarbon-clay interactions of both model and process samples have been studied using X-ray spectromicroscopy. To accurately study these systems using STXM microscopy, the development of an anticontaminator was necessary to eliminate photodeposition of carbonaceous material on the sample. The anticontaminator was tested and proved to be effective and essential for our studies. A major portion of the work for this thesis was testing and developing various sample preparation methods to obtain samples free of contaminants, and drying artifacts, as well as providing proper thickness for transmission measurements.

The interactions between clay particulates and organics in the samples were directly probed using C 1s NEXAFS spectroscopy. The C 1s NEXAFS spectroscopy of our model clays demonstrated that the process used for bleaching clay particles to remove organic contaminants, in particular using peroxide, was not effective. A modified technique was then used instead, and a CBD bleached illite provided fairly carbon free clay particles. The study of the interaction of naphthenic acid with illite demonstrated that polar interactions between these substances were weak. We observed three

significantly different carbon spectra for pure naphthenic acid, naphthenic acid mixed with illite and naphthenic acid on the substrate. These findings lead us to believe that different components in naphthenic acid were separating. Some of which preferentially associated with the Si_3N_4 substrate while other associated to the illite clay surfaces.

Conversely, examination of methylene blue mixed with illite showed no indication of methylene blue bound to the Si_3N_4 substrate surface, indicating preferential binding of methylene blue to the clays' surface. The C 1s NEXAFS spectrum of pure methylene blue was similar to the C 1s spectra of the methylene blue - illite mixture, indicating that methylene blue was bound to the surface of the clay particles.

The functional groups present in the two model organics were very different. In methylene blue aromatic components were well associated with the surface of illite. However, naphthenic acid was found to separate into different components which appeared to segregate onto different surfaces. In particular, the aromatic component in naphthenic acid was the major component present at the surface of illite particles.

The C 1s NEXAFS spectra of four bitumen froth process samples provided nearly similar spectra. The area under the π^* peak, representing the amount of unsaturated carbon present in each froth, was studied. We were able to determine that the two froths from Petrocan contained significantly more unsaturated carbon than the primary and secondary froths from Suncor. Our findings were correlated with previous studies by our collaborators at NRCan showing that the froths contained different morphologies which were indicative of changed bitumen chemistry, observed by fluorescence changes. Using our quantitative NEXAFS data, we were able to show that the changes in the bitumen chemistry may be in part related to differences in unsaturated carbon present in the froths.

However, direct correlation for the four froths was not possible; inhomogeneity is implicated.

6.2 Future Work

The development of effective sample preparation was one of the major achievements accomplished in this thesis work. The ability to obtain samples with clean surfaces, free from contaminants and artifacts is essential for proper characterization. Our newly defined preparation procedures can be applied and used to study hydrocarbon-clay interactions using additional model systems, with different models and organic species, to further test our initial observations regarding strong interactions between certain naphthenic acid components and clay surfaces. A study testing preferential interactions of naphthenic acid with clay mixtures using fine clays obtained from clay banks and from natural sources (oil sands) will also be performed. The use of the anticontaminator will be essential in many future studies on this project, as well as other systems with very low carbon concentrations.

To further this work, it would be extremely useful to increase surface sensitivity, which could be achieved by using total electron yield detection in the STXM. Using the STXM to detect TEY signal from samples is currently an ongoing challenge being investigated by a Dr. Urquhart and Dr. Tyliszczak. This would require the use of STXM 11.0.2 at the ALS or the soft microscopy STXM at the CLS, as they operate on elliptically polarized undulator (EPU) beamlines, which creates more flux, thereby providing a greater signal for TEY detection. Studying model hydrocarbon-clay systems using TEY will enhance surface sensitivity at the hydrocarbon-clay surface. This can then

be further applied in studies regarding samples extracted directly from the oil sands, with inherent carbon, without bleaching.

References

(1) Liu, J.; Xu, Z.; Masliyah, J. *Journal of Materials, Interfaces, and Electrochemical Phenomena* **2004**, *50*, 1917.

(2) Liu, J.; Xu, Z.; Masliyah, J. *The Canadian Journal of Chemical Engineering* **2004**, *82*, 655.

(3) Munoz, V. A.; Kasperski, K. L.; Omotoso, O. E.; Mikula, R. J. *Petroleum Science and Technology* **2003**, *21*, 1509.

(4) Urquhart, S. G.; Hitchcock, A. P.; Smith, A. P.; Ade, H. W.; Lidy, W.; Rightor, E. G.; Mitchell, G. E. *Journal of Electron Spectroscopy and Related Phenomena* **1999**, *100*, 119.

(5) Urquhart, S. G.; Smith, A. P.; Ade, H. W.; Hitchcock, A. P.; Rightor, E. G.; Lidy, W. *Journal of Physical Chemistry B* **1999**, *103*, 4603.

(6) Hitchcock, A. P. *Journal of Synchrotron Radiation* **2001**, *8*, 66.

(7) Hitchcock, A. P.; Morin, C.; Zhang, X.; Araki, T.; Dynes, J.; Stover, H.; Brash, J.; Lawrence, J. R.; Leppard, G. G. *Journal of Electron Spectroscopy and Related Phenomena* **2005**, *144-147*, 259.

(8) Ade, H.; Urquhart, S. G. NEXAFS Spectroscopy and Microscopy of Natural and Synthetic Polymers. In *Chemical Applications of Synchrotron Radiation: Part I: Dynamics and VUV Spectroscopy*; Sham, T.-K., Ed.; World Scientific Publishing Co. Ltd: Singapore, **2002**; Vol. 12A; pp 285.

(9) Kikuma, J.; Tonner, B. P. *Journal of Electron Spectroscopy and Related Phenomena* **1996**, *82*, 53.

(10) Urquhart, S. G.; Ade, H. *Journal of Physical Chemistry B* **2002**, *106*, 8531.

(11) Urquhart, S. G.; Cooney, R. *Journal of Physical Chemistry B* **2004**, *108*, 18185.

(12) Kaznacheyev, K.; Osanna, A.; Jacobsen, C.; Plasshkevych, O.; Vahtras, O.; Agren, H.; Carravetta, V.; Hitchcock, A. P. *Journal of Physical Chemistry A* **2002**, *106*, 3153.

(13) Jacobsen, C.; Beetz, T.; Feeser, M.; Osanna, A.; Stein, A.; Wirick, S. *Surface Review and Letters* **2002**, *9*, 185.

(14) Ildefonse, P.; Cabaret, D.; Sainctavit, P.; Calas, G.; Flank, A.-M.; Lagarde, P. *Physics Chemical Materials* **1998**, *25*, 112.

(15) Neuhausler, U.; Abend, S.; Ziesmer, S.; Schulze, D.; Stott, D.; Jones, K.; Feng, H.; Jacobsen, C.; Lagaly, G. "Soft X-ray Spectromicroscopy on Hydrated Colloidal and Environmental Science Samples"; X-ray Microscopy: Proccedings of the Sixth International Conference, **2000**.

(16) Thieme, J.; Schmidt, C.; Niemeyer, J. "Studies of Colloidal Systems in Soils with X-ray Microscopy"; X-Ray Microscopy: Proceedings of the Sixth International Conference, **2000**.

(17) Su, L.; Xu, Z.; Masliyah, J. *Minerals Engineering* **2006**, *19*, 641.

(18) Long, J.; Xu, Z.; Masliyah, J. *Colloids and Surfaces A: Physicochemical Engineering Aspects* **2006**, *281*, 202.

(19) Lam, W. W.; Tyerman, W. J. R.; Payette, C.; Mikula, R. J.; Sanford, E. C. *Fuel Science and Technology International* **1995**, *13*, 483.

(20) Czarnecka, E.; Gillott, J. E. *Clays and Clay Minerals* **1980**, *28*, 197.

(21) Omotoso, O. E.; Mikula, R. J. *Applied Clay Science* **2004**, *25*, 37.

(22) Bukka, K.; Miller, J. D.; Oblad, A. G. *Energy & Fuels* **1991**, *5*, 333.

(23) Gafonova, O. V.; Yarranton, H. W. *Journal of Colloid and Interface Science* **2001**, *241*, 469.

(24) Zhao, S.; Kotlyar, L. S.; Woods, J. R.; Sparks, B. D.; Gao, J.; Chung, K. H. *Petroleum Science and Technology* **2003**, *21*, 183.

(25) Fong, N.; Ng, S.; Chung, K. H.; Tu, Y.; Li, Z.; Sparks, B. D.; Kotlyar, L. S. *Fuel* **2004**, *83*, 1865.

(26) Chong, J.; Ng, S.; Chung, K. H.; Sparks, B. D.; Kotlyar, L. S. *Fuel* **2003**, *82*, 425.

(27) Bantignies, J.-L.; Cartier dit Moulin, C.; Dexpert, H. *Clays and Clay Minerals* **1997**, *45*, 184.

(28) Rehr, J. J.; Albers, R. C. *Reviews of Modern Physics* **2000**, *72*, 621.

(29) Rehr, J. J. *Radiation Physics and Chemistry* **2006**, *75*, 1547.

(30) George, G. N.; Hedman, B.; Hodgson, K. O. *Nature Structural Biology* **1998**, *5*, 645.

(31) Stöhr, J. *NEXAFS Spectroscopy*; Springer-Verlag: Berlin, **1992**; Vol. 25.

(32) Fu, J. X.; Urquhart, S. G. *Journal of Physical Chemistry A* **2005**, *109*, 11724.

(33) Margaritondo, G. *Introduction to Synchrotron Radiation*; Oxford University Press: Oxford, **1988**.

(34) Snigireva, I.; Snigirev, A. *Journal of Environmental Monitoring* **2006**, *8*, 33.

(35) Yoon, T. H.; Johnson, S. B.; Benzerara, K.; Doyle, C. S.; Tyliszczak, T.; Shuh, D. K.; Brown, G. E. *Langmuir* **2004**, *20*, 10361.

(36) Hitchcock, A. P.; Koprinarov, I.; Tyliszczak, T.; Rightor, E. G.; Mitchell, G. E.; Dineen, M. T.; Hayes, F.; Lidy, W.; Priester, R. D.; Urquhart, S. G.; Smith, A. P.; Ade, H. *Ultramicroscopy* **2001**, *88*, 33.

(37) Holman, H. Y. N.; Perry, D. L.; Martin, M. C.; Lamble, G. M.; McKinney, W. R.; Hunter-Cevera, J. C. *Geomicrobiology Journal* **1999**, *16*, 307.

(38) Holman, H. Y. N.; Martin, M. C.; McKinney, W. R. *Journal of Biological Physics* **2003**, *29*, 275.

(39) Urquhart, S.; Lanke, U.; Fu, J. *International Journal of Nanotechnology* **2007**, (accepted).

(40) Doub, W. H.; Adams, W. P.; Spencer, J. A.; Buhse, L. F.; Nelson, M. P.; Treado, P. J. *Pharmaceutical Research* **2007**, *24*, 934.

(41) Braun, A.; Huggins, F. E.; Shah, N.; Chen, Y.; Wirick, S.; Mun, B. S.; Jacobsen, C.; Huffman, G. P. *Carbon* **2005**, *43*, 117.

(42) Ade, H.; Zhang, X.; Cameron, S.; Costello, C.; Kirz, J.; Williams, S. *Science* **1992**, *258*.

(43) Rightor, E. G.; Hitchcock, A. P.; Ade, H.; Leapman, R. D.; Urquhart, S. G.; Smith, A. P.; Mitchell, G. E.; Fischer, D.; Shin, H. J.; Warwick, T. *Journal of Physical Chemistry B* **1997**, *101*, 1950.

(44) Neuhausler, U.; Jacobsen, C.; Schulze, D.; Stott, D.; Abend, S. *Journal of Synchrotron Radiation* **2000**, *7*, 110.

(45) Rothe, J.; Denecke, M. A.; Dardenne, K. *Journal of Colloid and Interface Science* **2000**, *231*, 91.

(46) Myneni, S. C. B.; Brown, J. T.; Martinez, G. A.; Meyer-Ilse, W. *Science* **1999**, *286*, 1335.

(47) Neuhausler, U.; Abend, S.; Jacobsen, C.; Lagaly, G. *Colloid Polymer Science* **1999**, *277*, 719.

(48) Velde, B. *Clay Minerals: A Physico-Chemical Explanation of their Occurrence*; Elsevier: Amsterdam, **1985**; Vol. 40.

(49) Downs, R. T.; Hall-Wallace, M. *American Mineralogist* **2003**, *88*, 247.

(50) Hahner, G.; Marti, A.; Spencer, N. D. *Journal of Chemical Physics* **1996**, *104*, 7749.

(51) Zwahlen, M.; Brovelli, D.; Caseri, W.; Hahner, G. *Journal of Colloid and Interface Science* **2002**, *256*, 262.

(52) Fischer, D.; Caseri, W.; Hahner, G. *Journal of Colloid and Interface Science* **1998**, *198*, 337.

(53) Headley, J. V.; McMartin, D. W. *Journal of Environmental Science and Health Part a-Toxic/Hazardous Substances & Environmental Engineering* **2004**, *39*, 1989.

(54) Yan, Z.; Elliott, A. W.; Masliyah, J. *Journal of Colloid and Interface Science* **1999**, *220*, 329.

(55) Watts, B.; Thomsen, L.; Dastoor, P. C. *Journal of Electron Spectroscopy and Related Phenomena* **2006** *151*, 105.

(56) Attwood, D. *Soft X-Rays and Extreme Ultraviolet Radiation: Principles and Applications*; Cambridge University Press: Cambridge, UK, **1999**.

(57) Jacobsen, C.; Chapman, H.; Kirz, J.; Maser, J.; Osanna, A.; Spector, S.; Wang, S.; Wirick, S.; Zhang, X. *Molecular Biology of the Cell* **1995**, *6*, 660.

(58) Neuhausler, U.; Schmidt, C.; Hoch, M.; Susini, J. *Journal de Physique IV, Colloque* **2003**, *104*, 443.

(59) Hitchcock, A. P.; Morin, C.; Tyliszczak, T.; Koprinarov, I. N.; Ikeura-Sekiguchi, H.; Lawrence, J. R.; Leppard, G. G. *Surface Review and Letters* **2002**, *9*, 193.

(60) Kilcoyne, A. L. D.; Tylisczack, T.; Steele, W. F.; Fakra, S.; Hitchcock, P.; Franck, K.; Anderson, E.; Harteneck, B.; Rightor, E. G.; Mitchell, G. E.; Hitchcock, A. P.; Yang, L.; Warwick, T.; Ade, H. *Journal of Synchrotron Radiation* **2003**, *10*, 125.

(61) Warwick, T.; Ade, H.; Kilcoyne, D.; Kritscher, M.; Tylisczack, T.; Fakra, S.; Hitchcock, A.; Hitchcock, P.; Padmore, H. *Journal of Synchrotron Radiation* **2002**, *9*, 254.

(62) Jacobsen, C.; Wirick, S.; Flynn, G.; Zimba, C. *Journal of Microscopy* **2000**, *197*, 173.

(63) Tyliszczak, T., Lawrence Berkeley National Laboratories, Advanced Light Source, Berkeley, CA.

(64) Hao, C.; Headley, J. V.; Peru, K. M.; Frank, R.; Yang, P.; Solomon, K. R. *Journal of Chromatography A* **2005**, *1067*, 277.

(65) Shelden, R. A.; Caseri, W. R.; Suter, U. W. *Journal of Colloid and Interface Science* **1993**, *157*, 318.

* Permission was granted for all previously published figures that were used in this thesis.